Application of Actuator Surface Concept in LES Simulations of the Near Wake of Wind Turbines

by

Jörn NATHAN

THESIS PRESENTED TO ÉCOLE DE TECHNOLOGIE SUPÉRIEURE
IN PARTIAL FULFILLMENT FOR THE DEGREE OF
DOCTOR OF PHILOSOPHY
Ph.D.

MONTREAL, MARCH 19, 2018

ÉCOLE DE TECHNOLOGIE SUPÉRIEURE
UNIVERSITÉ DU QUÉBEC

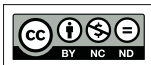

BOARD OF EXAMINERS

THIS THESIS HAS BEEN EVALUATED

BY THE FOLLOWING BOARD OF EXAMINERS

Prof. Christian Masson, Ph.D., Thesis Supervisor
Département de génie mécanique, École de technologie supérieure

Prof. Louis Dufresne, Ph.D., Co-supervisor
Département de génie mécanique, École de technologie supérieure

Prof. Simon Joncas, Ph.D., President of the Board of Examiners
Département de génie de la production automatisée, École de technologie supérieure

Prof. François Morency, Ph.D., Member of the jury
Département de génie mécanique, École de technologie supérieure

Prof. Éric Laurendeau, Ph.D., External Independent Examiner
Département de génie mécanique, Polytechnique Montréal

THIS THESIS WAS PRESENTED AND DEFENDED

IN THE PRESENCE OF A BOARD OF EXAMINERS AND THE PUBLIC

ON MARCH 15, 2018

AT ÉCOLE DE TECHNOLOGIE SUPÉRIEURE

FOREWORD

The rise of wind energy during the last decades caused a shortage of available space for conceiving new wind farms. Hence the farm layout tends to adapt denser turbine arrangements which cause stronger turbine to turbine interactions in the form of wakes. They have an important impact on the downstream turbines performance and fatigue as they exhibit a higher turbulence level and velocity deficit. This work first validates the rotor model of the actuator line with another existing implementation and then verifies it against experimental results. After having established a valid base case, the rotor is then immersed in ambient turbulence notably homogeneous isotropic turbulence and shear layer turbulence in order determine their influence on the near wake. Several interesting findings are deduced from this numerical experiment and contribute to the understanding of the underlying method and its applicability.

ACKNOWLEDGEMENTS

I gratefully acknowledge my supervisor Professor Christan Masson for having me given the opportunity to participate engage in wind energy research through his group. Thanks for your presence, support and guidance which always shed light on aspects I had not fully considered allowing me to improve this work in a constant manner. Also grateful acknowledgements to my co-supervisor Louis Dufresne for his guidance on CFD and particular on turbulence. The discussions with you allowed me to obtain a more insight to this vast topic and its relation to my work.

This research was funded by the Canadian Research Chair on the Nordic Environment Aerodynamics of Wind Turbines and the Natural Sciences and Engineering Research Council (NSERC) of Canada. Their support is greatly appreciated. Also a lot of thanks goes to Calcul Québec and Compute Canada for their computational resources, namely the super-computer Colosse and Guillimin and their outstanding technical support group.

I also want to thank all the people I had the chance to work with at the research group of Professor Christian Masson, in particular Mary, Hugo and Pascal with whom I shared the joy and burden to use the open-source framework OpenFOAM for the numerical simulations. Furthermore I would like to mention some people I enjoyed sharing time at the university in the last years, namely Jon, Simon-Philippe, Nico, Nico, Yann-Aël, Alex and Éric.

A special word of gratitude goes to the people I had the opportunity to collaborate with. First there was my stay at the NWTC site near Boulder, CO, USA under the guidance of Matthew Churchfield, the main architect of the SOWFA framework, a very inspirational man on a professional as well as on a personal level. Also thanks a lot to Alexander Meyer Forsting from the DTU, Denmark, with whom I had the chance to collaborate on the comparison of SOWFA and EllipSys3D. I enjoyed working with you and also sharing some private moments.

Finally my biggest thanks goes to my dear partner Julie, whose continuous support made this PhD possible. Thank you for sharing our lives and the ones of our adorable children Gloria & Paul.

APPLICATION DE LA SURFACE ACTUATRICE DANS DES SIMULATIONS AUX GRANDES ÉCHELLES POUR LE SILLAGE PROCHE

Jörn NATHAN

RÉSUMÉ

Au cours des dernières décennies, l'énergie éolienne est devenue une partie cruciale des énergies renouvelables, qui cherchent à satisfaire la demande d'énergie d'une façon durable. La conception actuelle des pales des éoliennes est proche de son optimum aérodynamique, donc le défi principal, de nos jours, est la viabibilité dans la concecption des parcs éoliens. En conséquence, les parcs éoliens sont développés avec une densité des turbines plus élévée et sur des terrains plus complexes au niveau de la topographie. C'est ainsi que l'interaction entre les turbines, notamment par les sillages, joue un rôle très important dans la conception des sites. Les sillages sont caracterisés par le niveau élévé de la turbulence et le déficit de la vitesse. Alors que l'industrie préfère des solutions approximatives à cause des coûts de calcul, le caractère non-linéaire du phénomène est mieux décrit par les équations de Navier-Stokes. Dû au fait qu'il n'y a pas de solution analytique pour ces équations, la dynamique des fluides computationnelle est souvent utilisée. Des niveaux différents de fidélité peuvent être atteints selon la représentation de la turbulence.

L'objectif de ce travail est d'examiner le sillage proche d'une éolienne pour des turbulences ambiantes différentes. Le rotor est représenté par la méthode de la ligne actuatrice implementée dans le cadre applicatif très populaire SOWFA du NREL, USA. Un cas sans turbulence ambiante est validé avec une autre structure logicielle pour l'énergie éolienne populaire, EllipSys3D. Par la suite, le cas est vérifié avec des résultats expérimentaux provenant des expériences en soufflerie MEXICO et NEW MEXICO. En adaptant la largeur de distribution de la force dans le domaine numérique, la ligne actuatrice se dirige vers la surface actuatrice. La largeur de distribution pour le cas présenté ici est déterminée d'une façon empirique.

Une fois le cas de base établi, le rotor est immergé dans une turbulence homogène isotrope pour laquelle une condition à la frontière a été conçue dans le cadre applicatif OpenFOAM. La turbulence synthétique obtenue par l'algorithme de Mann est imposée à la simulation aux grandes échelles avec le modèle dynamique Lagrangien pour les échelles de sous-maille. Finalement, le rotor est exposé à la turbulence cisaillée générée par une librairie externe permettant l'utilisation de la turbulence synthétique obtenue par l'algorithme de Mann dans un cas cisaillé. En analysant les propriétés tourbillonaires et le spectre d'énergie dans les deux cas de turbulence, on peut déduire l'influence de la turbulence ambiante sur le sillage proche. Un autre aspect intéressant est de déterminer, grâce aux spectres, jusqu'à quelle distance en aval les pales distinctes du rotor peuvent être ressenties par l'écoulement.

Mots-clés: énergie éolienne, sillage des éoliennes, modélisation de turbulence, ligne actuatrice, simulation aux grandes échelles, turbulence homogène isotrope, turbulence cisaillée

APPLICATION OF ACTUATOR SURFACE CONCEPT IN LES SIMULATIONS OF THE NEAR WAKE OF WIND TURBINES

Jörn NATHAN

ABSTRACT

During the last decades wind energy became a crucial part of the renewable energy mix seeking to satisfy the growing energy demands in a sustainable manner. While current state of the art wind turbine blades are close to their aerodynamical optimum, the challenge lies today in the viability of concepted wind farms. Hence wind farm designs aim for denser turbine arrangements and topographically more complex terrains. Therefore the interaction between turbines namely through the wind turbine wakes become an important aspect of the layout of a wind farm. Theses wakes are characterized by an elevated turbulence level and a noticable velocity deficit. While the wind energy industry prefers more approximative solutions for the sake of computational costs, the non-linear character of the phenomenon is best captured by the Navier-Stokes equations. As there exists no analytical solution, computational fluid dynamics is used to tackle this equation. Depending on the turbulence modelling different levels of accuracy can be achieved.

The objective of this work is to examine the near wake of a wind turbine for different kinds of ambient turbulences. The rotor is represented by the actuator line method implemented in the widely popular wind energy framework SOWFA from NREL, USA. In order to evaluate the here used method a non-turbulent test case is validated against another popular wind energy framework EllipSys3D and then verified with the results from the open jet wind tunnel experiments MEXICO and NEW MEXICO. By adapting the distribution width of the force within the computational domain this approach is then extended towards an actuator surface. An optimal distribution width depending on the grid resolution is found empirically for the here presented case.

After the base case is established and successfully tested the rotor is immersed in homogeneous isotropic turbulence for which a custom boundary condition for the OpenFOAM framework is conceived. Then the synthetic turbulence field obtained by the Mann algorithm is imposed on the large-eddy simulation with dynamic Lagrangian model for the sub-grid scales. Finally the rotor is exposed to a shear layer turbulence using an external library allowing to impose a synthetic turbulent field obtained from the Mann algorithm on a sheared flow. By analyzing the vortex properties and the energy spectra in both cases the influence of the ambient turbulence on the near wake are deduced. Another interesting aspect is the way how the energy spectra gives insight in how far downstream the effects of the distinct blades are noticable.

Keywords: wind energy, wind turbine wakes, turbulence modelling, actuator line method, large-eddy simulations, homogeneous isotropic turbulence, shear layer turbulence

TABLE OF CONTENTS

LIST OF TABLES

Page

LIST OF FIGURES

Page

LIST OF ABREVIATIONS

ABL	atmospheric boundary layer
ADM	actuator disk method
AL	actuator line
ALM	actuator line method
AOA	angle of attack
ASM	actuator surface method
BEM	blade element momentum
CBC	convective boundedness criterion
CD	central differencing
CDS	central differencing scheme
CFD	computational fluid dynamics
CR	contraction ratio
DES	detached eddy simulation
DNS	direct numerical simulation
DNW	German-Dutch Wind tunnels
FVM	finite volume method
HAWT	horizontal axis wind turbine
HIT	homogeneous isotropic turbulence
HPC	high performance computing

IEA	international energy agency
LES	large-eddy simulation
LUD	linear upwind differencing
LUST	linear-upwind stabilized transport
MEXICO	model experiments in controlled conditions
MINMOD	minimal model
NASA	national aeronautics and space administration
NREL	national renewable energy laboratory
NS	Navier-Stokes
NVA	normalized variable approach
NVD	normalized variable diagram
NWTC	national wind technology center
PISO	pressure-implicit split-operator
PIV	particle image velocimetry
PSD	power spectral density
QUICK	quadratic upstream interpolation for convective kinematics
RANS	Reynolds-averaged Navier–Stokes
RPM	revolutions per minute
SFS	sub-filter scale
SGS	sub-grid scale

SIMPLE	semi-implicit method for pressure linked equations
SOWFA	simulator for wind farm applications
SST	shear stress transport
TORQUE	The Science of Making Torque from Wind
TI	turbulence intensity
TVD	total variation diminishing
UD	upwind differencing
USA	United States of America
VAWT	vertical axis wind turbine

LISTE OF SYMBOLS AND UNITS OF MEASUREMENTS

General notation

$\langle a \rangle$	time-averaged quantity
$\langle a \rangle_{Psi}$	phase-averaged quantity
$\langle a \rangle_{\Psi=0^\circ}$	phase-averaged quantity for $\Psi = 0$
$\overline{a}$	filtered quantity
$\widehat{\overline{a}}$	filtered quantity by two different filter
a'	sub-grid quantity
a_f	quantity at cell face
a_O	quantity of neighbour cell
a_P	quantity of center cell
a_Q	quantity of other neighbour cell

Lower-case Roman

a	discretization coefficient $[-]$
c	blade chord [m]
c_D	drag coefficient $[-]$
c_L	lift coefficient $[-]$
$c_{porosity}$	porosity coefficient $[-]$
d	distance between two actuator points [m]
$\mathbf{d}$	distance between face and cell center [m]

$\mathbf{d}_x$	distance vector between cell center and actuator point [m]
$\mathbf{e}_D$	unit vector in direction of drag [−]
$\mathbf{e}_L$	unit vector in direction of lift [−]
$\mathbf{e}_n$	normal unit vector [−]
$\mathbf{e}_t$	tangential unit vector [−]
f_i	force components [m/s^2]
f_{tip}	tip correction [−]
f_x	distance ratio for discretization schemes [−]
k	turbulent kinetic energy [m/s^2]
k_p	turbulent kinetic energy [m/s^2]
$\mathbf{k}$	non-orthogonal part of face area vector $\mathbf{S}$ [m^2]
l	distance between vortices [m]
l_s	length of actuator segment [m]
p	pressure [m^2/s^2]
r	radial coordinate [m]
r_{ap}	radius of actuator point [m]
r_{core}	vortex radius [m]
t	tangential coordinate [m]
t_i	time [s]
w	lateral and vertical extent of refined zone [m]

x	axial coordinate [m]
$\mathbf{x}$	coordinate of point [m]
x_0	distance from beginning of domain and rotor position [m]
x_{00}	distance from beginning of refined zone and rotor position [m]
x_1	distance from rotor position to end of domain [m]
x_{11}	distance from rotor position to end of refined zone [m]
$\mathbf{x}_P$	coordinate of cell center [m]
y	lateral coordinate [m]
z	vertical coordinate [m]

Upper-case Roman

A	discretization matrix [−]
A_h	non-covered area by distribution kernel [m^2]
A_t	area covered by distribution kernel [m^2]
C_{ij}	cross stress tensor [$1/(ms^2)$]
$\mathscr{C}_{ij}$	cross stress tensor (definition by Germano (1986)) [$1/(ms^2)$]
C_s	Smagorinsky coefficient [−]
C_T	thrust coefficient [−]
D	rotor diameter [m]
E	three-dimensional energy spectra as a function of the wavenumber [m^3/s^2]
$\mathbf{F}$	body force [m/s^2]

$F_1(k_1)$	one-dimensional energy spectra for longitudinal wavenumber $[\mathrm{m}^3/\mathrm{s}^2]$
F_D	drag force [N]
F_{flux}	convective flux $[\mathrm{m}^3/\mathrm{s}]$
F_L	lift force [N]
$\mathfrak{F}_{LM}$	integral trajectory using $L_{ij}M_{ij}$ $[1/(\mathrm{m}^2\mathrm{s}^3)]$
$\mathfrak{F}_{MM}$	integral trajectory using $M_{ij}M_{ij}$ $[1/(\mathrm{m}^2\mathrm{s}^3)]$
F_n	normal force $[\mathrm{N}/\mathrm{m}]$
F_t	tangential force $[\mathrm{N}/\mathrm{m}]$
F_P	punctual blade force [N]
$\mathscr{G}$	Gaussian distribution kernel $[-]$
H	reduced set of discretization matrix A $[-]$
L	integral length scale [m]
L_{ij}	Leonard stress tensor $[1/(\mathrm{ms}^2)]$
$\mathscr{L}_{ij}$	Leonard stress tensor (definition by Germano (1986)) $[1/(\mathrm{ms}^2)]$
$L_{x,y,z}$	axial, lateral, vertical extent of computational domain [m]
N	number of cells per rotor diameter $[-]$
N_{blades}	number of blades $[-]$
N_b	number of blade points $[-]$
P	center point of center cell [m]
P_0	center of rotation [m]

P_{new}	actuator point after rotation [m]
P_{old}	actuator point before rotation [m]
R	rotor radius [m]
$\mathbf{R}$	rotation matrix [−]
R_{hub}	hub radius [m]
R_{ij}	Reynolds stress tensor $[1/(\mathrm{ms}^2)]$
$\mathscr{R}_{ij}$	Reynolds stress tensor (definition by Germano (1986)) $[1/(\mathrm{ms}^2)]$
R_{res}	residual [m/s]
R_S	integration radius for obtaining total circulation Γ [m/s]
Re	Reynolds number [−]
$\mathbf{S}$	face area vector $[\mathrm{m}^2]$
S	source term $[\mathrm{m/s}^2]$
S_{ij}	rate-of-strain tensor [1/s]
T	rotor torque [Nm]
T_{ij}	stress tensor on coarser grid $[1/(\mathrm{ms}^2)]$
T_{lagDyn}	time scale used in sub-grid model proposed in Meneveau *et al.* (1996) $[1/(\mathrm{ms}^2)]$
TI_{syn}	turbulence intensity of synthetic turbulence field
$\mathbf{U}$	velocity [m/s]
U_{mag}	velocity magnitude [m/s]
$U_{x,r,t}$	axial, radial and tangential velocity component [m/s]

U_∞	velocity magnitude [m/s]
$\mathbf{U}_s$	sampled velocity [m/s]
V	volume [m^3]
W	weighting function in sub-grid model proposed in Meneveau *et al.* (1996) [−]

Lower-case Greek

α	angle of attack [°]
α_p	exponent for wind power law [−]
$\alpha\varepsilon^{2/3}$	scaling coefficient in energy spectrum [m^2/s^3]
β	parameter used in model by Mann (1998) [−]
γ	blending factor in blended schemes [−]
$\varepsilon*$	turbulent dissipation rate [m^2/s^3]
θ	parameter for sub-grid model proposed in Meneveau *et al.* (1996) [−]
κ	wavenumber [1/m]
κ_p	wavenumber corresponding to blade passage [1/m]
ν	kinematic viscosity [m^2/s]
σ	variance [m/s]
τ	stress tensor [$1/(ms^2)$]
ϕ	generic variable [−]
φ_T	blade twist angle [°]
φ_P	blade pitch angle [°]

ω	vorticity $[1/\mathrm{s}]$
$\omega*$	specific rate of dissipation $[1/\mathrm{s}]$
ω_{rot}	rotation frequency of rotor $[1/\mathrm{s}]$

Upper-case Greek

Δ	filter width [m]
Δt	time step [s]
Δx	cell size [m]
Γ	circulation $[\mathrm{m}^2/\mathrm{s}]$
Γ_ϕ	dissipation coefficient for ϕ $[\mathrm{m}^2/\mathrm{s}]$
Ψ	rotor position $[^\circ]$

INTRODUCTION

The installed wind energy capacity has steadily risen over the last twenty years as shown in Figure (0.1) (BP, 2017). While having locally some slowdowns, such as e.g. the US capacity following the 2008 economic crisis and again in 2013, the overall trend has an increasing grow-rate. In North America the wind energy farms clearly dominate whereas the Canadian capacity has risen to almost $12GW$ with one third of it in Québec in 2016 which is almost a tenfold increase compared to 2006. China has caught up and almost overtaken the important wind energy regions North America and Europe, which makes it a very interesting market in the short-term. The three main player China, North America and Europe are making up almost the total of the entire installed world capacity.

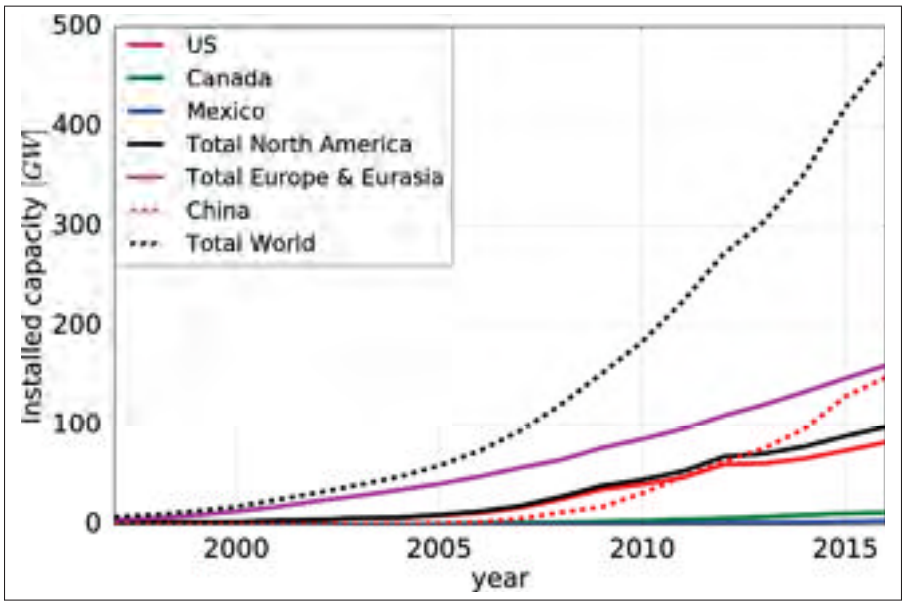

Figure 0.1 Installed wind energy capacity for different countries and regions in the world taken from BP (2017).

While the aerodynamic efficiency of wind turbine blade is close to their optimum, one of the remaining challenges resides in the design of wind farms and their operation. As a flat, homogeneous and obstacle-free terrain would be optimal in terms of installation and maintenance of

wind farms, the upcoming lack of its availability is forcing wind energy companies to prospect also sites with complex terrain and higher roughness, e.g. with forests. In order to raise the viability of a wind farm project often a very dense turbine arrangement is prefered. A phenomenon which can decrease the energy output up to 20 % (Manwell *et al.*, 2010) is the occurring wake behind the rotor. The velocity deficit due to the wake reduces the energy output of a downwind wind turbine, which can cause significant losses in wind turbine arrays under certain wind directions.

In order to describe this phenomenon the effects of the rotor on the flow have to be modelled correctly. The thrust and torque caused by the wind turbine creates a wake in the downstream region, which is influenced by turbulent structures of different magnitudes such as the vortices created by the blade tips and the shear layer turbulence of the atmospheric boundary layer. Furthermore the structure of the terrain and its roughness have to be taken into account in order to model the correct inflow conditions for wind turbine but also their influence on the wake. In this work the focus will be put on the aerodynamics of near wake and the capability of actuator methods and turbulence models to describe it.

The near wake representation in a computational fluid dynamics simulation depends heavily on the applied rotor model (Sanderse *et al.*, 2011). Approaches range from actuator forces inserted as momentum sink in the Navier-Stokes equations to fully resolved rotor representations where the attached boundary layers on the blades are simulated. In order to create vortical structures in a CFD simulation at relatively low cost this work will apply an actuator force approach in order to model the transient behaviour of the rotor. Each blade will be represented by a force line allowing to reproduce the helicoidal vortical structure in the near wake.

Once this model is validated and verified with a non-turbulent flow, ambient turbulence will be added. First the rotor is immersed in an homogeneous isotropic turbulence which corresponds to wind tunnel experiments at different turbulence intensities. Then shear layer turbulence is

introduced exposing the rotor model to a more realistic wind flow situation which bears more resemblance to applied wind energy.

Objectives and methodology

The main objective is the description of the near wake properties of a horizontal axis wind turbine immersed in different ambient turbulence flows by the means of the actuator line method extended towards the actuator surface method. It can be subdivided into three specific objectives:

- Implementation and validation of actuator line model and its extension, the actuator surface model.
- Embedding and validation of actuator surface into large eddy simulation (LES) with homogeneous isotropic turbulence.
- Embedding and validation of actuator surface into LES with shear layer turbulence.

It is expected that by the aid of the results of this study the understanding of the wake phenomena and usability of the underlying rotor model will be improved. Finally this model could also be introduced in a simulation for obtaining a wind energy assessment of a site taking into accounts the effects of complex terrain and ABL flow using a detailed description of the rotor effects.

Original contribution

The original scientific contributions of this research project are in summary the following:

- successful comparison of ALM implementation of the two most popular CFD frameworks for wind energy
- empiricial deduction of necessary distribution width depending on grid resolution

- coupling of OpenFOAM framework with Gillings (2009) implementation of Mann (1998) algorithm
- immersion of ALM within synthetic shear layer turbulence of Muller (2015)
- determination of near-wake limits based on energy spectra

Thesis overview

The work will start out with the literature overview in Chapter 1 where the state of the current research on the topic is presented. It will include currently used rotor models, turbulence models and flow models before in the concluding remarks the choice and their justification are stated. This is followed by the numerical methodology in Chapter 2 where firstly an overview of the OpenFOAM framework is given. Then the implementation of the rotor model is discussed followed by a description of the flow model. Here the large-eddy simulation and its sub-grid modelling are discussed. Finally the methods of synthetic turbulence are presented for the homogeneous isotropic and the shear layer turbulence. In Chapter 3 the MEXICO and NEW MEXICO experiments are shown serving as verification of the base case.

In Chapter 4 the results for the validation and verification of the base case are presented. As the final focus of this work is the near wake, the base case then undergoes a sensitivity study in order to reduce the mesh size to obtain the final case. In Chapter 5 the established rotor model is then immersed in homogeneous isotropic turbulence and the wake characteristics are analyzed. Finally in Chapter 6 the rotor is exposed to the shear layer flow and its results are discussed.

This is followed by a conclusion and an appendix containing the complete table of the used airfoil coefficients, the exact geometrical definition of the blades used in the MEXICO and NEW MEXICO experiments.

CHAPTER 1

LITERATURE REVIEW

In this chapter a literature review will be presented in order to develop a methodology to achieve the above stated objectives. It is also used to put the objectives in a more global context in order to evaluate the impact of the contributions. First a look will be taken at the aerodynamic aspects of a wind turbine and its associated wake in Section 1.1. Then several modelling aspects will be discussed, such as the rotor, flow and turbulence modelling in sections 1.2, 1.3 and 1.4 respectively. Followed by an overview of wind turbine experiments in Section 1.5, finally a conclusion is given including a justification for the chosen methods in this work.

1.1 Aerodynamics

Wind turbines can be divided into two main categories based on their axial orientation, the vertical axis wind turbine (VAWT) and the horizontal axis wind turbine (HAWT). Although there have been efforts to establish VAWTs more widely in the wind energy industry (Shamsoddin & Porté-Agel, 2016), it still remains a punctual solution for remote locations as they prove to be low-maintenance. As the HAWTs represent the majority of wind energy applications, this work solely focuses on this turbine type and more precisely on three-bladed rotors working as lifting devices. The blade number represents an optimum in terms of energetic gain versus thrust (Hau, 2008) and it is therefore the most commonly used configuration used in the industry.

The interaction between the wind flow and the rotating blades of the wind turbine results in a pressure difference between the two sides of the blade. Hence a lift is created resulting in a torque from which different forms of energy can be derived (Vermeer *et al.*, 2003). An important difference to fixed-wing aerodynamics is the rotating motion of the blade resulting in Coriolis and centrifugal forces (Hansen *et al.*, 2006). While the centrifugal pumping creates a radial flow in direction of the tip, the Coriolis forces deflect the flow towards the trailing edge. This creates a favorable pressure gradient and therefore delays the stall (Leishman, 2002).

This has to be kept in mind in regards to rotor modelling as many of those methods rely on experimental data obtained from a fixed-wing experiment.

The wake behind a wind turbine is characterized by a velocity deficit which recovers in the downstream direction until there are no more discernible effects. At the turbine location the rotating blades extract energy and cause a sudden pressure drop across the rotor plane and a steady and more continuous decrease of the velocity magnitude.

Figure 1.1 Different wake regions (separated by dashed lines) downstream of the rotor (solid line).

The wake region can be split in several sub-regions as illustrated in Figure (1.1). The near wake is the region in vicinity of the rotor up to one (Vermeer *et al.*, 2003) or two (Sanderse *et al.*, 2011) rotor diameter downstream. In this region the vortex sheets created due to radial variation of the circulation shed from the trailing edge roll up and merge with the tip vortices. The interaction of tip vortices and the shed vortex sheet from the trailing edge plays an important role when evaluating near wake flow properties and hence on the rotors performance (Leishman, 2002). Depending on the rotational velocity of the rotor and the ambient velocity, these vortices describe a helicoidal trajectory or merge into a circular vortex sheet which is propagated downstream. Those vortical structures usually propagated at a lower speed than the local flow speed (Vermeer *et al.*, 2003) and have a strong influence on the near wake properties (Leishman, 2002). Several properties characterize the helicoidal vortex structure, e.g. the tip vortex path or wake expansion, vortex spiral twist angle and the strength of the tip vortices (Vermeer *et al.*, 2003). The vortex strength and the turbulence intensity of the ambient fluid are the main factors of how far downstream the vortices remain defined as single vortices

(Vermeer *et al.*, 2003). Eventually they catch up with their neighbour and merge into a vortex sheet. For experimental data for low turbulence intensities this can be seen at several diameter downstream (Hand *et al.*, 2001). But for numerical simulations it often occurs faster due to the presence of numerical dissipation because of the discretization scheme or a coarse meshe (Leishman, 2002) or (Ivanell *et al.*, 2009).

The shear layer created from the steep velocity gradients due to the tip vortices separates the ambient flow and the wakes inner flow (Crespo *et al.*, 1999). This shear layer also exhibits a very high turbulence intensity (Sanderse *et al.*, 2011). Due to convection and turbulent diffusion the initially thin shear layer at the rotor edge will smear out until it reaches the rotor axis. This region can extend up to five rotor diameter according to Vermeer *et al.* (2003) and is part of the transition towards the far wake region.

In the far wake the presence of the rotor shape is still felt by the reduced axial velocity component and a higher turbulence intensity (Sanderse *et al.*, 2011) than in the ambient flow. In absence of a sheared ambient flow (Vermeer *et al.*, 2003), the far wake obeys laws of self-similarity as demonstrated in Johansson & George (2006) for a downstream distance of more than $60R$. Despite the fact that this distance exceeds usual turbine distances used in the wind energy industry by a lot, many wake models are based on this assumption (Vermeer *et al.*, 2003).

While the rotor model is very important in the near wake in order to well represent the presence of a rotor, it becomes less important in the far wake where the wake model gains more significance according to Vermeer *et al.* (2003). While the focus of the near wake lies on the physical process of power extraction the far wake becomes important when wake interaction comes into play e.g. for turbine siting.

1.2 Rotor modelling

In order to represent the aerodynamics of the wind turbine and its impact on the flow, numerous methods of increasing computational complexity exist. In the first half of the last century the

Blade Element Momentum (BEM) method developed by Glauert (1935) provided an analytical solution which is, with certain variations applied, still used today for wind energy purposes (Hau, 2008). Then there are vortex methods well summarized in Schmitz & Chattot (2006) and finally fully resolved CFD simulations of wind turbines presented in Krogstad & Lund (2012), Bazilevs *et al.* (2011a), Bazilevs *et al.* (2011b) and Sørensen & Schreck (2012). The latter method delivers high fidelity results compared to the physical reality (Carrión *et al.*, 2015) at a high computational expense as the entire boundary layer over the blade surface is modelled. In Carrión *et al.* (2015) is also a detailed description of the wake turbulence characteristics.

While relying on CFD simulations also an alternative approach can be taken - the body force approach. Instead of considering the viscous effects on the blade surfaces, the forces associated with the rotor are calculated based on sampled velocities and airfoil coefficient data are calculated. Then they are projected in the computational domain in order to represent the rotor effect on the flow. This method is widely used when it comes to numerical simulations of wind turbines and numerous publications have been made on the topic (Sørensen & Shen, 2002; Troldborg, 2009; Shen *et al.*, 2009b).

Within the force approach a set of different methods exists, namely the actuator disk method (ADM), the actuator line method (ALM) and the actuator surface method (ASM), which will be discussed in the upcoming sections sections 1.2.1, 1.2.2 and 1.2.3.

1.2.1 Actuator disk method

Based on the works of Hough & Ordway (1964), the ADM was implemented by Mikkelsen (2004) for wind energy purposes. In the simple version (Hough & Ordway, 1964), the forces are azimuthally averaged over the circular plane swept by the rotor blades. Based on a sampled velocity, angle of attack and wind speed determine the lift and drag at each radial positions by the aid of the airfoil coefficients. The forces are inserted as momentum sink in the momentum equations of the Navier-Stokes (NS) equations. When applying the force in a discretized form in a CFD domain a thin disk with an one cell thickness is created as shown in Figure (1.2). The

abrupt changes across this disk introduces numerical oscillations at the point of the inserted force, which becomes a problem when the velocity at the disk is of interest. In order to get rid of this phenomenon a regularization such as the Gaussian kernel can be used (Mikkelsen, 2004). Another possibility would be to introduce the force as a pressure discontinuity as done by Rethore & Sørensen (2008).

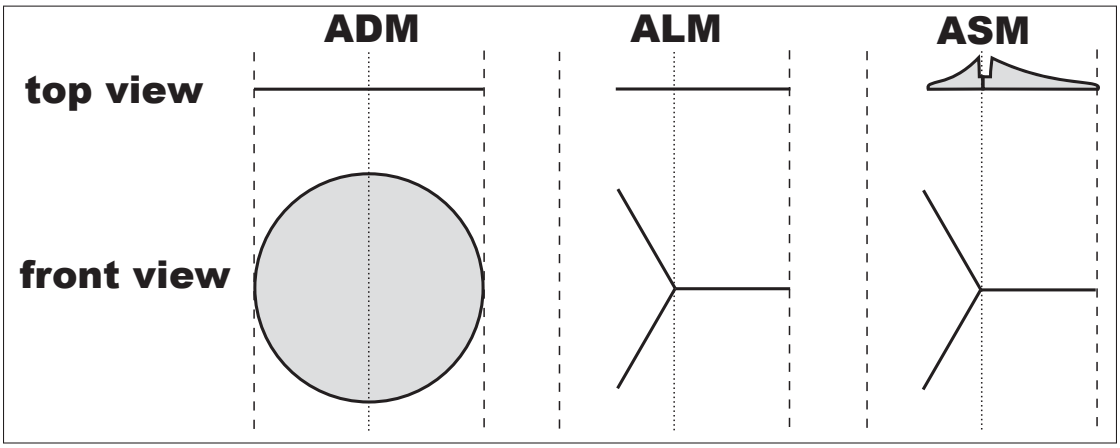

Figure 1.2 Different representations of a rotor with rotor circumference (dashed line) and center-line (dotted line).

By representing the rotor as a disk, instead of distinct tip vortices a vortex sheet is shed. Hence a correction was introduced by Prandtl at the time for the Blade Element Momentum (BEM) method in order to account for the finite blade number (Manwell *et al.*, 2010). This method was adapted in various ways in order to be integrated more easily within CFD methods by e.g. Shen *et al.* (2005) and Branlard & Gaunaa (2014).

The airfoil data used for the evaluation of the force is mostly derived from wind tunnel experiments with usually a fixed wing setup. Therefore this method can break for high angles of attack (AOA), as the stall effect for a fixed-wing occurs already at lower AOAs than for a rotating blade due to the stabilizing effects of the rotation (Leishman, 2002). Hence the same airfoil exhibits a higher maximum lift coefficient c_L for a wind turbine blade (Vermeer *et al.*, 2003). Due to the stochastic nature of the turbulent velocity field surrounding the rotor, stall often is an

intrinsic part of the wind energy extraction process (Vermeer *et al.*, 2003). Therefore a correction method is needed and several were proposed to redeem insufficiency of the available airfoil data and correct it for the 3D effects such as Coriolis force and centrifugal pumping Vermeer *et al.* (2003), such as Viterna & Janetzke (1982); Leishman & Beddoes (1989); Du & Selig (1998). Another aspect rarely covered by the available 2D airfoil data sets, is the hysteresis loop for higher AOAs according to Snel (1998); Leishman (2002); Vermeer *et al.* (2003).

A further enhancement of the airfoil data would be the extension beyond the limits of the angle of attacks of the experimental data. This is achieved by assuming the airfoil to be a flat plate (Viterna & Janetzke, 1982) beyond this point and thereby the set of airfoil data can be extended to a range of 360°. This approach is also used for helicopter aerodynamics (Leishman, 2002).

An alternative would also be to use generic airfoil data as done by Churchfield *et al.* (2013) instead of the actual airfoil data. This is particular interesting for the analysis of rotors where blade and airfoil data is not available.

1.2.2 Actuator line method

Inspired by the ADM approach a more sophisticated modelling of the wind turbine can be achieved by representing each blade as a line force as shown in Figure (1.2) and presented in Sørensen & Shen (2002). The angular momentum is not considered. Instead of shedding a vortex sheet as done by the ADM, the ALM sheds distinct tip vortices from each blade tip and a vortex sheet from the blade trailing edge enabling to simulate a more realistic interaction of the turbine with the flow in the near wake. As the forces are no longer azimuthally averaged, the rotation has to be taken into account in numerical simulations. It can be done via a rotating reference frame in Reynolds-Averaged Navier-Stokes (RANS) simulations as used in Nilsson *et al.* (2015) or by applying a transient method such as unsteady Reynold-Averaged Navier-Stokes equations (URANS) (Kalvig *et al.*, 2014). A very thorough description of an implementation of this method in conjecture with large-eddy simulation (LES) was laid out in Troldborg (2009).

Despite the presence of finite blade number and presence of the tips, Sanderse *et al.* (2011) and Shen *et al.* (2005) suggest to apply a tip correction when using unaltered 2D airfoil data. The reasoning behind that is that the influence of the particular flow situation around the blade tip on the resulting blade forces are not represented by the 2D airfoil data obtained usually from an experiment with an infinite wing configuration.

A particular challenge lies in the sampling of the velocities as the induction caused by the rotating blades makes it difficult to determine the optimal sampling location (Snel, 1998). This problem does not exist for the ADM as the sampling point can coincide with the point where the force will be applied. A possibility is to sample at the last location of the blade and therefore at a point where the induced velocity would be close to zero (Churchfield *et al.*, 2012). The value can then be obtained by either a gradient corrected version of the cell-center value (Churchfield *et al.*, 2012) or by a trilinear interpolation taking the adjacent cells into account (Troldborg, 2009).

The two most commonly used implementations of the ALM are found in EllipSys3D[1](Sørensen, 1995) and SOWFA[2] (Churchfield *et al.*, 2012) a project within OpenFOAM[3] (Weller *et al.*, 1998).

1.2.3 Actuator surface method

The ASM can be seen as an extension of the ALM, where the blades are not any longer modelled as lines, but extended chord-wise to surfaces immersed in the flow as shown in Figure (1.2). According to Vermeer *et al.* (2003) a chord-wise distribution of the inserted forces would ameliorate the near wake representation of the induced velocities. Different implementations exist as shown in Dobrev *et al.* (2007); Shen *et al.* (2009b); Sibuet Watters & Masson (2010).

[1] see: http://www.the-numerical-wind-tunnel.dtu.dk/EllipSys
[2] see: https://nwtc.nrel.gov/SOWFA
[3] Copyright 2004-2017 OpenCFD Ltd (ESI Group).

The first proposed method in Dobrev *et al.* (2007) is a hybrid between body force and pressure discontinuity. All forces tangential to the blade are inserted as forces in the NS equations and the normal force imposed by a pressure discontinuity. This results in an infinitely thin blade but also poses constraints on the computational mesh as it has to be aligned with the blades surface, which can be difficult for coned rotors or misalignment of rotor and flow direction (yawed flow).

Then there is the ASM proposed by Shen *et al.* (2009b) using entirely the body force approach. The pressure distribution on the surface is represented by body forces which are obtained using existing databases for pressure- and skin-friction distribution of airfoils and also the ones calculated by "XFOIL". The former algorithm solves the boundary layer equations around given airfoils as presented by Drela (1989).

Finally there is the work of Sibuet Watters & Masson (2010) where the effects of the rotating blades are represented by pressure and velocity discontinuities, which can be related to the circulation around the airfoil. By the aid of the Kutta-Joukowski theorem, a function for the circulation in dependence of the local lift coefficient can be derived. So the model contains elements of vortex methods as well as of the BEM theory. Besides the same limitations as experienced by the model of Dobrev *et al.* (2007) another shortcoming of this method comes with its usage of the Euler equations hence dropping the dissipation term and making it very similar to vortex methods such as the lifting surface method as described in Snel (1998). Similar approaches also had been undertaken by Snel (1998), Chattot (2011) and Schmitz & Chattot (2006). Although no drag is taken into consideration for this method, energy could still be extracted from the flow by the induced drag (Sanderse *et al.*, 2011).

As Vermeer *et al.* (2003) indicates when talking about vortex methods it would result in more realistic results when spreading the vorticity over a surface, e.g. using panel methods instead of methods based on single line vortex. At the same time this advantage would be more pronounced for low aspect ratio wings (Anderson, 2010) whereas wind turbine blades tend to have rather high aspect-ratio wings. In the case of the (NEW) MEXICO experiment (Schepers *et al.*,

2012) the aspect-ratio of mean chord over spanwidth is more than 20. Hence the better representation by ASM in comparison with the ALM would probably be more noticeable in the very near wake region.

1.3 Turbulence modelling

Most of the flows in engineering practice have a turbulent character, by the means of unsteadiness, three dimensionality and wide range of length and time scales (Tennekes & Lumley, 1972). In the case of the wind turbine several different origins of turbulence can be determined. First there is the turbulence of the ambient fluid, e.g. homogeneous isotropic turbulence in a wind tunnel or a shear layer turbulence in the atmospheric boundary layer. Second there is the turbulence originating from the boundary layers around blades, tower and nacelle. And finally the turbulence which stems from the breakdown of the helicoidal vortex structure.

One of the main phenomena of the turbulent flow is the vortex stretching which is caused by the shear of the main flow on the largest eddies in the flow. Due to the dominance of inertia effects at high length scales and therefore their quasi-inviscid character, the angular momentum is being conserved during stretching according to the law of Helmholtz. Therefore by stretching an eddy, its length scale is decreased and its velocity is increased, which automatically also decreases its time scale. By this mechanism smaller and smaller eddies are created and energy is passed down from the mean flow to eddies at smaller scale. Finally the eddy size is reaching the Kolmogorov scale (Pope, 2000).

At this level inertia and viscous effects become equal and the energy will be dissipated as internal energy of the flow. The creation of large eddies by the mean flow, their handing down of energy to smaller eddies and finally the dissipation of it at the smallest scales is called the energy cascade its consequence, the energy spectrum, is shown in Figure (1.3) (Pope, 2000).

The general form of the motion describing Navier-Stokes equations cannot be solved analytically so far due to the non-linear convection term. Hence there are several ways to obtain

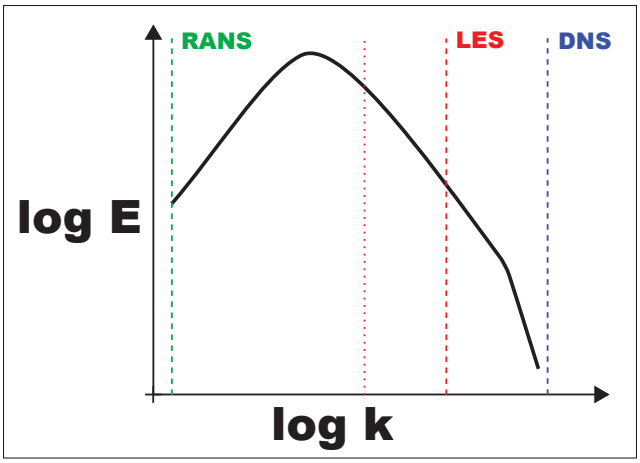

Figure 1.3 Energy spectrum as a function of the wavenumber k with scale representation due to different numerical methods (dashed line) in the energy spectrum with beginning of inertial sub-range (red dotted line).

approximative numerical solutions (Ferziger & Peric, 2012), of whom some will be discussed in the upcoming subsections.

1.3.1 Direct numerical solution

First there is the direct numerical solution (DNS) resolving all turbulent scales of the motion. Therefore no turbulence model is needed and numerical dissipation stems solely from the computational grid and the discretization schemes. As the Reynolds number is proportional to the range of eddy sizes occuring in the turbulent flow (Davidson, 2015), computational meshes become very fine even for simple low Reynolds number flows, as e.g. in Doran (2017). This leads to high computational costs and makes it unfeasible (Sanderse *et al.*, 2011) for wind energy application as there is a vast range of eddy sizes from the atmospheric boundary layer down to to the Kolmogorov scales close to the ground or on the wind turbine blades.

1.3.2 Large-eddy simulation

In large-eddy simulations (LES) a spatial filter is applied to the NS equations, which divides the fluid motion in a resolved part with the eddies of the size bigger than twice the filter with and a modelled part of all eddies smaller than the filter size as shown in Figure (1.3). The red dotted line is representing the beginning of the inertial sub-range, where the motion is assumed to be mainly isotropic. This approach relies on the fact that the large scale motion is mainly anisotropic and therefore depends on boundary conditions and geometry as discussed in Pope (2000). By directly resolving these structures an accurate representation of the larger scale motion is hoped to be obtained. The smaller (than filter-scale) motion is assumed to be isotropic and their main mechanism is the dissipation of energy which was handed down from larger eddies. A further discussion on this topic can be found in Sagaut (2006) and Lesieur *et al.* (2005).

The unresolved motion has to be modelled by a so-called sub-filter scale (SFS) model. As theoretically several different forms of filters can be used (Sagaut, 2006), the practise for CFD simulations is to use the grid as a box filter (Versteeg & Malalasekera, 2007). Therefore in the subsequent work instead of SFS the term sub-grid scale (SGS) model will be used.

As described in Speziale (1985) care should be taken when it comes to filtering and decomposition of the SGS stress tensor as there are approaches which do not exhibit Galilean invariance, which they should as it is one of the main basic properties of the NS equations and therefore models derived from these equations should inherent the same behaviour. So Germano (1992) presented a method whereas all components are consistent with the Galilean invariance.

The most widely used SGS model is the Smagorinsky model (Smagorinsky, 1963) which defines a turbulent SGS viscosity which is dependent on the mean strain rate. This is similar to the RANS approach where the turbulent effects are represented by the turbulent viscoity. As discussed in Mason (1994) the validity of this model breaks with the presence of a solid boundary as occurring in atmospheric boundary layers. The constant Smagorinsky coefficient, relating the sub-grid stress to the large-scale strain rate, causes an over-dissipation. There-

fore Smagorinsky models with a dynamic coefficient were proposed by Germano *et al.* (1991) and Fureby *et al.* (1997), where an additional coarser filter is used in order to determine the dynamic coefficient. Both these models rely on the assumption that the coefficient is scale invariant, which becomes invalid when approaching the solid boundary as shown in Porté-Agel *et al.* (2000) and causing an under-dissipation within the dynamic models. The latter article is proposing a scale-dependent dynamic model, which should remedy the known faulty behaviour of the previous SGS models. It could have been shown that the results ameliorated on a fundamental level when looking at the energy spectra, but at the same time it only contributes to minor changes when it comes to mean velocities. The dynamic Smagorinsky model as presented by Germano *et al.* (1991) relies on averaging on a homogeneous 3D space as in the case of decaying isotropic turbulence (Bautista, 2015) or on a plane parallel to the ground for a atmospheric boundary layer flow. The wake of a wind turbine is a less homogeneous flow and therefore the dynamic Lagrangian model (Meneveau *et al.*, 1996) could be advantageous as it averages over streamlines (Churchfield *et al.*, 2012).

1.3.3 Reynolds averaged Navier-Stokes approach

In order to ameliorate the computational costs the resolved scales can be reduced by a filtering process. The most popular method which also widely applied in industry focusing on aerodynamics (Spalart & Garbaruk, 2017), is the Reynolds-Averaged Navier-Stokes equation (RANS). Here a temporal filter is applied with a filter size of at least one turnover time of the largest eddy (Sanderse *et al.*, 2011). As shown in Figure (1.3) the cut in the turbulent spectrum would therefore occur at smallest wave length or largest eddy. Hence all fluctuating motion would have to be modelled and the RANS equations would represent only the mean velocities. In some cases the RANS filtering is done within the spectrum and thus the transient term is kept with an evolving mean velocity. This special case is called unsteady RANS (URANS) and also has some special applications as in Kalvig *et al.* (2014) or it serves in conjecture with another model in a hybrid method as e.g. presented in Bautista (2015).

When applying a temporal or spatial filter to the LES or RANS equations a closure problem arises from the non-linear convective term (Ferziger & Peric, 2012). In order to achieve closure the most common solution is the introduction of a turbulent viscosity added to the kinematic viscosity of the observed fluid. It represents the diffusive effects by the turbulent motion which is cut off by the filter. The turbulent viscosity is obtained by applying a turbulence model. One of the most important and widely used is the $k-\varepsilon*$[4] model as initially presented by Jones & Launder (1972). For aerodynamic purposes the $k-\omega*$ SST[5] (Menter, 1994) and the Spalart model (Spalart & Allmaras, 1994) proved to be very useful. An excellent overview of available models, their inner workings and usage can be found in Wilcox (2006). The assumption of a turbulent eddy viscosity (Boussinesq, 1877) depends on the mean strain rate and hence this assumption weakens when the mean strain rate undergoes sudden changes as for example at the boundary of a wake to the external flow.

1.4 Synthetic turbulence

1.4.1 Homogeneous isotropic turbulence

Many numerical simulations are conducted with an irrotational flow at the inlet of the computational domain as done e.g. by Nilsson *et al.* (2015). But when the rotor performance should be compared to experimental data from a real turbine in a wind tunnel or in the field, a turbulent inflow is needed in order to represent the respective flow conditions as done e.g. by Olivares Espinosa (2017).

In wind tunnel experiments, which are discussed more thoroughly in Section 1.5, often the inlet flow passes through a physical grid before entering the section containing the rotor. This ideally generates a homogeneous isotropic turbulence as e.g. in Comte-Bellot (1969). This means that the statistics of the turbulence is independent of direction (isotropy) and location in space (homogeneity) (Pope, 2000).

[4]The notation $(\cdot)*$ is used here in order not to cause confusion with the ALM distribution width parameter ε.
[5]The notation $(\cdot)*$ is used here in order not to cause confusion with the vorticity ω.

In the case of RANS modelling turbulence the flow variables represent mean variables, turbulence characteristics can be imposed directly at the boundaries, such as e.g. the turbulent kinetic energy and the dissipation rate for the classic $k-\varepsilon*$ model (Wilcox, 2006). Contrary to this in large eddy simulations turbulent flow structures are resolved, hence a synthetic turbulence field will be imposed at inlet boundaries as done by Olivares Espinosa (2017) or Muller (2015).

Therefore the challenge lies in generating a synthetic velocity field reproducing a realistic velocity field obtained by grid-turbulence. Several methods are used in wind energy research (Sanderse *et al.*, 2011) of which some will be presented here.

One of the first approaches was presented by Veers (1988)[6] and it takes the power spectral densities (PSD) and the coherence function as input. Further details are laid out in the report (Veers, 1988). This method was then adapted by Kelley (1992) and is used to this date in the "TurbSim" code[7] of NREL.

Another widely employed method was developed by Mann (1998)[8], where a velocity field is created based on the spectral tensor. Its first usage in numerical simulations of wind turbines was presented by Troldborg (2009) where planes of the velocity field were translated to body forces. Then these force were distributed and inserted at a plane downstream of the rotor. As it imposes velocity fluctuations on the incoming irrotational velocity field it can also be seen in a way as a modelling of a grid placed inside the flow.

Another very interesting approach was presented by Muller (2015) where wavelet transformations are used in conjunction with established methods like the Mann method. Here the transient aspects of the synthetic turbulence field are taken into account which can be of particular interest when it comes to ABL flow. In this method the generated velocity fields are applied on the inlet and lateral boundaries.

[6]The author references to it as the "Sandia method".
[7]See https://nwtc.nrel.gov/TurbSim
[8]Referenced to as "Mann method" in the wind energy research community.

1.4.2 Atmospheric boundary layer

The atmospheric boundary layer (ABL) with a height of the order of 1 km is the lower part of the troposphere, whose upper part is called free atmosphere which a height up to 10 km. The boundary layer is distinguished as the part of the troposphere which is directly influenced by the grounds surface by the means of a response time to ground forces of less than an hour as mentioned in Stull (2012). Having a no-slip condition imposed on the ground and the velocity of the free atmosphere on the top of the ABL, also known as the geostrophic wind, the pressure gradient is causing wind motion. Due to surface roughness, complex terrain and obstacles the wind flow undergoes perturbations which are finally resulting into a turbulent motion. Furthermore buoyancy effects caused by warm air rising due to solar heating of the earths surface are contributing to the wind flow.

The discussion of the ABL flow comes into play when the look is not only taken on the wake of one wind turbine but rather on a whole wind farm whose length is often exceeding the height of the ABL as mentioned in Calaf *et al.* (2010) and therefore even the large scale motion of the ABL has to be taken into account when looking at whole wind farms. The wakes have a significant impact on the overall performance of the downstream turbines, as the velocity deficits are causing a decrease in the extracted energy. In Meyers & Meneveau (2012) an optimal spacing of the wind turbines is discussed with taking the wakes into consideration. As RANS approaches are only able to give an time-averaged profile, transient approaches can determine also effects like wake meandering which can impose periodical velocity deficits on downstream turbines. This phenomenon is discussed in depth in Larsen *et al.* (2008) and España *et al.* (2011).

A brief discussion of appropriated SGS models for the ABL flow has already been given in the last section. It should be mentioned as well, that hybrid models were successfully used in the modelling of the ABL as shown in Bechmann *et al.* (2007), where LES is handling the flow phenomena far away from solid boundaries while the zone close to the ground is treated by a RANS approach with a $k-\varepsilon*$ model.

Other attempts of representing the ABL flow by a hybrid model was undertaken by Bautista (2015) by using a hybrid model between LES and $k-\omega*$ SST. In Nathan *et al.* (2014) this approach was combined with the ALM of SOWFA and compared to a non-turbulent flow and a homogeneous isotropic turbulent flow.

Besides physical representation of the ground by the aforementioned models, other approaches as presented by Mann (1998) introduce a synthetic turbulence field of a sheared flow. Numerical implementations within a CFD framework of this approach are presented in Muller (2015).

1.5 Experiments

A very detailed overview of wind tunnel experiments involving wind turbines is given by Vermeer *et al.* (2003) and a more recent update on the topic can be found in Sanderse *et al.* (2011). As laboratory scales are often much smaller scales than the ones of wind turbines used in wind farms (Snel, 1998), for the sake of similarity the Reynolds number $Re = \omega_{rot} Rc/\nu$, in terms of rotational velocity and chord, should be kept as close as possible between experiment and reality. So far these conditions were respected best for two experiments, the NASA Ames wind tunnel experiment (Hand *et al.*, 2001) and the MEXICO (Model experiments in controlled conditions) experiment (Schepers *et al.*, 2012).

While instrumentation for the NASA Ames experiment mainly consisted of pressure sensors on the blade, the MEXICO experiment added also PIV (Particle image velocimetry) data of up- and downstream region of the rotor which permits a study of the near wake besides the forces acting on the blades. Based on the set-up of the first round (Schepers *et al.*, 2012) a second round of the MEXICO experiment was conducted (Schepers & Boorsma, 2014), called "New MEXICO".

Here some shortcomings of the first round were addressed, such e.g. reflection of the nacelle distorting PIV recordings close to the hub, small PIV windows, lower wind tunnel velocities than specified etc.

1.6 Justification of the methodology

By reviewing the current scientific literature on the topic of wind rotor modelling in LES simulation under turbulent condition as presented in the former sections, several conclusions were reached.

In order to well represent the rotor and show the benefits of a ASM, the body force approach of Shen *et al.* (2009b) is chosen, as it firstly allows a seamless integration into existing numerical frameworks dealing with wind energy. A part from this practical aspect, methods such as Dobrev *et al.* (2007) and Sibuet Watters & Masson (2010), which are based on discontinuous jumps across cells of the computational domain, pose a meshing challenge especially in the presence of a solid wall and a rotating device. Although the method Sibuet Watters & Masson (2010) gave encouraging results in special cases (Breton *et al.*, 2012), the presence of turbulence when modelled by an eddy viscosity would be difficult when neglecting the diffusive term in the NS equations. Although Sibuet Watters & Masson (2010) permits meshes with much lower resolution than the approach of Shen *et al.* (2009b), this advantage can impair the behaviour of the shed tip vortices, as they are exposed to a stronger numerical dissipation than in the case of the pure body force approach.

For the flow modelling the LES is chosen due to the transient character of the near wake. Although RANS could also model the helicoidal vortex system behind the wind turbine by applying a rotating reference frame, but then the presence of a solid ground would be difficult to model and the integration into existing numerical frameworks for wind energy close to impossible. When it comes to the SGS model, a dynamic model is chosen over the standard Smagorinsky as it proves to be too dissipative. As there are no homogeneous box or plane, the dynamic Smagorinsky model proposed by Germano *et al.* (1991) is discarded and instead a Lagrangian model presented by Meneveau *et al.* (1996) is used. It allows the averaging over streamlines and hence the dynamic determination of the Smagorinsky coefficient under the here examined flow conditions. By the choosing a dynamic approach, the tip vortices and hence the vortex dynamics of the near wake will be better preserved.

When it comes to the turbulence modelling, the approach as presented by Olivares Espinosa (2017) and Muller (2015) will be followed. So instead of imposing the generated turbulence as a body force within the domain (Troldborg, 2009), the velocity field will be directly imposed as boundary conditions. The latter method seems to be the more direct approach, as once imposed the CFD simulation will already alter the field in dependence of grid resolution and numerical schemes. The former method seems to add another level of complexity by transforming the velocity field into a body force and then distribute it over the computational domain. On top of these two changes to the field also the CFD simulation will act upon as for the other approach. The alternative option of a precursor simulation is discarded as it involves high computational costs and would necessitate a wall-resolved LES.

The generation of the homogeneous isotropic turbulence will be the method of Mann (1998) as it has became quasi-standard for generating synthetic turbulence field in the wind energy community. The implementation by Gilling (2009) is used as it enforces a divergence free velocity field needed for the modelling of the incompressible NS equations. For the sheared turbulence the library of Muller (2015) will be used, as there is no need to model the flow close to the wall, which reduces the complexity of the mesh and the calculations by a lot.

CHAPTER 2

NUMERICAL METHODOLOGY

Based on the chosen methods in the previous chapter the numerical methodology applied throughout this work will be laid out in this chapter. It begins with a description of the numerical framework in Section 2.1 followed by how rotor forces are evaluated and introduced in the numerical simulations in Section 2.2. Then the description of the flow modelling is presented in Section 2.3 and the turbulence modelling in Section 2.4, where the generation and introduction of the synthetic homogeneous isotropic turbulence as well as the shear layer turbulence are discussed .

2.1 Numerical framework

This work is realized within the open-source framework OpenFOAM[1] (version 2.2.2) together with the SOWFA[2] project, which contains an implementation of the ALM as described in Troldborg (2009). A more detailed explanation for the implementation can be found in Martínez-Tossas *et al.* (2016).

OpenFOAM is an open-source collection of libraries and executables entirely written in C++ (Stroustrup, 2013). While the first released scientific article about the framework was by Weller *et al.* (1998) its inner workings are described more in-depth by Jasak (1996).

2.1.1 OpenFOAM

In OpenFOAM the computational domain is discretized by using the finite volume method (FVM), where the integral form of the governing equations is discretized over control volumes as shown in Figure (2.1a).

[1]OPENFOAM® (Open source Field Operation And Manipulation) is a registered trade mark of OpenCFD Limited, producer and distributor of the OpenFOAM software via wwww.openfoam.com.

[2]NWTC Design Codes (SOWFA (Simulator fOr Wind Farm Applications) by Matt Churchfield and Sang Lee) http://wind.nrel.gov/designcodes/simulators/SOWFA/. NWTC (National Wind Technology Center) is part of NREL (National Renewable Energy Laboratory) based in Golden, CO, USA.

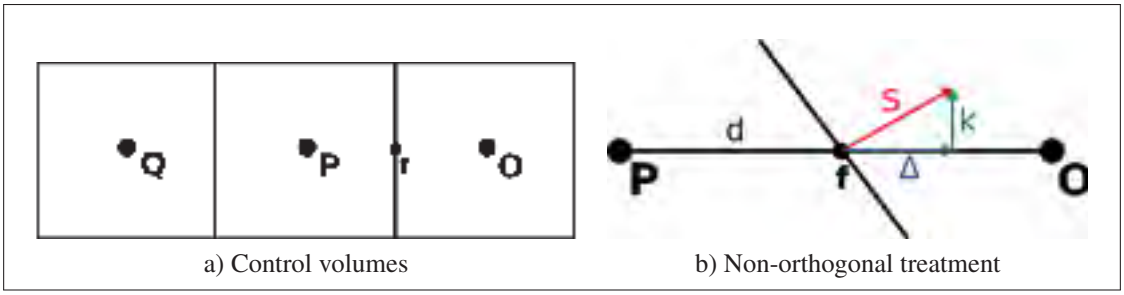

a) Control volumes b) Non-orthogonal treatment

Figure 2.1 Mesh discretization in OpenFOAM

A co-located grid arrangement is used, so all dependent variables are stored at the centroid P of the volume, hence

$$\int_{V_P} (\mathbf{x} - \mathbf{x}_P) dV = \mathbf{0} \tag{2.1}$$

The control volumes are general polyhedra bounded by flat faces where each face is shared with only one neighbouring volume. The face area vector $\mathbf{S}$ as depicted in Figure (2.1b) is normal to the face, its magnitude equals to the face area and its direction is pointing outward from the cell with the lower label index. The latter cell is called “owner” and the other cell is called “neighbour”. Boundary faces are always owned by the adjacent cell.

As for this work, the Mach number remains below 0.3, the incompressible form of the general transport equation can be used and written as

$$\frac{\partial \phi}{\partial t} + \nabla \cdot (\mathbf{U}\phi) - \nabla \cdot (\Gamma_\phi \nabla \phi) = S_\phi \tag{2.2}$$

whereas the integral form is given by

$$\int_t^{t+\Delta t} \left[\frac{\partial}{\partial t} \underbrace{\int_{V_P} \phi dV}_{\text{temporal term}} + \underbrace{\int_{V_P} \nabla \cdot (\mathbf{U}\phi) dV}_{\text{convective term}} - \underbrace{\int_{V_P} \nabla \cdot (\Gamma_\phi \nabla \phi) dV}_{\text{diffusive term}} \right] dt = \int_t^{t+\Delta t} \left(\underbrace{\int_{V_P} S_\phi dV}_{\text{source term}} \right) dt \tag{2.3}$$

In order to accurately discretize the second order terms of the dependent variable ϕ occurring in Eqn. (2.3) a second order method is needed (Ferziger & Peric, 2012). Hence the variation of $\phi(\mathbf{x},t)$ around P is assumed to be linear in time and space:

$$\phi(\mathbf{x}) = \phi(x_P) + (\mathbf{x} - \mathbf{x}_P) \cdot (\nabla\phi)_P \tag{2.4}$$

$$\phi(t + \Delta t) = \phi(t) + \Delta t \left(\frac{\partial \phi}{\partial t} \right) \tag{2.5}$$

According to the Taylor series expansion in space, the truncation error scales with $|(\mathbf{x} - \mathbf{x}_P)^2|$, so the approximation is therefore of second order. By the same method it can also be shown that the temporal discretization is of second order.

Discretization of transport equation

As the cell center P is the centroid (Eqn. (2.1)) of the control volume and together with the assumption of a linear variation (Eqn. (2.4)) the temporal term in Eqn. (2.3) can be discretized by

$$\begin{aligned}
\int_{V_P} \phi(\mathbf{x}) dV &= \int_{V_P} \left[\phi(x_P) + (\mathbf{x} - \mathbf{x}_P) \cdot (\nabla\phi)_P \right] dV \\
&= \phi_P \int_{V_P} dV + \left[\int_{V_P} (\mathbf{x} - \mathbf{x}_P) dV \right] \cdot (\nabla\phi)_P \\
&= \phi_P V_P
\end{aligned}$$

By using the Gauß' theorem the convective term in Eqn. (2.3) can be transformed as a sum over the faces f

$$\begin{aligned}
\int_{V_P} \nabla \cdot (\mathbf{U}\phi) dV &= \int_{\delta V} (\mathbf{U}\phi) \cdot d\mathbf{S} \\
&= \sum_f \int_f (\mathbf{U}\phi) \cdot d\mathbf{S}
\end{aligned}$$

with assuming a linear variation of $\mathbf{U}\phi$ it then follows

$$\begin{aligned}\sum_f \int_f (\mathbf{U}\phi)\cdot d\mathbf{S} &= \sum_f \left[(\mathbf{U}\phi)_f \cdot \int_f \mathbf{dS} + (\nabla(\mathbf{U}\phi))_f : \int_f (\mathbf{x}-\mathbf{x}_P) d\mathbf{S} \right] \\ &= \sum_f (\phi \mathbf{U})_f \cdot \mathbf{S} \\ &= \sum_f \phi_f F_{flux} \end{aligned} \tag{2.6}$$

with $F_{flux} = (\mathbf{U})_f \cdot \mathbf{S}$ as the flux through the cell face. The face values ϕ_f will be calculated from convection differencing schemes.

One widely used scheme can be derived by assuming a linear variation of ϕ between P and O with

$$\phi_f = f_x \phi_P + (1 - f_x)\phi_O$$

with f_x being the ratio distance $f_x = \frac{\overline{fO}}{\overline{PO}}$. This scheme is called central differencing (CD). It is second order, but only conditionally bounded as it causes numerical oscillations in convection-dominated flows.

An unconditionally bounded scheme is the upwind differencing (UD) where only the value of upwind node is considered. It can be stated as

$$\phi = \begin{cases} \phi_f = \phi_P & \text{for } F_{flux} \geq 0 \\ \phi_f = \phi_O & \text{for } F_{flux} < 0 \end{cases} \tag{2.7}$$

The boundedness is achieved at the expense of the accuracy, as UD is of first order accuracy and therefore reducing the order of accuracy of the discretization.

In order to obtain a compromise between the two schemes presented above, the blended differencing (BD) can be used. It can be e.g. a linear combination of CD and UD:

$$\phi_f = (1-\gamma)(\phi_f)_{UD} + \gamma(\phi_f)_{CD}$$

with a blending factor γ between 0 and 1. In this work a scheme is used which blends between 75% CD and 25% of a second-order UD scheme as presented by Warming & Beam (1976). The latter scheme corrects the upwind cell value by the gradient (for $F_{flux} \geq 0$) by

$$\phi_f = \phi_P + \frac{\phi_P - \phi_Q}{2}$$

with ϕ_Q as the value of the upstream neighbour of the upwind cell as shown in Figure (2.1a). In OpenFOAM terminology this scheme is called "Linear-upwind stabilized transport" (LUST). The diffusive term in Eqn. (2.3) is also discretized similarly to Eqn. (2.6)

$$\begin{aligned} \int_{V_P} \nabla \cdot (\Gamma_\phi \nabla \phi) dV &= \sum_f \mathbf{S} \cdot (\Gamma_\phi \nabla \phi) \\ &= \sum_f (\Gamma_\phi)_f \mathbf{S} \cdot (\nabla \phi)_f \end{aligned} \tag{2.8}$$

According to Figure (2.1b) in a purely orthogonal mesh with $\mathbf{d}$ and $\mathbf{S}$ parallel to each other it is possible to calculate the face gradient of ϕ via

$$\mathbf{S} \cdot (\nabla \phi)_f = |\mathbf{S}| \frac{\phi_O - \phi_P}{|\mathbf{d}|} \tag{2.9}$$

Alternatively the cell centered gradients could be calculated, e.g. for P

$$(\nabla \phi)_P = \frac{1}{V_P} \sum_f \mathbf{S} \phi_f$$

and the face gradient would be interpolated linearly by using these as following

$$\mathbf{S} \cdot (\nabla \phi)_f = \mathbf{S} \cdot [f_x (\nabla \phi)_P + (1 - f_x)(\nabla \phi)_O] \tag{2.10}$$

In an non-orthogonal mesh Eqn. (2.9) has to be split up in to an orthogonal contribution and in a non-orthogonal correction as shown in Figure (2.1b)

$$\mathbf{S} \cdot (\nabla \phi)_f = \Delta \cdot (\nabla \phi)_f + \mathbf{k} \cdot (\nabla \phi)_f \tag{2.11}$$

so the surface area vector $\mathbf{S}$ is constructed by its orthogonal part Δ and its non-orthogonal part $\mathbf{k}$.

For the minimal correction approach the orthogonal component is obtained by the projection of $\mathbf{S}$ on the distance vector $\mathbf{d}$:

$$\Delta = \mathbf{d} \cdot \mathbf{S} \frac{\mathbf{d}}{\mathbf{d} \cdot \mathbf{d}}$$

While the contribution from ϕ_P and ϕ_O diminish with increasing non-orthogonality with this approach, it remains constant for the orthogonal correction approach, where the orthogonal component is defined as

$$\Delta = \mathbf{S} \cdot \mathbf{S} \frac{\mathbf{d}}{\mathbf{d} \cdot \mathbf{d}}$$

In the over-relaxed approach the contribution is even increasing because Δ is defined as

$$\Delta = \frac{\mathbf{d}}{\mathbf{d} \cdot \mathbf{S}} (\mathbf{S} \cdot \mathbf{S})^2$$

The diffusion term as stated in Eqn. (2.8) is bounded and on orthogonal meshes this feature is preserved. The non-orthogonal correction can introduce unboundedness and therefore it is has to be limited in terms of stability at the expense of accuracy.

The orthogonal part for all three approaches can be calculated via

$$\Delta \cdot (\nabla \phi)_f = \Delta \cdot \Delta \frac{\phi_O - \phi_P}{\mathbf{d} \cdot \mathbf{d}}$$

The face gradient of ϕ can be calculated via Eqn. (2.10).

All terms which are not falling in the categories of convection, diffusion or temporal terms are treated as source terms in Eqn. (2.3). Its integral form with a linear dependency on ϕ can be written as

$$\int_{V_P} S_\phi(\phi) dV = SuV_P + \underbrace{SpV_P\phi_P}_{=0}$$

As the body forces are calculated explicitly before being inserted as momentum sink, the dependency term of the source term part is zero.

With all these discretizations of the different terms in Eqn. (2.3), the spatially discretized form of the transport equation can now be written as

$$\int_t^{t+\Delta t} \left[\left(\frac{\partial \phi}{\partial t} \right)_P V_P + \sum_f F_{flux}\phi_f - \sum_f (\Gamma_\phi)_f \mathbf{S} \cdot (\nabla\phi)_f \right] dt = \int_t^{t+\Delta t} SuV_P \, dt$$

According to Eqn. (2.5) the temporal derivative and the temporal integral can be calculated as

$$\left(\frac{\partial \phi}{\partial t} \right)_P = \frac{\phi_P^n - \phi_P^o}{\Delta t}$$
$$\int_t^{t+\Delta t} \phi \, dt = \frac{1}{2}(\phi^o + \phi^n)\Delta t$$

with $\phi_o = \phi(t)$ and $\phi_n = \phi(t+\Delta t)$. So the completely discretized form of the integral transport equation would be

$$\begin{aligned} \frac{\phi_P^n - \phi_P^o}{\Delta t} V_P + \frac{1}{2}\sum_f F_{flux}\phi_f^n - \frac{1}{2}\sum_f (\Gamma_\phi)_f \mathbf{S} \cdot (\nabla\phi)_f^n \\ + \frac{1}{2}\sum_f F_{flux}\phi_f^o - \frac{1}{2}\sum_f (\Gamma_\phi)_f \mathbf{S} \cdot (\nabla\phi)_f^o \\ = SuV_P \end{aligned} \tag{2.12}$$

This temporal discretization, which is used throughout this work, is called Crank-Nicolson method whose accuracy is of second order and using the face values of ϕ and $\nabla\phi$ as well as

the cell values for the old and new time level. The method is also unconditionally stable, but it does not guarantee boundedness (Ferziger & Peric, 2012).

So for every cell center P an equation of the form

$$a_P \phi_P^n + \sum_O a_O \phi_O^n = R_{res,P}$$

with the coefficient of the point a_P, neighbour coefficents a_O and residual $R_{res,P}$ can be constructed which finally leads to the following system of algebraic equations:

$$[A][\phi] = [R_{res}]. \tag{2.13}$$

Implementation of Boundary Conditions

The boundary conditions are prescribed on the faces coinciding with the domain boundary. There is the Dirichlet boundary condition represented by a fixed value, the Neumann boundary condition represented by a fixed gradient normal to the boundary face and a combination of each other. These boundary conditions can be built into the system of algebraic equations before its solution. The physical boundary conditions are e.g. symmetry planes, walls, inlets and outlets. Any of these conditions can be associated with a set of numerical conditions.

Solution Techniques for Systems of Linear Algebraic Equations

The system of linear algebraic equations in Eqn. (2.13) is normally solved by iterative methods as they are less expensive for large equation systems than direct methods. Iterative solvers need a diagonal dominant matrix for convergence, so that $|a_P| \geq \sum_n |a_O|$ for all lines and for at least one line $|a_P| > \sum_O |a_O|$ (Ferziger & Peric, 2012). The presence of source terms in this case augments the diagonal dominance as the body forces are calculated explicitly. This enhances the numerical stability of the simulation (Versteeg & Malalasekera, 2007).

On non-uniform meshes the contribution of the other neighbour cells according to Eqn. (2.11) introduces other sign coefficients, hence it creates unboundedness. Therefore the non-orthogonal contributions are also moved to the source term. This is leading to an additional loop for non-orthogonal correction as the non-orthogonal term is treated explicitly. The discretization of the temporal term is increasing the diagonal coefficient and adding a source, so it is increasing the diagonal dominance.

For the pressure equation as presented in the upcoming subsection, a generalized geometric-algebraic multi-grid (GAMG) is used (Versteeg & Malalasekera, 2007) and for the remaining equations such as the momentum and the turbulence closure a preconditioned bi-conjugate gradient solver (PBiCG) is used (Ferziger & Peric, 2012).

Iterative solution of discretized Navier-Stokes Equations

For discretizing the incompressible Navier-Stokes equations, whereas the momentum part becomes a specific equation based on the general form of the transport equation in Eqn. (2.2),

$$\frac{\partial \mathbf{U}}{\partial t} + \nabla \cdot (\mathbf{U}\mathbf{U}) - \nabla \cdot (\nu \nabla \mathbf{U}) = -\nabla p + \mathbf{F} \tag{2.14}$$

$$\nabla \cdot \mathbf{U} = 0 \tag{2.15}$$

two major challenges arise: the non-linearity stemming from the convection term and the pressure-velocity coupling. The former one will be addressed in Section 2.3. For the latter issue a non-linear solver or linear solver together with the linearization of the convection could be applied. Due to computational costs a linearization of the convection term is being used.

The convection term can be described as

$$\begin{aligned}\nabla \cdot (\mathbf{U}\mathbf{U}) &= \sum_f \mathbf{S} \cdot (\mathbf{U})_f (\mathbf{U})_f \\ &= \sum_f F(U_f) \\ &= a_P \mathbf{U}_P + \sum_O a_O \mathbf{U}_O\end{aligned}$$

where the coefficients a_P and a_O and the flux F are functions of $\mathbf{U}$. The momentum equation in Eqn. (2.14) can be discretized as

$$a_P \mathbf{U}_P = \mathbf{H}(\mathbf{U}) - \nabla p \tag{2.16}$$

whereas the pressure gradient is left out of the discretization as done in the Rhie-Chow interpolation (Rhie & Chow, 1983). The $\mathbf{H}$ term consists of the transport part, including the neighbour coefficients times the corresponding velocities, and the source part, including partly the transient term and all other source terms $\mathbf{F}$ apart from the pressure gradient:

$$\mathbf{H} = -\sum_O a_O \mathbf{U}_O + \frac{\mathbf{U}^o}{\Delta t} + \mathbf{F}$$

So Eqn. (2.16) can be used to obtain $\mathbf{U}_P$ by

$$\mathbf{U}_P = \frac{\mathbf{H}(\mathbf{U})}{a_P} - \frac{1}{a_P} \nabla p \tag{2.17}$$

The cell fluxes are then calculated via

$$\mathbf{U}_f = \left(\frac{\mathbf{H}(\mathbf{U})}{a_P} \right)_f - \left(\frac{1}{a_P} \right)_f (\nabla p)_f$$

With the discretization of the mass conservation in Eqn. (2.15)

$$\nabla \cdot \mathbf{U} = \sum_f \mathbf{S} \cdot \mathbf{U}_f = 0$$

the Eqn. (2.17) becomes

$$\nabla \cdot \left(\frac{1}{a_P} (\nabla p) \right) = \nabla \cdot \left(\frac{\mathbf{H}(\mathbf{U})}{a_P} \right)$$
$$\sum_f \mathbf{S} \left[\left(\frac{1}{a_P} \right)_f (\nabla p)_f \right] = \sum_f \mathbf{S} \cdot \left(\frac{\mathbf{H}(\mathbf{U})}{a_P} \right)_f$$

When this relation is satisfied, the face fluxes are guaranteed to be conservative.

The pressure-velocity coupling can be either achieved by solving the whole equation system simultaneously or by using a segregated approach which accounts for the coupling in another way, as done in the most popular methods such as SIMPLE and PISO.

The "Pressure Implicit solution by Split Operator method" (PISO) introduced by Issa (1986) is for the treatment of the pressure-velocity coupling for transient flows and it can be divided into the following steps:

- In the momentum predictor stage a solution of the momentum equation is obtained with the pressure field included explicitly, which gives an approximation for the new velocity field.
- In this step, called the pressure solution, a first estimate for the pressure field is calculated by solving the pressure equation including $\mathbf{H}(\mathbf{U})$, which could be constructed based on the predicted velocities.
- In the explicit velocity correction the velocity field is corrected explicitly as in Eqn. (2.17).

As the time step in transient simulations is presumably small, more importance is given to the pressure-velocity coupling than to the non-linearity of the system. Therefore the coefficients in $\mathbf{H}(\mathbf{U})$ are not re-evaluated although new conservative fluxes are available after each new solution of the pressure field. So $\mathbf{H}$ is only taken once in the momentum predictor stage in consideration, while a new pressure solution is derived at each loop during the pressure solution stage.

2.2 Rotor modelling

Instead of directly resolving the dynamics of the boundary layer surrounding the blades by representing its exact geometry in the computational domain, their effect is represented by a body force **F** in Eqn. (2.14). The derivation of this body force for the ALM and ASM, and its insertion in the computational domain will be laid out in Section 2.2.1 and Section 2.2.2 respectively.

2.2.1 Actuator line method (ALM)

As shown in Figure (2.2) the rotor blade is split in several segments with each represented by a centrally located actuator point.

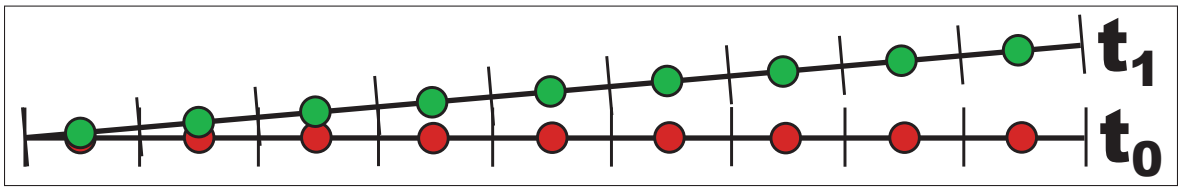

Figure 2.2 Schema of a blade representation using the ALM at previous timestep t_0 and current time step $t_1 = t_0 + \Delta t$. (red: t_0 and green: t_1)

The main steps of the ALM can be enumerated as follows

1. Velocities of the velocity field are sampled at the old actuator point locations, then the points are rotated.
2. Based on the angle of attack α the corresponding lift- and drag-coefficients c_l and c_d are looked up from the airfoil data of the current segment.
3. Lift and drag forces F_L and F_D for each actuator segment are calculated with eventually applying a tip correction f_{tip}.
4. Distribute force before inserting as source **F** in momentum equations.

and the numerical details are discussed in the upcoming subsections.

Velocity sampling and blade rotation

The velocity is sampled at the actuator point of the previous time step of the current velocity field as shown in Figure (2.2). The reason for sampling at the previous position is that it represents the center of the previously inserted force and hence should be the least affected by the field of induced velocities. Nevertheless due to this induction steep gradients exist in this region and therefore the velocity sampling always has been an issue of vivid discussion (Sanderse *et al.*, 2011). Other approaches exist where the velocity is sampled at an upstream position (Shen *et al.*, 2009b).

Steep gradients and the discrete nature of the computational domain result in a phenomenon when sampling the velocities. A trilinear interpolation is applied (Sørensen, 1995) to obtain the velocity value of the actuator point which almost never coincides with cell center point. Therefore even in absence of turbulent fluctuations of the inflow where a constant velocity would be expected, sampled velocities are oscillating around a mean value as shown in Figure (2.3)

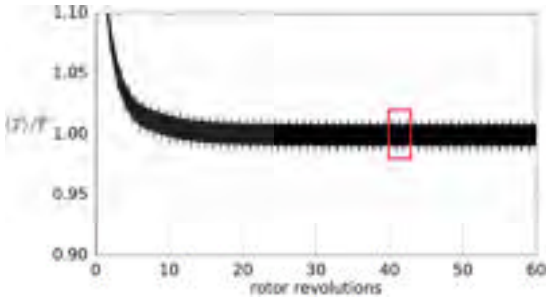

a) Whole simulation period

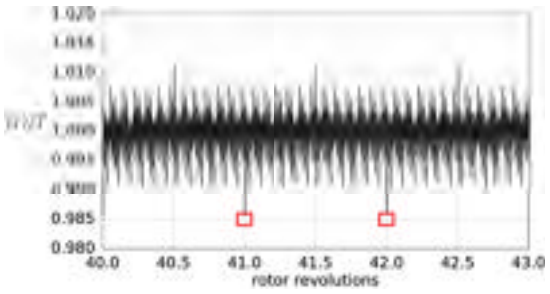

b) Selected simulation period (red box in Figure (2.3a)) showing recurring pattern.

Figure 2.3 Variation of normalized rotor torque $\langle T \rangle / T_{ref}$ over rotor revolution. The mean $\langle T \rangle$ is obtained via the lift forces acting on the rotor blades.

This oscillating sampled velocities then result in also oscillating blade forces causing something like a "numerical turbulence" to be created. This should be kept in mind when looking at momentum deficit and wake recovery.

In order to circumvent this issue several methods could be used in conjunction with the ALM. One could have a rotational reference frame as in Nilsson *et al.* (2015). This way the sampling point can always coincide with the actuator point and by adapting the mesh, making it even lie at the cell center hence no interpolation would be needed. Although this is an interesting approach and holds very well for a incoming potential flow, a rotational reference frame would cause problems with a homogeneous isotropic turbulent inflow as in Chapter 5 and would be almost impossible to combine with an ABL as discussed in Chapter 6.

Another way would be to proceed as Troldborg (2009) did and take multiple sampled velocities in a line parallel to the flow velocity up- and downstream of the blade and make an interpolation. This again is very viable for a potential flow, but in the presence of turbulence this would dampen out velocity fluctuations at the blade, hence deliver a much more stable torque than it actually would be.

Despite this problem and the different attempts to resolve it, its impact is judged to be rather small as can be seen in Figure (2.3b) and therefore neglected for now.

In this work the velocity U_s is sampled by correcting the cell center value of the cell containing the actuator point by the cell velocity gradient

$$\mathbf{U}_s = \mathbf{U}_P + \mathbf{d}_x \cdot \nabla U|_P \tag{2.18}$$

with the distance vector $\mathbf{d}_x$ between cell center and actuator point. By projecting the sampled velocity in the local reference of the blade as shown in Figure (2.4) the velocity magnitude U_{mag} can be obtained by

$$U_{mag} = \sqrt{(\mathbf{U}_s \cdot \mathbf{e}_n)^2 + (\mathbf{U}_s \cdot \mathbf{e}_t + \omega_{rot} r)^2} \tag{2.19}$$

with $\mathbf{e}_n$ and $\mathbf{e}_t$ as the unit vectors in the blade reference frame, and considering the rotational speed of the rotor ω_{rot} and the radial position r and the angle of attack α by

$$\alpha = \arctan\left(\frac{\mathbf{U}_s \cdot \mathbf{e}_n}{\mathbf{U}_s \cdot \mathbf{e}_t}\right) - \varphi_T - \varphi_P$$

with the twist angle φ_T and the pitch angle φ_P.

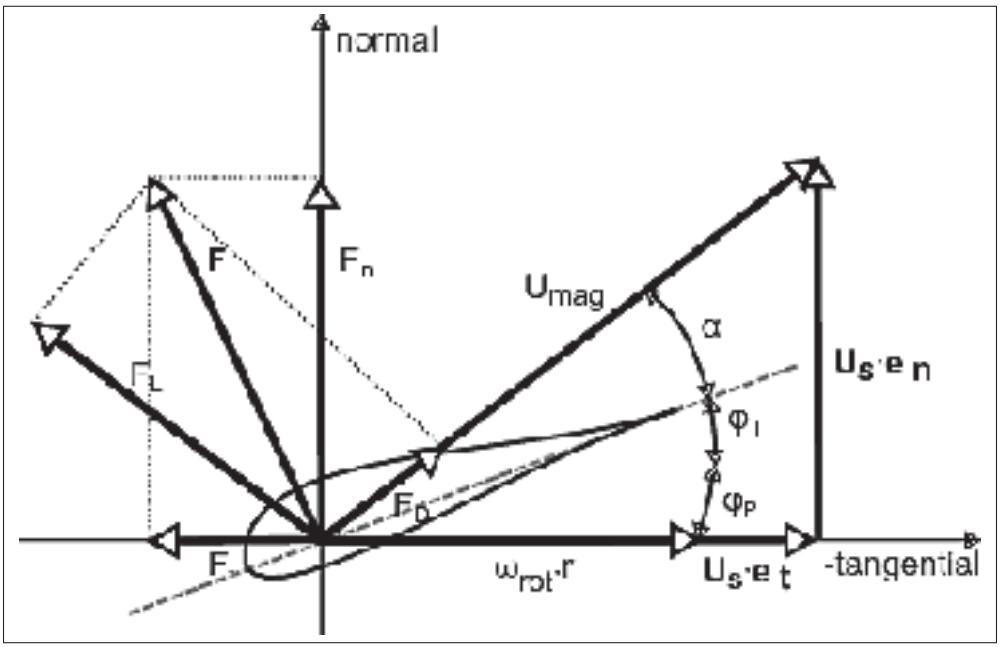

Figure 2.4 Geometry and forces in an airfoil section of the blade.

Then the actuator points are rotated by the matrix $\mathbf{R}$ defined as

$$\mathbf{R} = \begin{bmatrix} a_x^2 + (1-a_x^2)\cos\Delta\Psi & a_x a_y(1-\cos\Delta\Psi) - a_z\sin\Delta\Psi & a_x a_z(1-\cos\Delta\Psi) + a_y\sin\Delta\Psi \\ a_y a_x(1-\cos\Delta\Psi) + a_z\sin\Delta\Psi & a_y^2 + (1-a_y^2)\cos\Delta\Psi & a_y a_z(1-\cos\Delta\Psi) - a_x\sin\Delta\Psi \\ a_z a_x(1-\cos\Delta\Psi) - a_y\sin\Delta\Psi & a_z a_y(1-\cos\Delta\Psi) + a_x\sin\Delta\Psi & a_z^2 + (1-a_z^2)\cos\Delta\Psi \end{bmatrix}$$

around the axis $\mathbf{a}$ and by the angle $\Delta\Psi = \omega\Delta t$, whereas Δt represents the numerical time step. The actuator point of the new time step P_{new} is then obtained by rotating around the point $\mathbf{P}_0$

by

$$\mathbf{P}_{new} = (\mathbf{P}_{old} - \mathbf{P}_0) \cdot \mathbf{R} + \mathbf{P}_0.$$

Airfoil coefficients

As presented in Schepers *et al.* (2012) several tables for the airfoil coefficients exist in dependence of the blade Reynolds number, which is defined as

$$Re = U_{mag}\, c/\nu. \tag{2.20}$$

with U_{mag} as the velocity magnitude. When applied to the current blade configuration presented in Chapter 3 it can be seen in Figure (2.5) that towards the tip the tangential velocity dominates over the incoming normal flow[3] and hence the Re number remains at high level with $Re = 0.6 \cdot 10^6$.

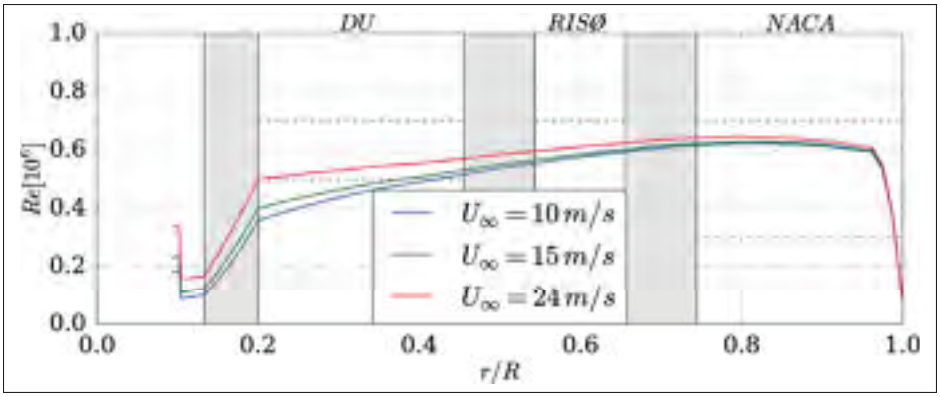

Figure 2.5 Blade Reynolds number in dependence of radial position. (gray area indicates transition zones)

[3]The abbrevations DU, RISØand NACA stand for Delft University, RisøNational Laboratory for Sustainable Energy and National Advisory Committee for Aeronautics respectively. They are discussed in more depth in Section 3.1.1.

In accordance to the local blade Reynolds at the radial positions the airfoil tables are selected for each airfoil, listed in Table (A-2) and visualized in Figure (2.6). This data was obtained due to wind tunnel experiments and therefore it does not include the stall delay due to boundary layer stabilizing effects such as Coriolis and centrifugal forcing which enhance the lift of the airfoil (Vermeer *et al.*, 2003). In the case of the MEXICO rotor an adaption was proposed by Shen *et al.* (2012) circumventing this issue as shown in Figure (2.6), but at the same time proposing a solution tuned for a known outcome.

There are also other methods including this lift-enhancing phenomenon such as correcting the airfoil data by applying the Du's method (Du & Selig, 1998) for the lift. Other possible corrections can be found in Viterna & Janetzke (1982) or Leishman & Beddoes (1989) which could be included in future work.

Another aspect are the limits of the available airfoil data in terms of range of the angle of attack. In this case the Viterna method (Viterna & Janetzke, 1982) is applied in order to extend the airfoil characteristics beyond the limits of angle of attacks imposed by experimental or numerical ("XFOIL") data by the help of a flat plate assumption (Viterna & Janetzke, 1982).

This work will relies exclusively on the original airfoil data obtained by wind tunnel experiments of finite wings as done in (Nathan *et al.*, 2017) in order to propose a generic solution and to determine up to which point they are reliable. This data is extended over a range of 360 deg with the help of the flat plate assumption.

With the help of the AOA α the lift- and drag-coefficients c_l and c_d are chosen from the selected airfoil table. In transition regions between the airfoils , a linear interpolation was implemented in order to permit a smooth transition of the airfoil data along the blade. While there is little difference in global results such as rotor torque and thrust as seen in Table (2.1), it smoothens the evaluted blade forces as can be seen in Figure (2.7).

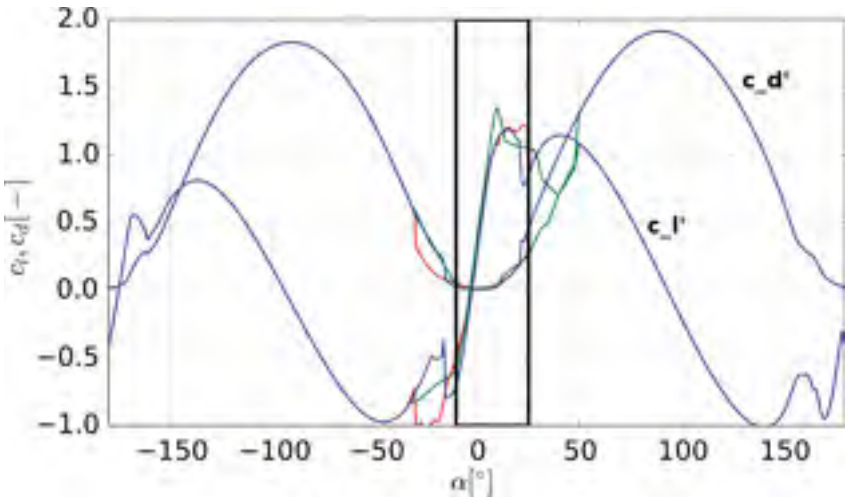

a) Entire range of angle of attack α

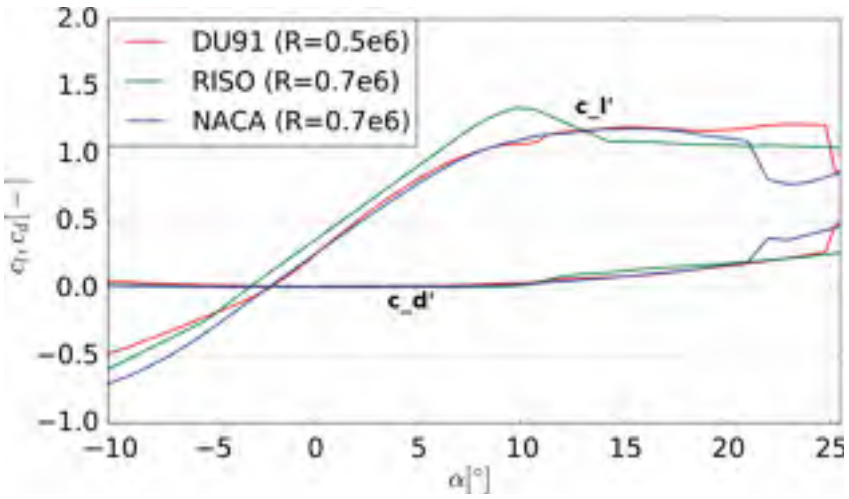

b) Selected range of angle of attack α (black box in Figure (2.6a)).

Figure 2.6 Airfoil coefficient data for MEXICO rotor simulations.

	Thrust (N)	Torque (Nm)
without transition	1615	310
with transition	1616	311
MEXICO experiment	1950	290

Table 2.1 Impact of blending between airfoil segments on rotor forces.

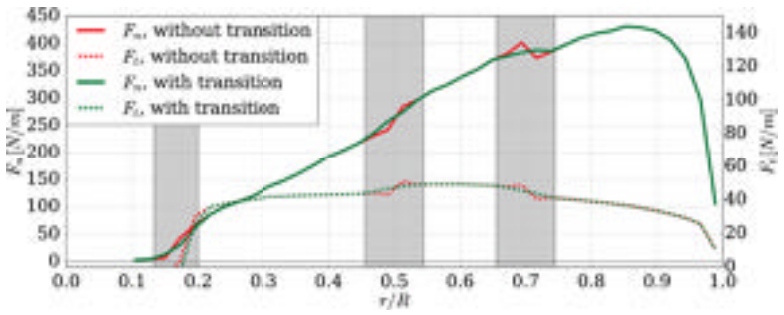

a) Blade forces.

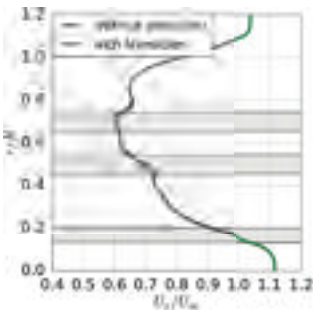

b) Normalized instantaneous velocity U_x/U_∞.

Figure 2.7 Impact on rotor calculations with and without transition zones between the airfoil sections.

Force calculation and tip correction

With the use of the airfoil data and the wind speed the lift and drag forces can be obtained by

$$F_L = \frac{1}{2}\, c_l\, U_{mag}^2\, c\, l_s$$
$$F_D = \frac{1}{2}\, c_d\, U_{mag}^2\, c\, l_s$$

with c_l and c_d as the lift and drag coefficients, U_{mag} as the velocity magnitude projected in the blade reference frame, c as the chord and l_s as the actuator segment width. Then the resulting punctual blade force $\mathbf{F_p}$ is obtained by

$$\mathbf{F_p} = f_{tip} \cdot (F_L \mathbf{e}_L + F_D \mathbf{e}_D) \tag{2.21}$$

together with an eventual tip correction f_{tip} (Glauert, 1935) defined as

$$f_{tip}(r) = \frac{2}{\pi} \cos^{-1}\left(\exp\left(-\frac{N_{blades}}{2}\frac{R-r}{r-\sin\left(\alpha(r)+\varphi_T(r)+\varphi_P(r)\right)}\right)\right)$$

with the blade number $N_{blades} = 3$, angle of attack α, twist angle φ_T and pitch angle φ_P. A similar correction is also applied for the root region. While intuitively a tip correction would

not be included in ALM simulation as tips and their associated vortices are present (Sanderse *et al.*, 2011) it strongly depends on the resolution of the computational domain as shown in Figure (2.8).

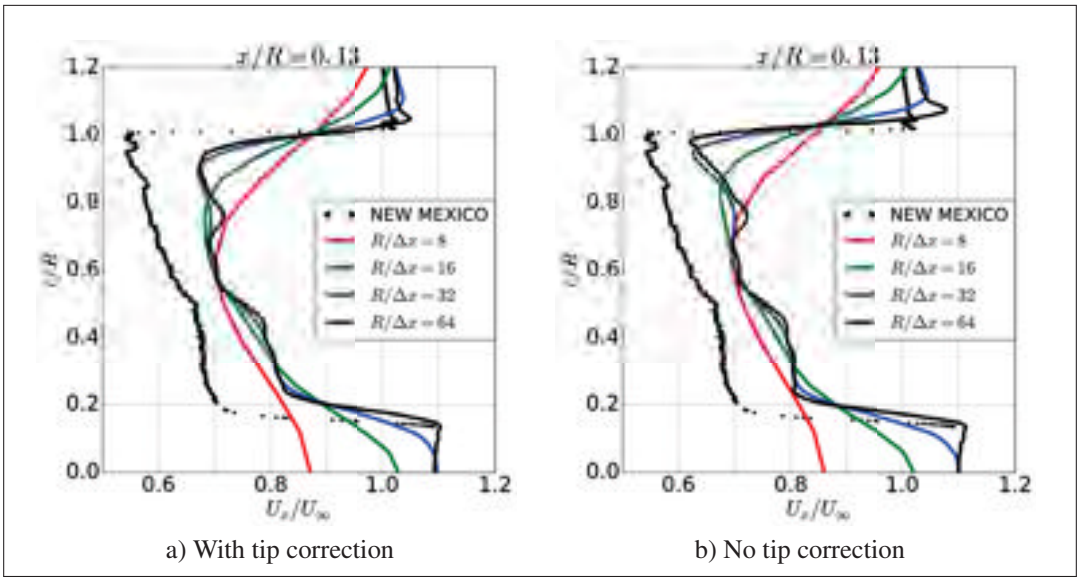

a) With tip correction b) No tip correction

Figure 2.8 Profiles of instantaneous normalized axial velocity component U_x/U_∞ with and without tip correction.

The influence of the resolution and the tip can be seen at $r/R = 1$ in Figure (2.8a) and Figure (2.8b) and it clearly shows that for a higher resolution $R/\Delta x \geq 32$ the tip vortex becomes distinct enough for inducing a more realistic velocity deficit. While at first sight, the case for high resolution without tip correction seems to behave well in the tip region, it should be noted that the sudden drop in velocity does not reflect in the experimental data. In fact, the case with a tip correction leaves to a velocity which has a constant offset to the experimental data, giving a systematic error but at least modelling the same behaviour. There the tip correction might be necessary for coarser resolutions in order to model a tip presence which is only weakly represented by the numerical simulation.

Force distribution

In order to avoid non-physical oscillations around the point of force insertion due to the sudden change the fluid is experiencing, the force has to be distributed which is achieved by a distribution kernel $\mathscr{G}$, so the final force $\mathbf{F}$ is given by

$$\mathbf{F} = \mathscr{G} * \mathbf{F_p}$$

with $()*()$ designating the convolution. Usually, as e.g. in Churchfield *et al.* (2012), a Gaussian distribution with a kernel

$$\mathscr{G}(r) = \frac{1}{\varepsilon^3\sqrt{\pi^3}} e^{-\left(\frac{r}{\varepsilon}\right)^2} \tag{2.22}$$

is chosen, where r is the distance from the point of the force and the point inside the Gaussian kernel and ε is the distribution width. In Troldborg (2009) a two-dimensional distribution is used arguing it gives a more realistic force representation at the blade tips. The reasoning is that three-dimensional distributions are smearing out the forces and therefore weaken the force of the created tip vortices. Using a two-dimensional distribution in this work lead to instabilities in the tip region, which result eventually in divergence. Therefore the 3D Gaussian kernel in Eqn. (2.22) is used throughout the work.

The distribution width is $\varepsilon = 2\Delta x$, with Δx as the width of the computational cell, as compromise between velocity oscillations and the regularization of the forces Troldborg (2009). Although Nilsson *et al.* (2015) uses $\varepsilon < 2\Delta x$, smaller values cause instabilities and eventually divergence within the here described framework.

When the blade is represented by forces distributed by a Gaussian Kernel as shown in Figure (2.9), it can be seen that due to the radius r as defined in Eqn. (2.23) and distance d of the Gaussian blob a certain region is not affected by the blade force although we assume the blade has smooth edges.

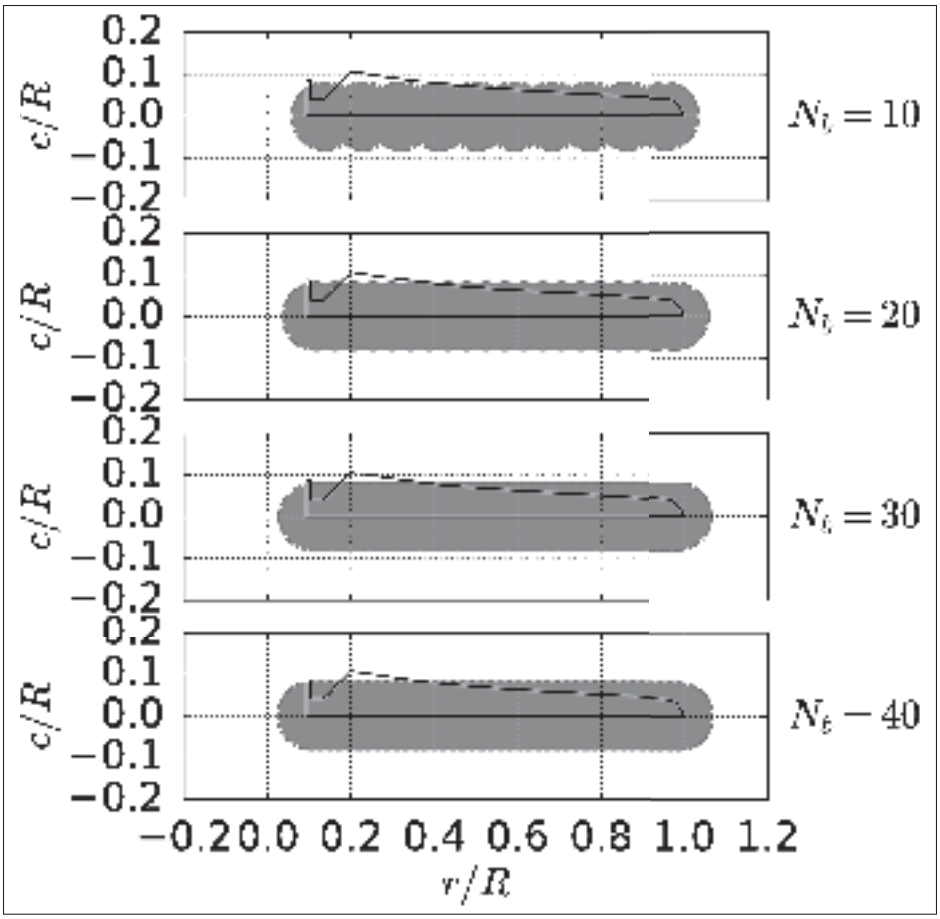

Figure 2.9 Blade force distribution as a function of the number of actuator points N_b

In order to calculate the porosity the blade forces are projected on a 2D plane as seen by the incoming flow and shown in Figure (2.10).

Then the porosity $c_{porosity}$ can be calculated via

$$\begin{aligned} c_{porosity} &= \frac{A_h}{A_t} \\ &= 1 - \frac{1}{2}\pi r^2 - r^2 \arccos\left(\frac{d}{2r}\right) + \frac{1}{4} d\sqrt{4r^2 - d} rd \end{aligned}$$

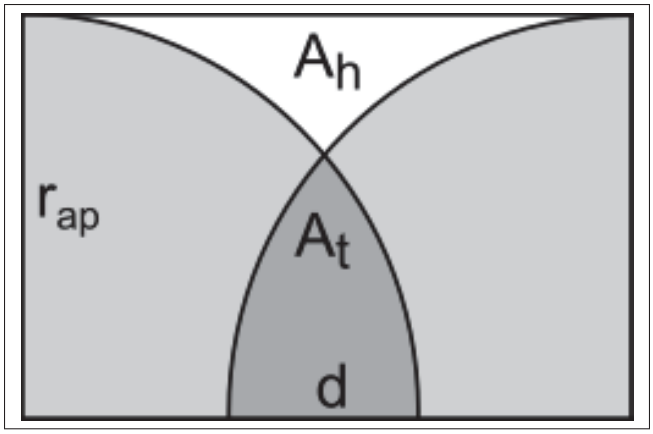

Figure 2.10 Geometrical definition for calculating the porosity $c_{porosity}$.

with

$$r = \varepsilon \sqrt{\log\left(\frac{1}{0.001}\right)} \tag{2.23}$$

$$d = \frac{R - R_{hub}}{N_b} \tag{2.24}$$

and $\Delta x = D/N$ it results in the porosity $c_{porosity}$ being a dependent function of the form

$$c_{porosity} = f(\varepsilon, R, R_{hub}, N, N_b) \tag{2.25}$$

When looking at global values such as e.g. the rotor torque listed in Table (2.2), it can be seen that for a resolution of $R/\Delta x = 32$, a distribution parameter $\varepsilon = 2\Delta x$ and a number of actuator points $N_b = 10$ the value of the torque reaches a stable level. But when taking a closer look

N_b	5	6	7	8	9	10	20	30	40	MEXICO
Torque (Nm)	166	220	260	286	301	312	312	311	310	290

Table 2.2 Rotor torque for ALM with different numbers N_b of actuator points.

at the downstream radial profile of the axial velocity component for this configuration as done in Figure (2.11), some slight oscillations are still visible for $N_b = 10$. Hence an actuator point

number of $N_b = 20$ resulting in a porosity of $c_{porosity} = 4.7\,\%$ will be preferred. Throughout the work it is always assured that the porosity remains below $5\,\%$.

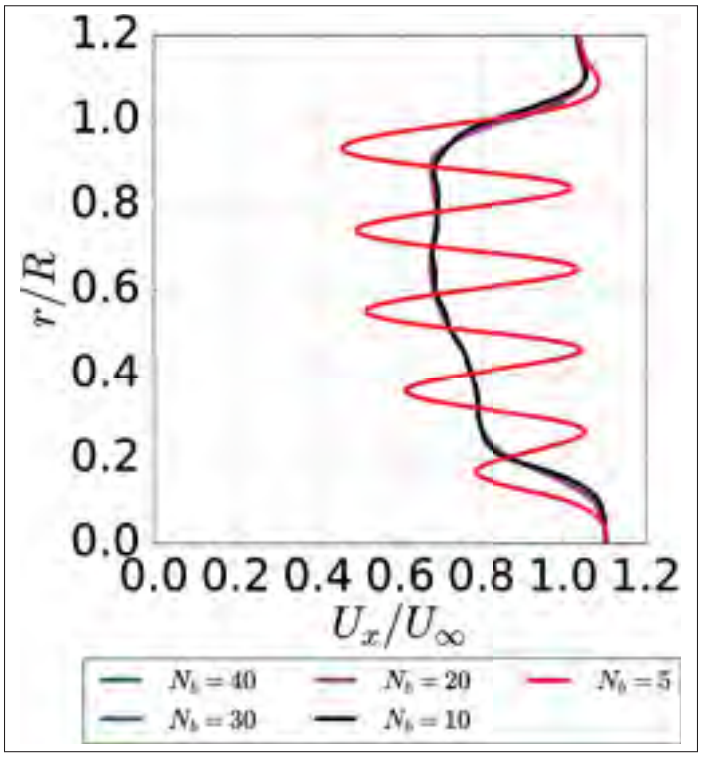

Figure 2.11 Rotor torque for ALM with different numbers N_b of actuator points with a grid resolution of $R/\Delta = 32$ and a distribution parameter of $\varepsilon = 2\Delta x$.

2.2.2 Actuator surface

The ALM implementation presented in the previous section can be extended to the ASM formulation presented by Shen *et al.* (2009b) as it also relies on body forces.

A first formulation of the ASM can be obtained by varying the distribution parameter ε as a function of the radial location r/R. When using the ALM with a constant ε a mesh refinement causes the shrinking of the volume over which the body force is applied as shown in Figure (2.12).

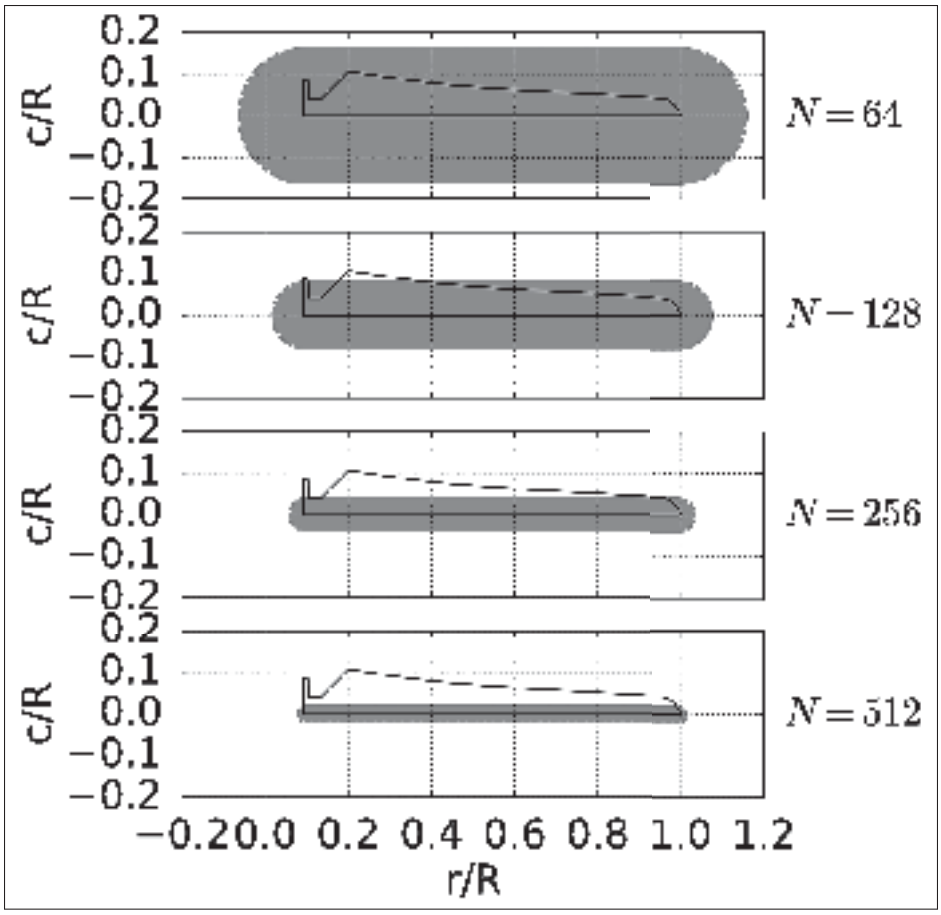

Figure 2.12 Blade forces in ALM with constant ε on different mesh resolutions with the number of cells N over one rotor diameter.

For a low resolution of $N \leq 64$ for one rotor diameter this means that the forces are distributed over a wide part of the computational domain and therefore the incoming fluid does not undergo as much change as it is supposed to. For very high resolutions $N \geq 256$ the body force volume becomes very small and the fluid experiences an only sudden bump leading as well to an under-prediction of the momentum deficit in the wake as seen in Figure (2.8a).

Therefore ε becomes variable with its smallest size $\varepsilon = 1.7\Delta x$ at the tip and varying towards the hub depending on the chord width. The kernel adjust itself to the chord width c as shown in Figure (2.13). It can be immediately seen that quite excessive resolutions with $N \geq 1024$ are needed to reproduce the blade shape using the body force distributions.

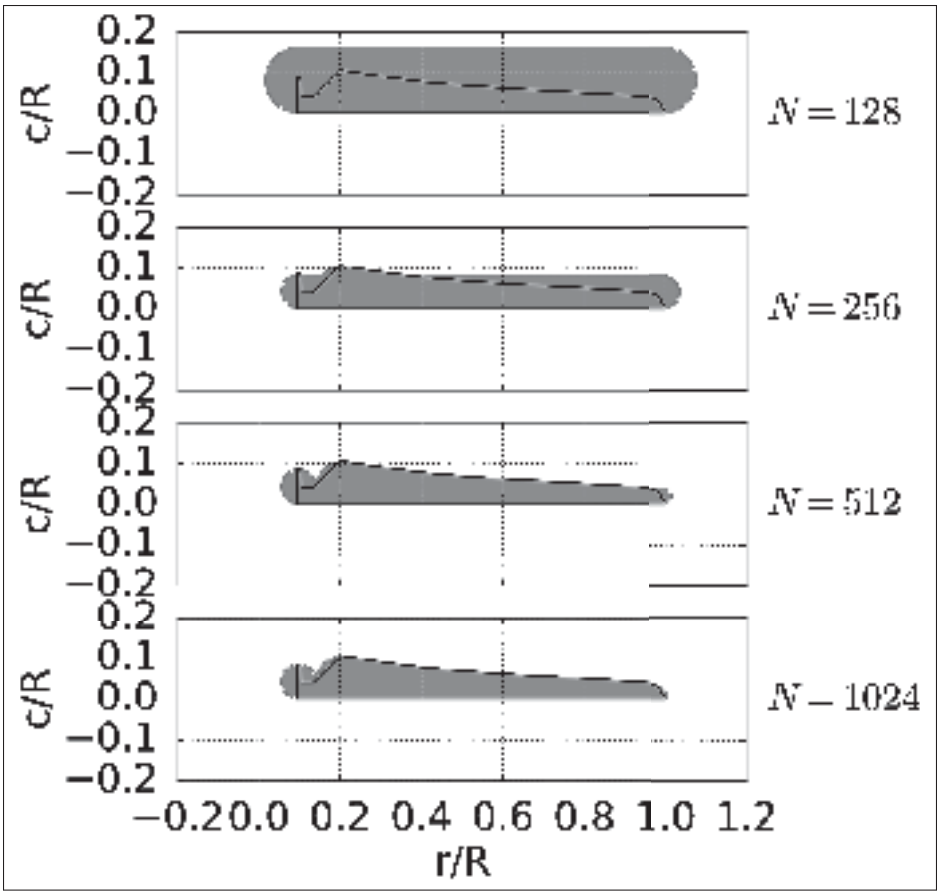

Figure 2.13 Blade forces in ASM with varying ε on different mesh resolutions depending on the blade chord.

If the thickness of the inserted force should also correspond to realistic values, the resolution must be even higher ($N = 4300$) as shown in Figure (2.14).

Instead of using the Gaussian approach, other approaches such as Sibuet Watters & Masson (2010) used a parabolic distribution or based on the C_P distribution derived from "XFOIL" results (Shen *et al.*, 2009a).

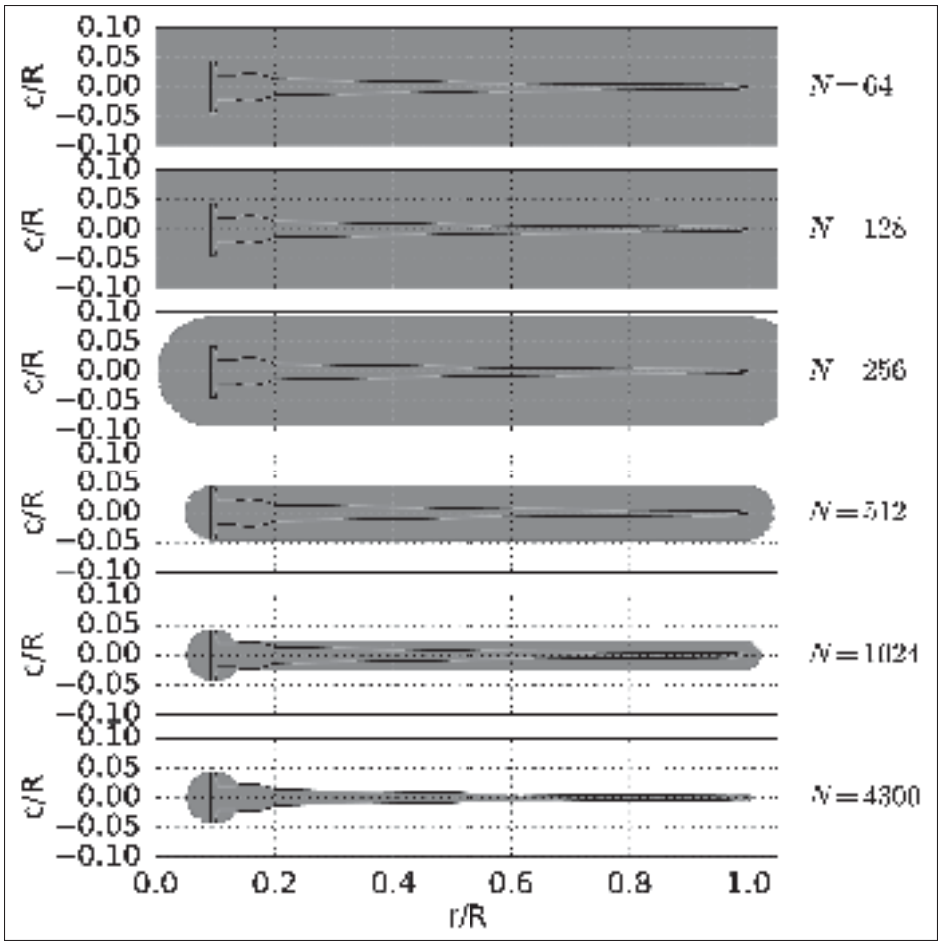

Figure 2.14 Blade forces in ASM with varying ε on different mesh resolutions depending on the blade thickness.

2.3 LES modelling

2.3.1 Filtering Navier-Stokes equations

In LES modelling a spatial filter is applied to the NS equations with the properties of linearity and conserving constants according to Sagaut (2006). In CFD simulations mostly the grid is used as implicit filter for the sake of convenience, hence the NS equations become according

to Pope (2000)

$$\frac{\partial \overline{u}_i}{\partial t} + \frac{\partial \overline{u}_i \overline{u}_j}{\partial x_j} = -\frac{\partial \overline{p}}{\partial x_i} + \frac{\partial}{\partial x_j}\left[\nu\left(\frac{\partial \overline{u}_i}{\partial x_j} + \frac{\partial \overline{u}_j}{\partial x_i}\right) - \tau_{ij}^{SGS}\right] + f_i \tag{2.26}$$

with $\overline{(\cdot)}$ as the filtered component and f_i as the components of the source term $\mathbf{F}$. The sub-grid stress τ_{ij}^{SGS} is defined as

$$\tau_{ij}^{SGS} = \tau^{SGS}(u_i u_j) = \overline{u_i u_j} - \overline{u}_i \overline{u}_j$$

furthermore the velocities can be split up in their resolved (non-filtered) and sub-grid (filtered) using the expression $\mathbf{u} = \overline{\mathbf{u}} + \mathbf{u}'$, which results in

$$\overline{u_i u_j} = \overline{(\overline{u}_i + u_i')(\overline{u}_j + u_j')} = \overline{\overline{u}_i \overline{u}_j} + \overline{\overline{u}_i u_j'} + \overline{u_i' \overline{u}_j} + \overline{u_i' u_j'}$$

By applying the filter a second time to the equation (2.26) and with $\overline{(\cdot)} = \overline{\overline{(\cdot)}}$ the turbulent stress can be defined as

$$\begin{aligned}\tau_{ij}^{SGS} &= \overline{u_i u_j} - \overline{\overline{u}_i \overline{u}_j} \\ &= \underbrace{\overline{\overline{u}_i u_j'} + \overline{u_i' \overline{u}_j}}_{C_{ij}} + \underbrace{\overline{u_i' u_j'}}_{R_{ij}}\end{aligned}$$

Resulting in a nonlinear term with twice filtered variables $\frac{\partial}{\partial x_j}(\overline{\overline{u}_i \overline{u}_j})$ in the filtered equation, Leonard proposed a triple decomposition as shown in Pope (2000) of the form

$$\begin{aligned}\tau_{ij}^{SGS} &= \underbrace{\overline{\overline{u}_i \overline{u}_j} - \overline{u}_i \overline{u}_j}_{L_{ij}} + \underbrace{\overline{\overline{u}_i u_j'} + \overline{u_i' \overline{u}_j}}_{C_{ij}} + \underbrace{\overline{u_i' u_j'}}_{R_{ij}} \\ &= \overline{u_i u_j} - \overline{u}_i \overline{u}_j\end{aligned}$$

As shown by Speziale (1985), the Galilean invariance rule is violated by the Leonard and the cross-stress tensor. As the original Navier-Stokes equation exhibits the property of the Galilean

invariance, so the unchanged variables with a reference frame under an uniform translation, also their filtered equations should exhibit this property. While the Leonard tensor representing the resolved scales is obtained numerically, the cross-stress tensor has to be modelled as it contains sub-grid stresses. So the decomposition as shown above would result in non-Galilean invariant models.

For adhering as well to Galilean invariance Germano (1986) proposes

$$\tau_{ij}^{SGS} = \mathscr{L}_{ij} + \mathscr{C}_{ij} + \mathscr{R}_{ij}$$

with

$$\begin{aligned}
\mathscr{L}_{ij} &= \overline{\overline{u}_i \overline{u}_j} - \overline{\overline{u}_i}\,\overline{\overline{u}_j} \\
\mathscr{C}_{ij} &= \overline{\overline{u}_i u'_j + u'_i \overline{u}_j} - \overline{\overline{u}_i}\,\overline{u'_j} - \overline{u'_i}\,\overline{\overline{u}_j} \\
\mathscr{R}_{ij} &= \overline{u'_i u'_j} - \overline{u'_i}\,\overline{u'_j}
\end{aligned}$$

2.3.2 SGS modelling

In numerical simulations information about the SGS scales are missing and therefore assumptions have to be made. A widely used approach is an eddy viscosity model which augments the effective viscosity in the NS equation by the eddy viscosity ν_{SGS}. It works similar to the turbulent viscosity model introduced by Boussinesq (1877), but instead of representing the effects by all fluctuations it is representing the effects of the filtered fluctuations.

Hence the SGS stress tensor can be rewritten as (Pope, 2000)

$$\tau_{ij}^{SGS} = 2\nu_{SGS}\overline{S}_{ij} + \frac{1}{3}\tau_{ii}^{SGS}\delta_{ij}$$

with the sub-grid scale viscosity ν_{SGS}. The second term on the right-hand side of the equation ensures that the sum of the modelled normal SGS stress corresponds the kinetic energy of the

SGS eddies (Versteeg & Malalasekera, 2007). The strain rate $\overline{S}_{ij}$ defined as

$$\overline{S}_{ij} = \frac{1}{2}\left(\frac{\partial \overline{u}_i}{\partial x_j} + \frac{\partial \overline{u}_j}{\partial x_i}\right)$$

and hence the SGS stress tensor becomes

$$\tau_{ij}^{SGS} = \nu_{SGS}\left(\frac{\partial \overline{u}_i}{\partial x_j} + \frac{\partial \overline{u}_j}{\partial x_i}\right) + \frac{1}{3}\tau_{ii}^{SGS}\delta_{ij}$$

When using this approach Eqn. (2.26) becomes

$$\frac{\partial \overline{u}_i}{\partial t} + \frac{\partial \overline{u}_i \overline{u}_j}{\partial x_j} = -\frac{\partial \overline{p}_m}{\partial x_i} + \frac{\partial}{\partial x_j}\left[(\nu + \nu_{SGS})\left(\frac{\partial \overline{u}_i}{\partial x_j} + \frac{\partial \overline{u}_j}{\partial x_i}\right)\right] + f_i \tag{2.27}$$

where the isotropic part of the stress tensor is included in the modified pressure term $\frac{\partial \overline{p}_m}{\partial x_i}$.

The most widely used SGS model to represent the eddy viscosity ν_{SGS} was introduced by Smagorinsky (1963) and it relates the strain rate of the resolved scales with a model constant C_s and the filter width Δ, which is the cell size in this case. The expression for eddy viscosity ν_{SGS} is formulated as

$$\nu_{SGS} = (C_s\Delta)^2\sqrt{2\overline{S}_{ij}\overline{S}_{ij}} \tag{2.28}$$

The default value for the Smagorinsky constant is set at $C_s = 0.167$. The disadvantage of this model is that it can be over-dissipative as shown e.g. in Porté-Agel *et al.* (2000) which can be problematic when representing small vortical structures such as the tip vortices. Therefore this model is only kept for comparison reasons.

To remedy this problem Germano *et al.* (1991) introduced a model where the model coefficient is evaluated dynamically (dynamic Smagorinsky model) based on the results on different grid

resolutions allowing to estimate the behavior of the sub-grid scales by using the expression

$$C_s^2 = \frac{\langle L_{mn} M_{mn} \rangle}{\langle M_{pq} M_{pq} \rangle} \tag{2.29}$$

with

$$L_{ij} = T_{ij} - \overline{\tau}_{ij}$$
$$M_{ij} = \frac{L_{ij}}{C_s^2}$$

where T_{ij} is the stress tensor on a grid twice as coarse as the actually resolved stress tensor τ_{ij} giving

$$T_{ij} = -2C_s^2 (2\Delta)^2 \widehat{\overline{S}}_{ij} \widehat{\overline{S}}_{ij}$$
$$\tau_{ij} = -2C_s^2 (\Delta)^2 \overline{S}_{ij} \overline{S}_{ij}$$

Therefore L_{ij} can be rewritten as

$$L_{ij} = 2\Delta^2 \left(\widehat{C_s^2 \overline{S}_{ij} \overline{S}_{ij}} - 4C_s^2 \widehat{\overline{S}}_{ij} \widehat{\overline{S}}_{ij} \right)$$

This approach allows a determination of the model coefficient based on the flow state without relying on a predetermined coefficient as within the classic Smagorinsky model. As it involves the averaging over statistical homogeneous directions such as e.g. planes parallel to the wall as done in Germano *et al.* (1991) or Piomelli (1993) or in the span-wise direction in the backward facing step flow (Akselvoll & Moin, 1993). With a rotor immersed in the flow it becomes more difficult to define a statistical homogeneous direction.

Hence the Lagrangian dynamic SGS model (Meneveau *et al.*, 1996) is used for this work. Instead of averaging over planes or spaces which proves to be difficult in inhomogeneous flow situations, it averages over flow pathlines where the name of model stems from. It basically relies on Eqn. (2.29) for determining the model coefficient C_s dynamically at each simulation

time steps, but by following the fluid-particle trajectories it introduces the expression

$$C_s^2 = \frac{\mathfrak{F}_{LM}}{\mathfrak{F}_{MM}} \tag{2.30}$$

with the integrals over the trajectories defined as

$$\mathfrak{F}_{LM}(\mathbf{x},t) = \int_{-\infty}^{t} L_{ij}M_{ij}(\mathbf{z}(t'),t')W(t-t')dt' \tag{2.31}$$

$$\mathfrak{F}_{MM}(\mathbf{x},t) = \int_{-\infty}^{t} M_{ij}M_{ij}(\mathbf{z}(t'),t')W(t-t')dt' \tag{2.32}$$

where $W(t-t')$ is a parameter to which extent the pathline should be followed backwards. When defining this weighting function as an exponential form as done in Meneveau *et al.* (1996) as $W(t-t') = T_{lagDyn}^{-1} e^{-(t-t')/T_{lagDyn}}$ the expressions in Eqn. (2.31) and Eqn. (2.32) will be solutions to the following equations

$$\frac{\partial \mathfrak{F}_{LM}}{\partial t} + \mathbf{u}\cdot\nabla\mathfrak{F}_{LM} = \frac{1}{T}(L_{ij}M_{ij} - \mathfrak{F}_{LM}) \tag{2.33}$$

$$\frac{\partial \mathfrak{F}_{MM}}{\partial t} + \mathbf{u}\cdot\nabla\mathfrak{F}_{MM} = \frac{1}{T}(M_{ij}M_{ij} - \mathfrak{F}_{MM}) \tag{2.34}$$

The time scale T_{lagDyn} is used to control the Lagrangian averaging and it is defined as

$$T_{lagDyn} = \theta\Delta(\mathfrak{F}_{LM}\mathfrak{F}_{MM})^{-1/8} \tag{2.35}$$

with the parameter $\theta = 1.5$ as proposed in Meneveau *et al.* (1996).

2.4 Turbulent flow generation

2.4.1 Homogeneous isotropic turbulence

Generation of synthetic turbulence field

A synthetic velocity field representing homogeneous isotropic turbulence based on the von-Kármán energy spectrum (Pope, 2000)

$$E(k) = \alpha\varepsilon^{2/3}L^{5/3}\frac{L^4\kappa^4}{(1+L^2\kappa^2)^{17/6}} \tag{2.36}$$

is obtained by using the algorithm proposed by Mann (1998). The technical details can be found in its initial article of Mann (1998) or more recently in Olivares Espinosa (2017). The main parameter for this approach are the integral length-scale L and the coefficient $\alpha\varepsilon^{2/3}$ which can be used as a scaling parameter in order to obtain the desired amplitude of the fluctuating velocities. The wavenumber κ depends on the grid resolution and dimension and therefore the ability of the numerical mesh to resolve a certain range of turbulent scales.

While several implementations of this method exist e.g. Olivares Espinosa (2017) or Muller (2015), the implementation of Gilling (2009) was chosen for the generation of HIT for several reasons. It is open-source and permits the imposing of HIT at the boundaries at relatively low computational cost.

In Figure (2.15) the midplane of a generated turbulent field is shown for different turbulence intensities. The flow structures are identical apart from the different scaling of the velocity fluctuations. This results from using the same seed for the random number generator in the Mann algorithm and by scaling the obtained velocity field with $\alpha\varepsilon^{2/3}L^{5/3}$ for obtaining the desired TI_{syn}.

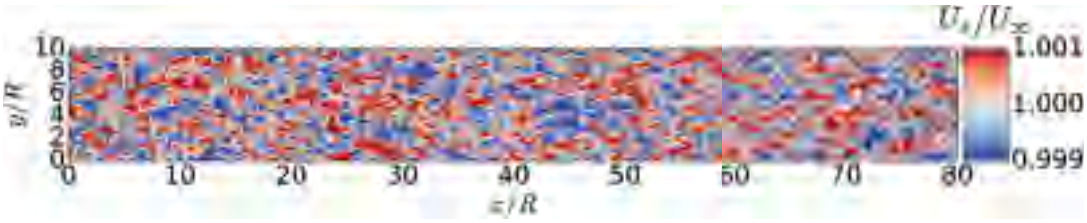

a) $TI_{syn} = 0.1\,\%$

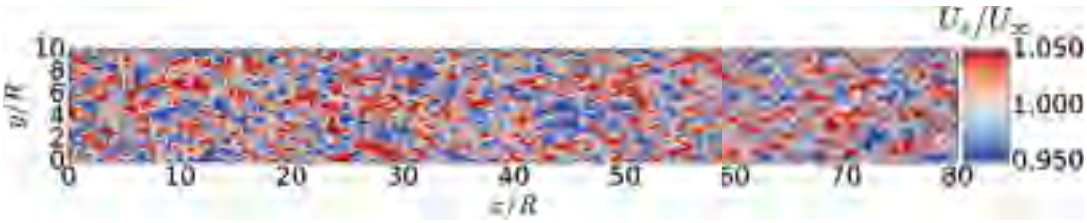

b) $TI_{syn} = 5\,\%$

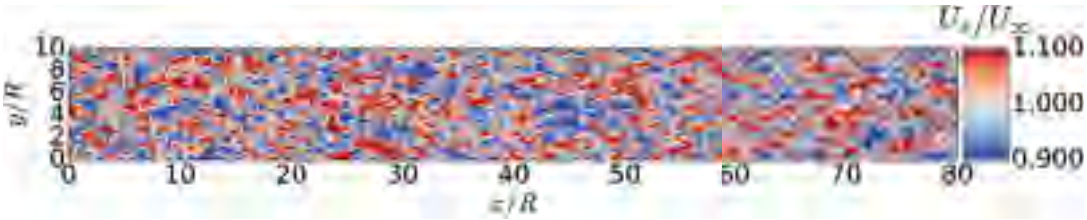

c) $TI_{syn} = 10\,\%$

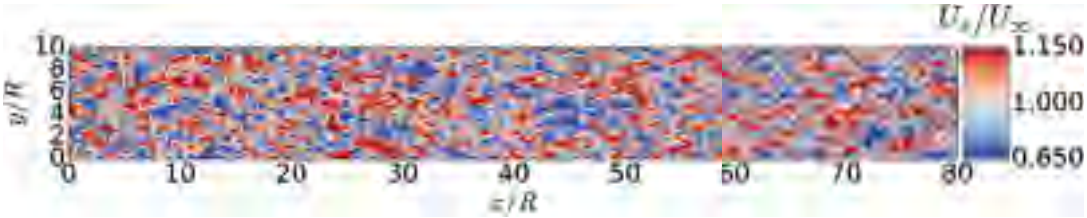

d) $TI_{syn} = 15\,\%$

Figure 2.15 Midplanes of synthetic turbulence boxes for different turbulent intensities.

Imposing HIT as boundary condition

Different methods can be found for imposing the synthetic turbulence in the computational domain, such e.g. Troldborg (2009), Muller (2015) and Olivares Espinosa (2017). In Olivares Espinosa (2017) it can be seen that there are difficulties when translating the incoming velocity field to a force by the aid of the NS equations and imposing it as a momentum source.

First there is a loss of accuracy as the force has to be distributed over several cells in order to avoid spurious oscillations in the solution as already discussed for the rotor force in Section 2.2. This aspect together with the strong decay throughout the domain in CFD simulations conducted with EllipSys3D as shown inOlivares Espinosa (2017), leads to the conclusion that different methods should be explored as well.

A further enhancement could be a mixed boundary condition where the field is not imposed by blending a Dirichlet condition and a Neumann-condition. This is due to the fact that once the synthesized velocity field enters the computational domain it evolves differently in respect to its synthetic counterpart. Hence strong velocity gradient appear in the cells adjacent to the boundaries where the velocity is imposed.

In this work the generated turbulence is imposed solely at the inlet as shown in Figure (2.16). Therefore a new boundary condition was written, which reads the generated velocity fields and imposes them on the inlet face. As the resolution of the synthetic turbulence field and the computational grid do not coincide as explained further in Chapter 5, a trilinear interpolation was used to obtain the desired value at each face center. A second tool was conceived to initialize the velocity field for t_0 as shown in Figure (2.16) in order to accelerate statistical convergence and hence lower the total necessary run-time.

So initially a part of the synthetic turbulence box with the length of the computational domain L_x is imposed as initial condition. Then at every timestep the current axial position within the synthetic velocity field is evaluated by taking the current run-time and the mean velocity into consideration.

2.4.2 Atmospheric boundary layer

The method proposed by Mann (1998) also offers the generation of sheared flow and it delivers good results in agreement with the Kaimal spectrum as shown in Muller (2015) and Olivares Espinosa (2017). A typical flow field generated by this algorithm can be seen in Figure (2.17).

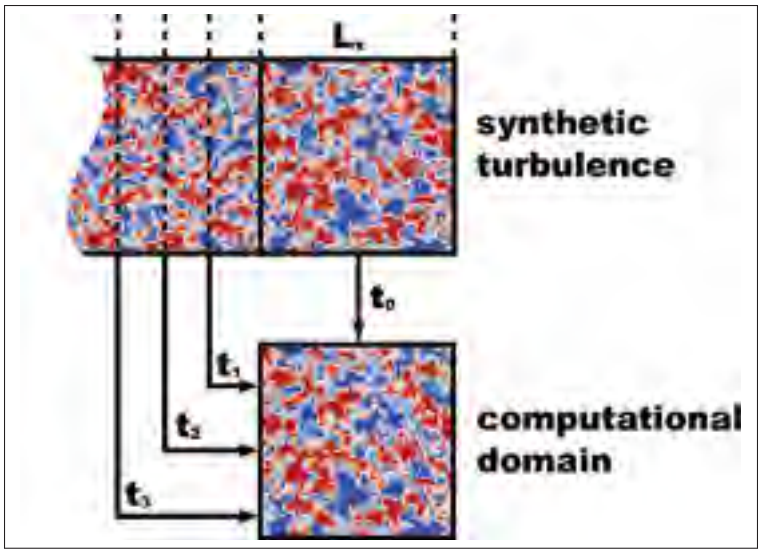

Figure 2.16 Initialization and boundary condition of computational domain by the means of synthetic turbulence field for the case of homogeneous isotropic turbulence.

It should be noted that the mean velocity profile is obtained via the power law

$$U_x = U_{ref}\left(\frac{z}{z_{ref}}\right)^{\alpha_p} \tag{2.37}$$

hence the velocity at the bottom of the domain does not necessarily have to be zero depending on the domain dimensions. The reference height z_{ref} was set at hub height and the reference velocity was set at $U_{ref} = 15\,m/s$. The parameter α_p can be deduced from experimental measurements if available. In this case they were not available, hence for neutral conditions often $\alpha_p = 1/7$ is used.

The main challenge here is rather how to impose the synthetic turbulence as the velocity field is propagated by a non-uniform mean speed in the vertical direction. Therefore the top of the velocity field moves at a faster pace than the part close to the ground. This results in the need of a vast synthetic turbulence field in order to cover a modest domain size and also a high mismatch between the synthetic turbulence field and its representation in the computational

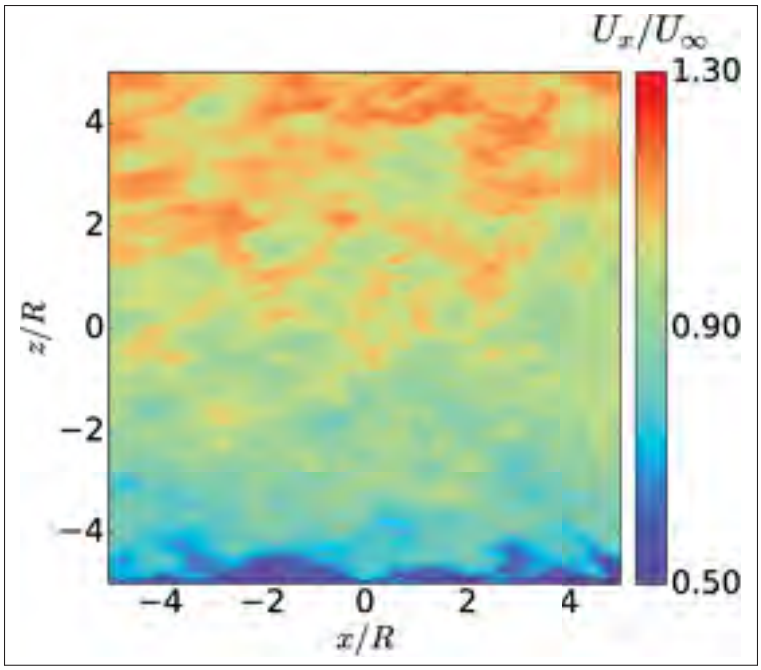

Figure 2.17 Vertical plane of synthetic turbulence field for the case of sheared turbulence obtained by the code of Muller (2015).

domain would occur as the generated field would not take into account the dynamic evolution of the turbulent structures.

In order to remedy this problem Muller (2015) combined the method of Mann (1998) with wavelet transformation obtaining an approach which imposes the synthetic velocity field of a sheared turbulence taking into account the dynamical evolution at each timestep. The downside of this method is the significant increase in demand of computational resources as shown in Figure (2.18).

The base case was run at a lowest processor number of 24 and hence the subsequent runs were made on multiples of 24 processors[4]. It shows that the cases without turbulence and with HIT show a linear speedup which indicates an huge parallel portion of at least 90% of the code according to Amdahl (1967). No tests above a processor number of 144 were conducted as the

[4]Most of the simulations were run at the HPC cluster Guillimin which is part of Compute Canada national HPC platform. The cases were run on nodes consisting of 2 Dual Intel Westmere EP Xeon X5650 processors (each 6-core, 2.66 GHz, 12MB Cache, 95W).

job waiting time in the process queue would be out of proportion in relation to the time gain of the simulation.

In contrast the code of Muller (2015) flattens out at already a speed-up of 3 which indicates a parallel portion somewhere between 50% and 75% which leaves a lot of room for improvement. This also has to be taken into account when choosing the number of processors as starting from 96 (4x24) additional processor do almost not reduce total run time.

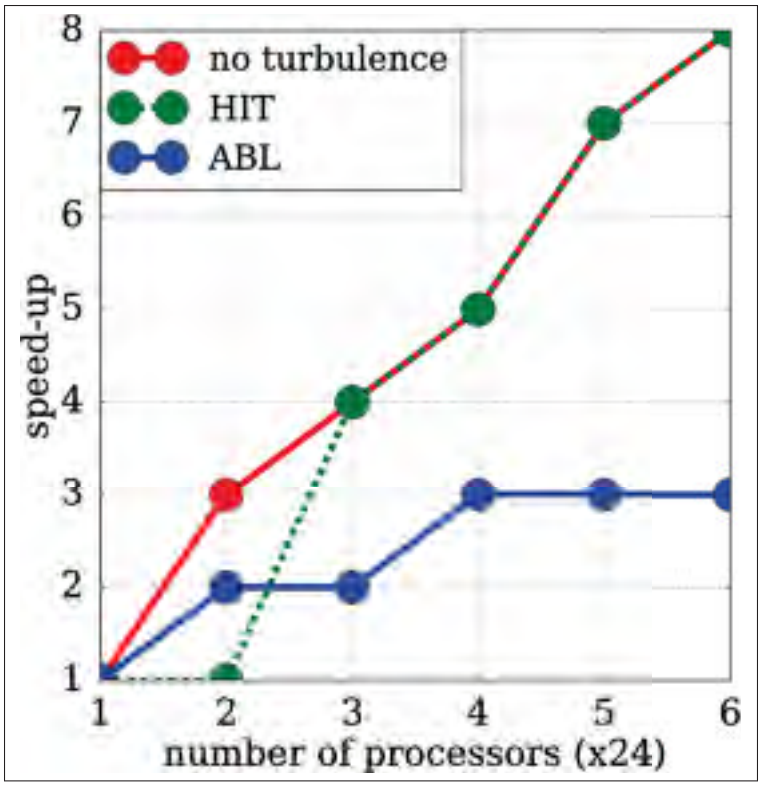

Figure 2.18 Speed-up over number of processors (multiples of 24) comparing the ALM immersed in a non-turbulent flow, homogeneous isotropic turbulence (HIT) and atmospheric boundary layer (ABL).

CHAPTER 3

(NEW) MEXICO EXPERIMENT

This chapter introduces the experimental results used for validating the numerical method in Chapter 4. First an overview of the setup of the MEXICO and NEW MEXICO experiment will be presented in Section 3.1 and its experimental results in Section 3.2.

The MEXICO experiment and its successor the NEW MEXICO experiment provide very useful data for the analysis of the near wake and the vortex properties of the shed vortices. When using the results obtained by the MEXICO experiment its shortcomings should be kept in mind such as e.g. the reflection of the nacelle and therefore a distortion of the values towards the hub. But also the overestimation of the velocity deficit especially in the case of $U_\infty = 15\,m/s$ which results also in a stronger wake expansion. This stems most probably from the fact that the wind tunnel experiments were conducted at lower velocities than the reference velocities.

Besides the rich findings of these two experiment, a lot of the numerical work has been done on the MEXICO experiment as summarized in Carrión *et al.* (2015). This permits also the validation against other numerical solutions.

3.1 Setup

The MEXICO (Model Rotor Experiments In Controlled Conditions) and NEW MEXICO experiments were conducted in an open-jet tunnel of the Large Low-speed Facility of DNW (German-Dutch Wind tunnels) in Netherlands. The square section of the open section was 9.5x9.5m^2 and a three-bladed rotor with a diameter of 4.5m was immersed in the flow.

3.1.1 (NEW) MEXICO rotor

The turbines used in both experiments are almost identical apart from the fact that the first one got destroyed during a transport and hence it had to be reconstructed for the NEW MEXICO

experiment based on the same rotor configuration used for the MEXICO experiment (Schepers & Boorsma, 2014).

It is a three bladed rotor and the numerically relevant properties for this work are listed in Table (3.1). For a more detailed description (Schepers *et al.*, 2012) is recommended. Each blade

Rotor diameter	$[m]$	4.5
Blade length	$[m]$	2.04
Hub height	$[m]$	5.49
Rotation direction	$[-]$	Clockwise (looking from upwind direction)
Rotor speed	$[rpm]$	324.5 - 424.5

Table 3.1 Technical details for (NEW) MEXICO rotor

consists of three airfoil sections, namely DU91-W2-250 in the root, RISØ A1-21 in the mid and NACA64-418 in the tip section with transition zones as depicted in Figure (3.1) between the sections and towards the tip and the hub. The exact data used for the blade definition given in Schepers *et al.* (2012) is listed in Table (A-1) and the cross sections of each airfoil segment are visualized in Figure (3.2).

As suggested also by Snel (1998) the airfoils in the root region are thicker and thinner towards the tip which is respected when looking at the different cross sections. Unfortunately when looking at the airfoil coefficients in Figure (2.6b) and especially the resulting force distribution on the blade in Figure (2.7a) it can be seen that the combination of these airfoils has its aerodynamical problems due to the abrupt changes in circulation at the edges of the mid-section of the blade. The choice of these airfoils was rather due to the fact that the three principal participating groups came from the Netherlands, Denmark and the USA and each wanted to contribute an airfoil.

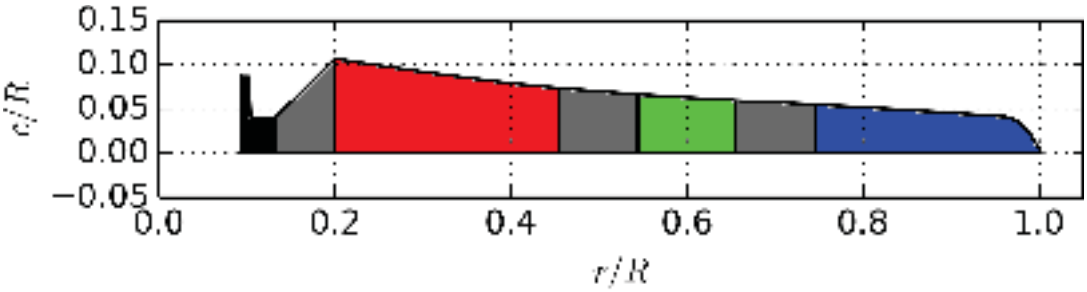

a) Variation of chord over radius

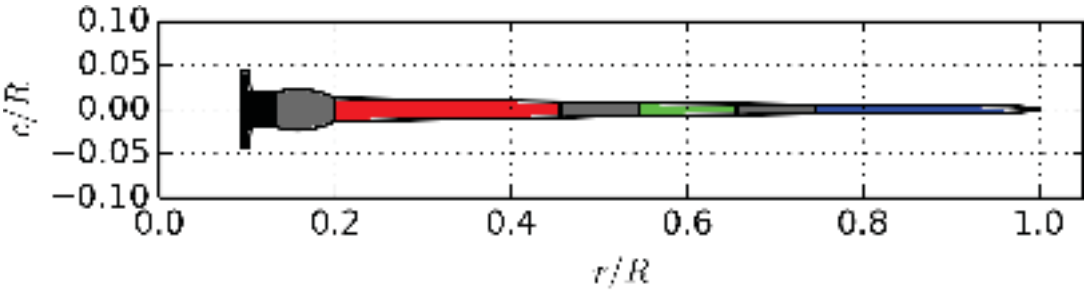

b) Variation of thickness over radius

Figure 3.1 Geometrical definition of the blade used in the MEXICO experiment with its airfoils DU91-W2-250 (red), RISØ A1-21 (green) and NACA64-418 (blue).

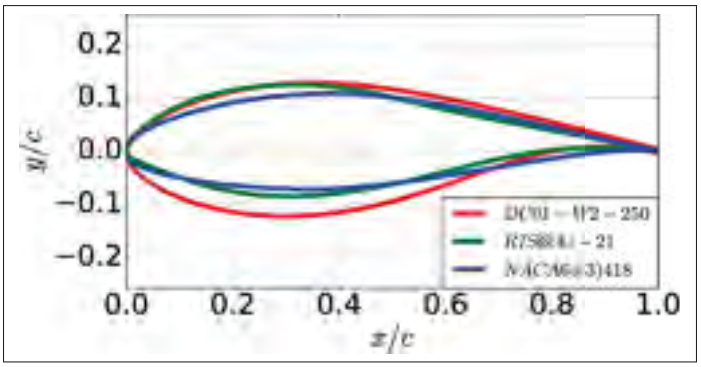

Figure 3.2 Cross sections of different airfoil segments used for MEXICO blade.

3.1.2 Wind tunnel

The experiment was conducted in the German Dutch Wind Tunnel Facilities (DNW) which is a closed-circuit, atmospheric, low-speed wind tunnel with an open jet. The test section for the (NEW) MEXICO experiments is $9.5\,\mathrm{m} \times 9.5\,\mathrm{m}$ or $4.22R$ x $4.22R$ with the rotor radius R.

The turbulence intensity TI was measured in an $8\,\mathrm{m} \times 6\,\mathrm{m}$ test section of the wind tunnel, hence the values have to be taken with care (Schepers *et al.*, 2012). DNW is suggesting the following formulas to correct the measured values for the actual tunnel geometry

$$TI_{x,9.5x9.5} = (CR_{8x6}/CR_{9.5x9.5})^2 \cdot TI_{long,8x6} \tag{3.1}$$

$$TI_{y,z,9.5x9.5} = (CR_{8x6}/CR_{9.5x9.5})^{0.5} \cdot TI_{lat,8x6} \tag{3.2}$$

for the longitudinal TI_x and lateral turbulence intensity $TI_{y,z}$ respectively whereas CR is the contraction ratio of the respective geometry. Another approach was using the stagnation point on the airfoil for high pitch angles for determining the turbulence intensity. With this approach it could not be differentiated between longitudinal and lateral turbulence intensity. Results are shown in Table (3.2) and when relying on the latter method some doubts are cast on the conversion formulas Eqn. (3.1) and Eqn. (3.2). Hence it is assumed that the turbulence intensity lies between $0.2\,\%$ and $0.4\,\%$ for the conducted wind tunnel experiments.

		measured ($8\,\mathrm{m} \times 6\,\mathrm{m}$)	corrected ($9.5\,\mathrm{m} \times 9.5\,\mathrm{m}$)	standstill measurements
TI_{long}	$[\%]$	0.22	0.77	–
TI_{lat}	$[\%]$	0.11	0.16	–
TI	$[\%]$	–	–	$0.2 - 0.4$

Table 3.2 Different possible turbulence intensities for NEW MEXICO.

Normally the tunnel blockage effects can be calculated from relating the rotor swept surface to the cross section surface of the wind tunnel. In this case it is not as straight forward as the

wind tunnel operates with an open jet and hence the free shear layer flow behaves differently than a wind flow confined by solid surfaces.

Several analytical and numerical approaches have already been considered for evaluating the resulting blockage effect in the MEXICO project (Schepers *et al.*, 2012). It was found that the blockage effect is very limited, especially in the near wake. Also a higher influence of the tunnel was found for higher thrust coefficients C_T and hence a more pronounced wake expansion.

3.1.3 Measurement campaign

While several experiments were conducted using the setup described above, only the PIV measurements and force measurements were used in this work. The testing parameter are summarized in Table (3.3). The PIV measurements were acquired by placing the PIV windows

		MEXICO	NEW MEXICO
Blade config	$[-]$	zig-zag tape	Clean outboard blade ($r/R > 0.7$)
Pitch angle	$[^\circ]$	-2.3	-2.3
Yaw angle	$[^\circ]$	0	$-30, 0, 30$
Rot. speed	$[rpm]$	424.5	425.1
U_∞	$[m/s]$	$10, 15, 24$	$10, 15, 24$

Table 3.3 Testing parameters for used runs from (NEW) MEXICO.

in the 9 o'clock plane looking at the rotor from an upwind position as shown in Figure (3.3), Figure (3.4) and Figure (3.5).

In Figure (3.3) the locations of the PIV windows for the vicinity of the rotor for each velocity used in MEXICO experiments are shown. Each window is represented by semi-transparent grey rectangle, while a certain overlap occurs indicated by the areas in darker grey. The intention was to well capture the tip region before and after the vortex shedding. Therefore the snapshots were taken at different rotor position angles Ψ.

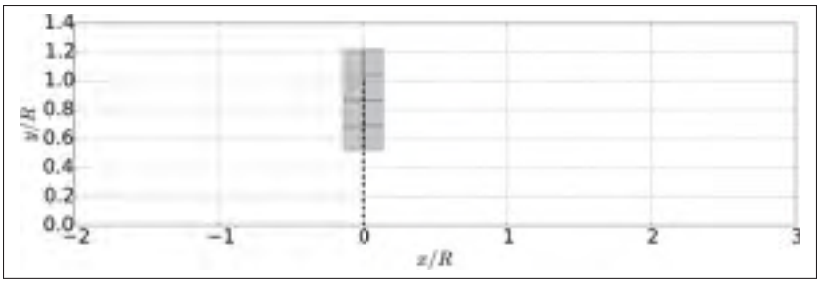

Figure 3.3 Locations of PIV windows for the vicinity of the rotor for each velocity used in MEXICO experiments for each case.

In Figure (3.4) the locations of the PIV windows for capturing the axial flow for each velocity used in MEXICO experiments are shown. All snapshots were taken at $\Psi = 0\ ^\circ$. Some PIV runs were made twice indicated by a darker gray window.

In Figure (3.5) the locations of the PIV windows for following the trajectory of the shed vortices for each velocity used in MEXICO experiments are shown. The windows were positioned in accordance to the observed vortex trajectories. All snapshots were taken at $\Psi = 30\ ^\circ$ or the moment when the blade crosses the PIV plane.

3.2 Results

3.2.1 Blade and rotor forces

By the aid of several pressure sensors distributed along the blade the forces could be evaluated and are shown in Figure (3.6). It can be seen that due to the similar setup results fall in the same range with a slightly higher normal force F_n towards the tip for the NEW MEXICO experiment. It can also be seen that the tangential force, hence the circulation remain almost constant over the whole span.

For the NEW MEXICO experiment also the standard deviation is given. The error for the forces along the blade are less than 1% for the normal forces F_n but up-to 300% (on average

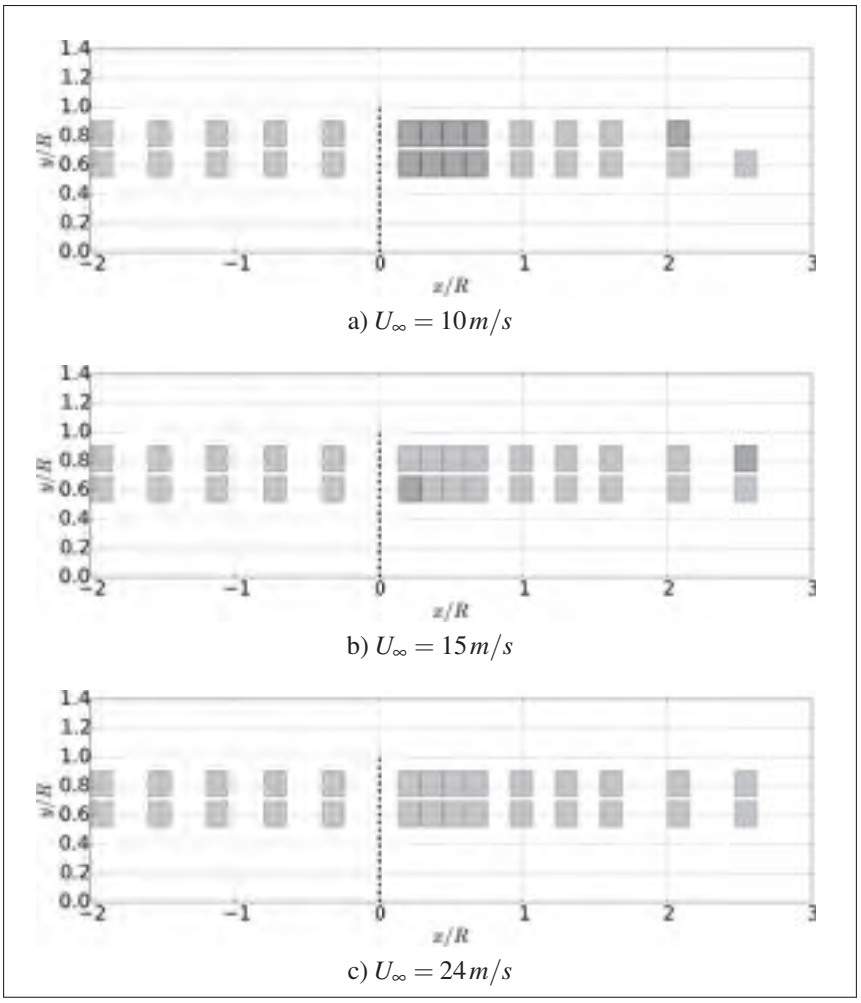

a) $U_\infty = 10 m/s$

b) $U_\infty = 15 m/s$

c) $U_\infty = 24 m/s$

Figure 3.4 Locations of PIV windows for capturing the axial flow for each velocity used in MEXICO experiments.

around 100%) for the tangential forces F_t as they are relatively small. As the absolute errors are very small for the force measurements, error bars are omitted in Figure (3.6).

In Table (3.4) the rotor torque and thrust are listed whereas the standard deviation is again given for NEW MEXICO. It can be seen that while the torque values seem to remain within the same range, the thrust values are significantly smaller for NEW MEXICO.

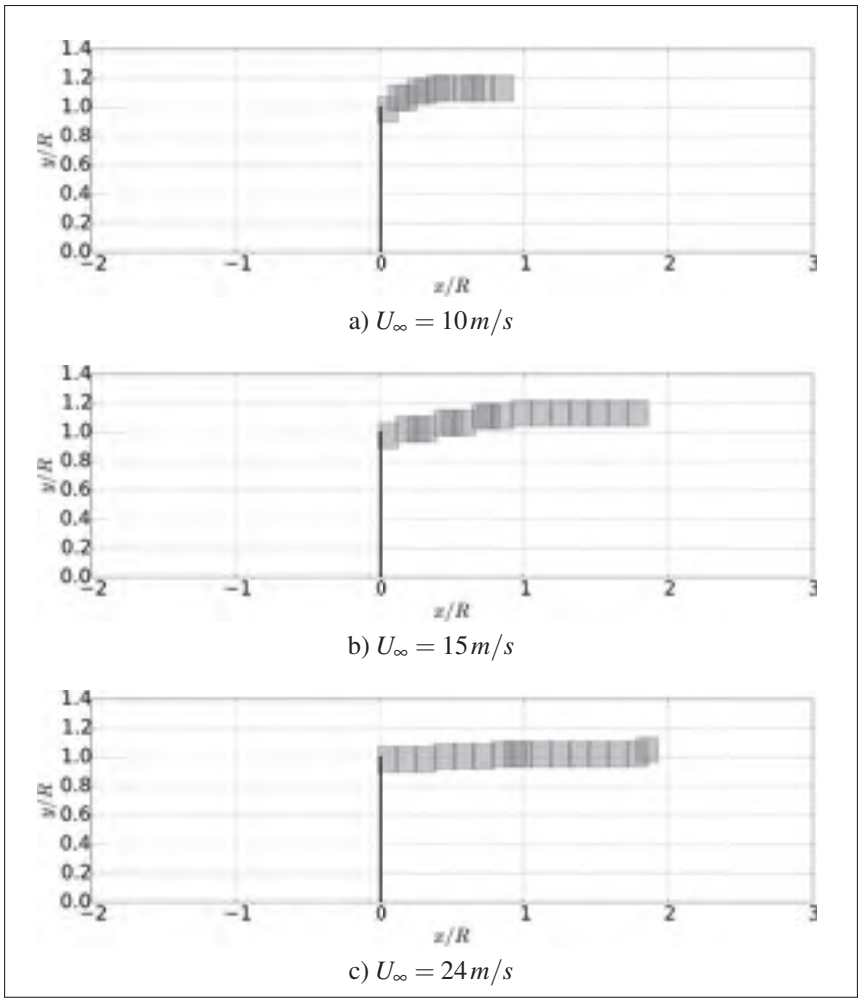

Figure 3.5 Locations of PIV windows for following the trajectory of the shed vortices for each velocity used in MEXICO experiments.

	$U_\infty [m/s]$	10	15	24
MEXICO	Torque $[Nm]$	60	290	690
	Thrust $[N]$	1,000	1,950	3,200
NEW MEXICO	Torque $[Nm]$	68±2.4	316±2.5	715±2.0
	Thrust $[N]$	974±9.2	1,663±15.0	2,172±10.9

Table 3.4 Rotor torque and thrust for the three different cases.

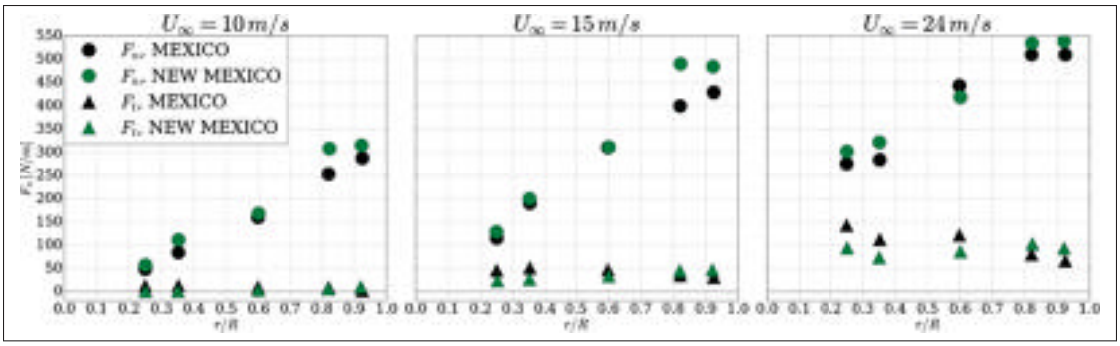

Figure 3.6 Normal and tangential forces along the blade for MEXICO and NEW MEXICO experiment.

3.2.2 PIV images

In order to analyze the shedding of the tip vortex, the vicinity of the rotor as shown in Figure (3.3) was captured and its results are shown in Figure (3.7). Phase-averaging references to the the angular position of the rotor Ψ for which separate time averages are taken. Several things can be observed when looking at the data, such as e.g. the circulation of the incoming blade in Figure (3.7h) and Figure (3.7n) visualized by the red line which is stronger towards the hub as the blade is closer to the PIV plane.

Another interesting aspect is also that for high velocities such as $U_\infty = 24\,m/s$ not only the tip vortex becomes appearant but also due to greater absolute differences in circulation along the blade more distinct vortices are shed from the trailing edge as seen shortly after the blade passes through the PIV plane in Figure (3.7o). In Figure (3.7c) the changes the circulation undergoes seem to be much smaller, hence a vortex sheet is shed instead. Of course this also due to the resolution of the PIV image.

Something more curious seem to happen downstream towards the hub particularly pronounced for $U_\infty = 15\,m/s$ e.g. in Figure (3.7i). An abrupt change in the velocity deficit bearing no resemblance to the other cases. This is due to the reflection of the nacelle distorting the PIV images towards the hub, hence results of the MEXICO experiment should be taken with caution in this range (Schepers *et al.*, 2012).

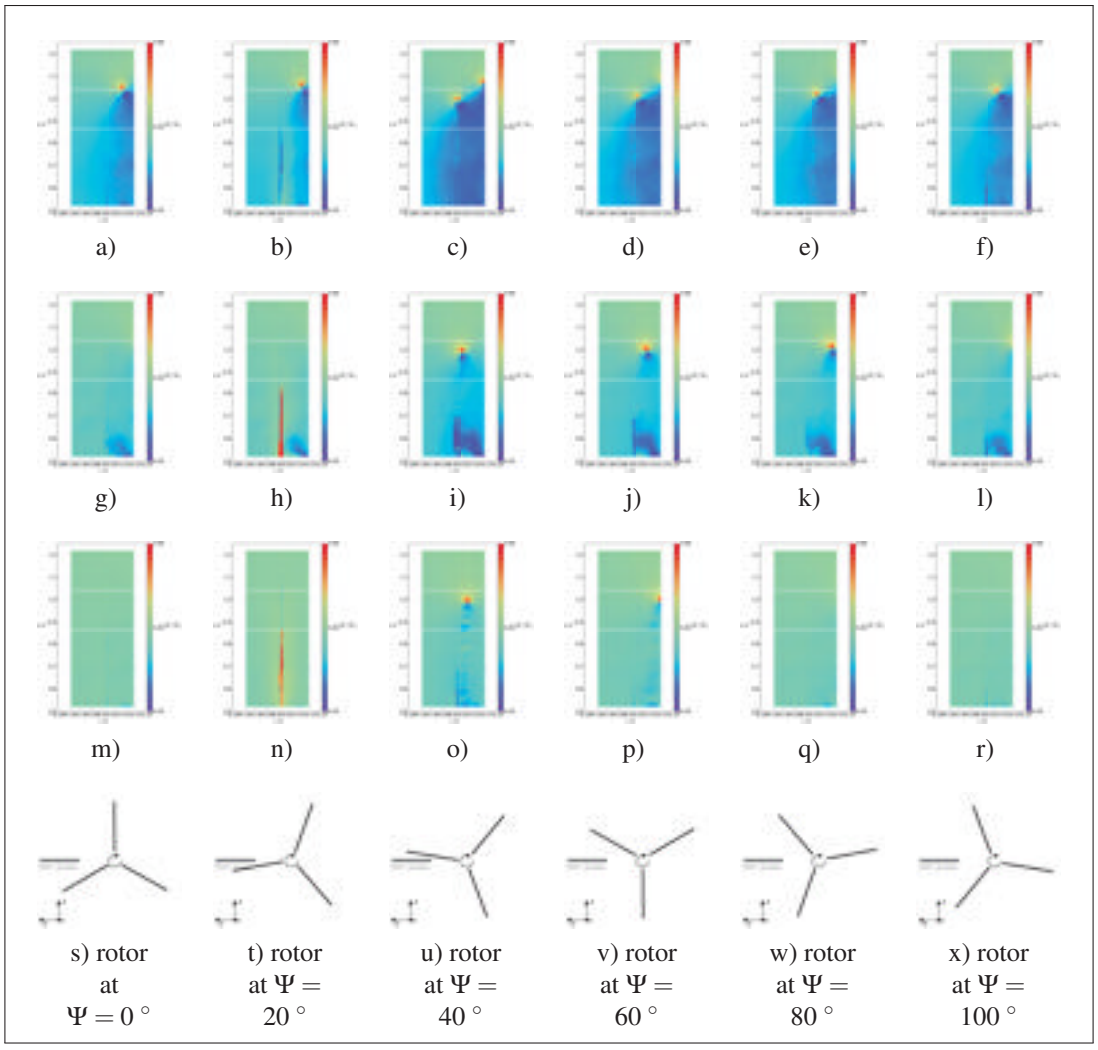

Figure 3.7 Phase-averaged velocity magnitudes $|\mathbf{U}|/U_\infty$ for $U_\infty = 10\,m/s$ (first-row), $U_\infty = 15\,m/s$ (second-row), $U_\infty = 24\,m/s$ (third-row) for different rotor positions Ψ (last-row).

The PIV images for capturing the bigger picture of the flow are visualized in Figure (3.8). In Figure (3.8a) due to high thrust and the deflection of part of the flow around the rotor, a turbulent wake state can be observed. For the high velocity case in Figure (3.8c) the momentum deficit behind the rotors remains rather small. Again reflection of the nacelles causes a distortion of the PIV images towards the hub which can be noticed for all three cases but is again particularly pronounced for the case of $U_\infty = 15\,m/s$ as shown in Figure (3.8b).

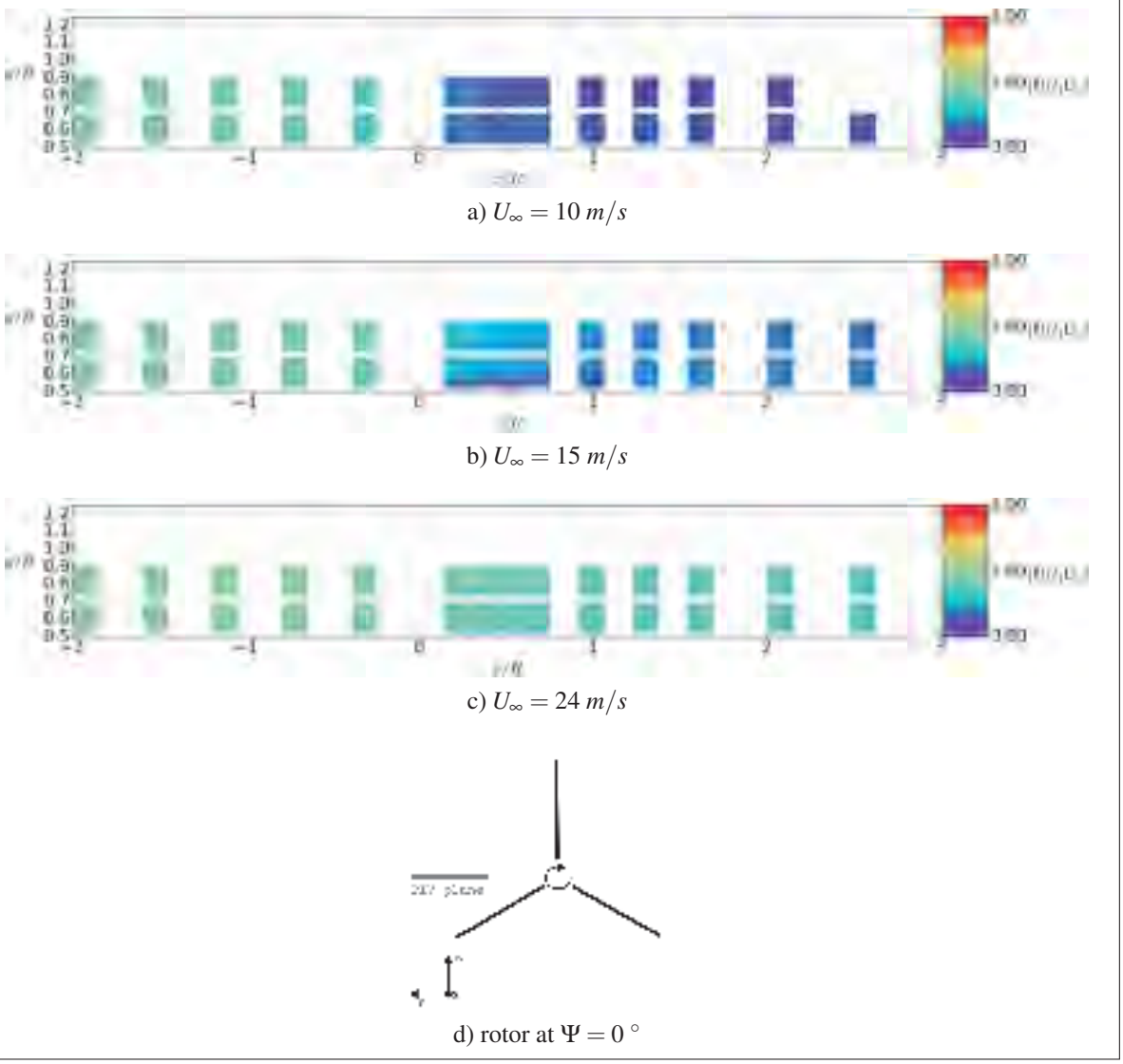

a) $U_\infty = 10\ m/s$

b) $U_\infty = 15\ m/s$

c) $U_\infty = 24\ m/s$

d) rotor at $\Psi = 0\ ^\circ$

Figure 3.8 Phase-averaged velocity magnitudes for the rotor position $\Psi = 0\ ^\circ$ for different velocities U_∞.

The PIV images for the vortex trajectories are visualized in Figure (3.9) and as the rotor passes through the PIV plane, the first tip vortex is not yet completely formed. Therefore for later comparison the second fully formed vortex will always be used. Due to the restriction in placing the PIV windows, some vortices are close to the edges of the windows especially in Figure (3.9a) and Figure (3.9b). This should be kept in mind when evaluating the circulation of the vortices, as the ones further downstream are not fully captured.

By looking at the different trajectories also the different kind of wake expansions can be seen, from the wide expansion of a turbulent wake state in Figure (3.9a) to only a very slight extension in the high velocity case in Figure (3.9c).

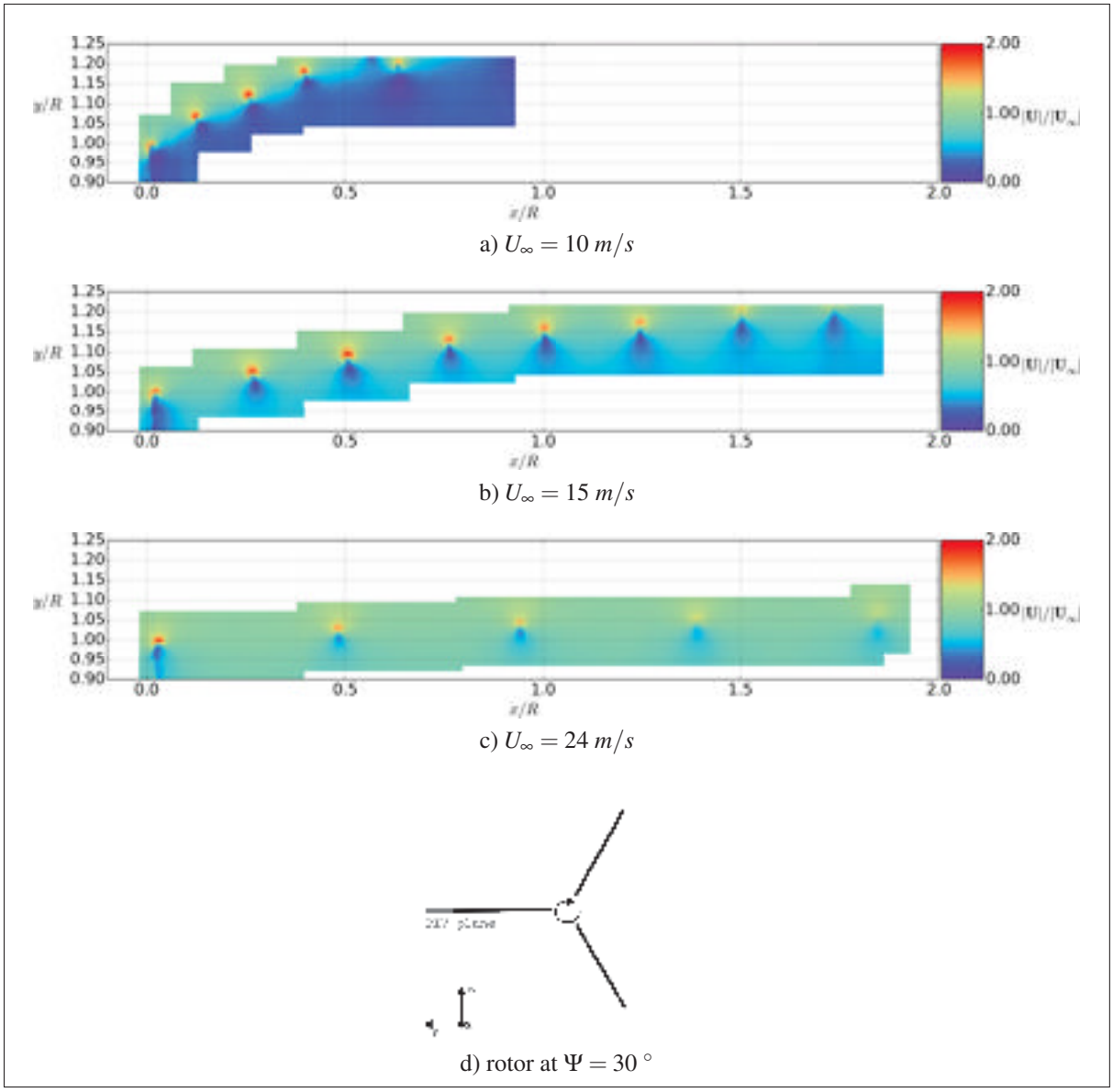

a) $U_\infty = 10\ m/s$

b) $U_\infty = 15\ m/s$

c) $U_\infty = 24\ m/s$

d) rotor at $\Psi = 30\ ^\circ$

Figure 3.9 Phase-averaged velocity magnitudes for the rotor position $\Psi = 30\ ^\circ$ for different velocities U_∞.

As the ÉTS Montréal was one of the participating universities in the MEXICO experiment (Schepers *et al.*, 2012), extensive data sets were available and the PIV images are used in this work to extract radial and axial velocity profiles. As this was not the case for the NEW MEXICO experiment, this access was restricted. But fortunately the organizers made a subset of the experimental data publicly available upon request. So instead of relying on PIV images for data extraction, some profiles at specific points are given. In Figure (3.10) the radial profiles are shown. Here the phase-averaged velocities for

$$\Psi = [10, 17, 22, 26, 29, 31, 34, 38, 43, 50, 70, 90, 110]\ ^\circ$$

were averaged again to obtain a time average. The density of measurement points around the moment of blade passage ($\Psi = 30\ ^\circ$) is higher as the significantly higher velocity deficit should have been included properly (Schepers & Boorsma, 2014).The axial positions of the radial profiles are very close to the rotor ($x/R = \pm 0.13$) and hence the induction of the blade has a very distinct appearance.

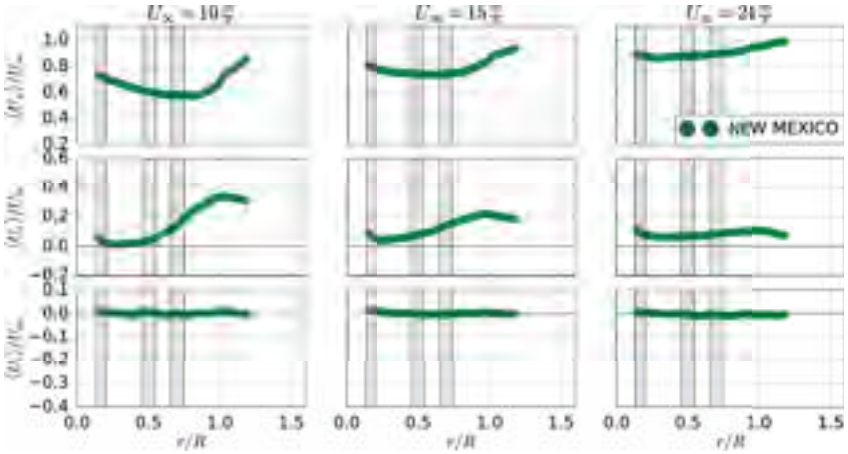

a) $x/R = -0.13R$

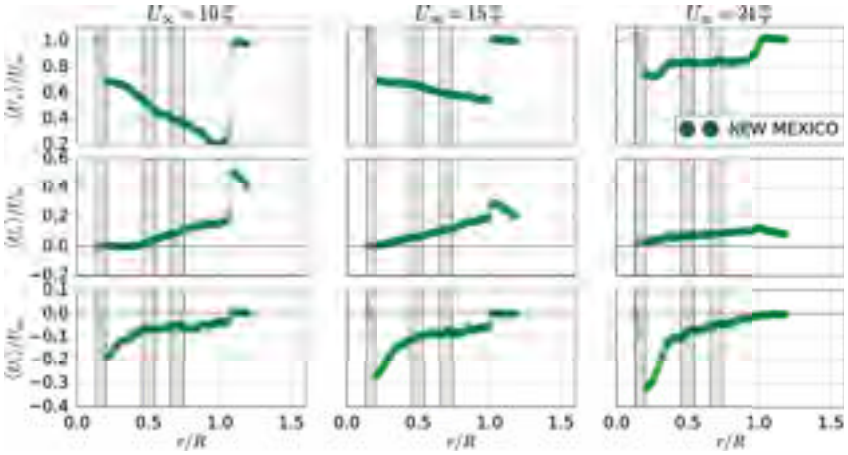

b) $x/R = 0.13$

Figure 3.10 Radial profiles of normalized time-averaged velocity components for the three cases slightly up- and downstream of the rotor for NEW MEXICO. The grey areas represent the transition between different airfoil segments of the blade.

The axial profile for different radial positions can be seen in Figure (3.11) together with sampled data from the MEXICO experiment. While for the outboard position the data for all three velocities is available, the data for the inboard position exists only for $U_\infty = 15\,m/s$. When comparing MEXICO and NEW MEXICO it can be seen that the velocity deficit is less pronounced for the NEW MEXICO experiment. This confirms what was observed by the global thrust values in Table (3.4).

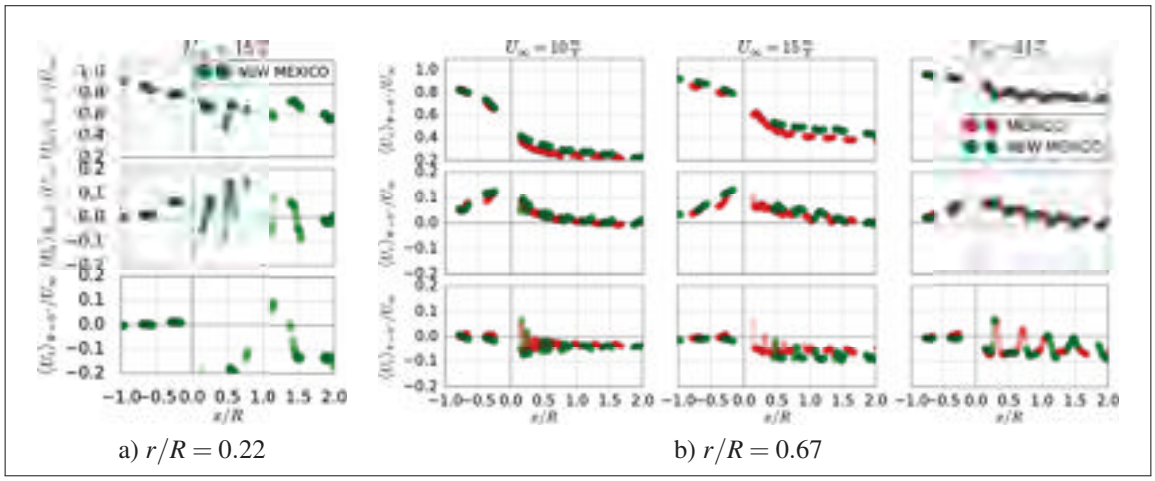

a) $r/R = 0.22$ b) $r/R = 0.67$

Figure 3.11 Axial profiles of normalized velocity components phase-averaged for azimuthal angles of $\Psi = 0\,^\circ$ for the case with $U_\infty = 15\,m/s$ at an in- and an out-board position of the blade for NEW MEXICO.

In order to evaluate the induction of the blade passage on the flow different azimuthal positions at different radial locations at up- and downstream of the rotor were taken and visualized in Figure (3.12) and Figure (3.13). As with the radial profiles in Figure (3.10) the induction upstream is much less pronounced than downstream due to the presence of the tip vortices. All three cases exhibit a continuous decrease in the axial velocity component around the passage point ($\Psi = 30\,^\circ$) and a bump in the tangential velocity component.

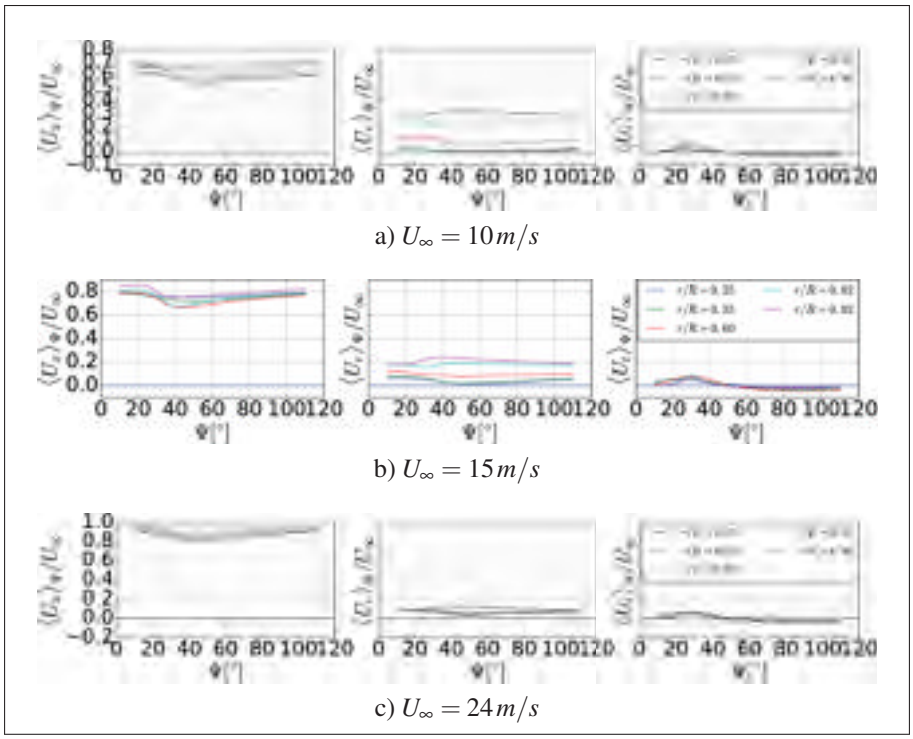

a) $U_\infty = 10\,m/s$

b) $U_\infty = 15\,m/s$

c) $U_\infty = 24\,m/s$

Figure 3.12 Azimuthal profiles of normalized phase averaged velocity components for the three cases at an upstream position $x/R = -0.13$ of the rotor for NEW MEXICO.

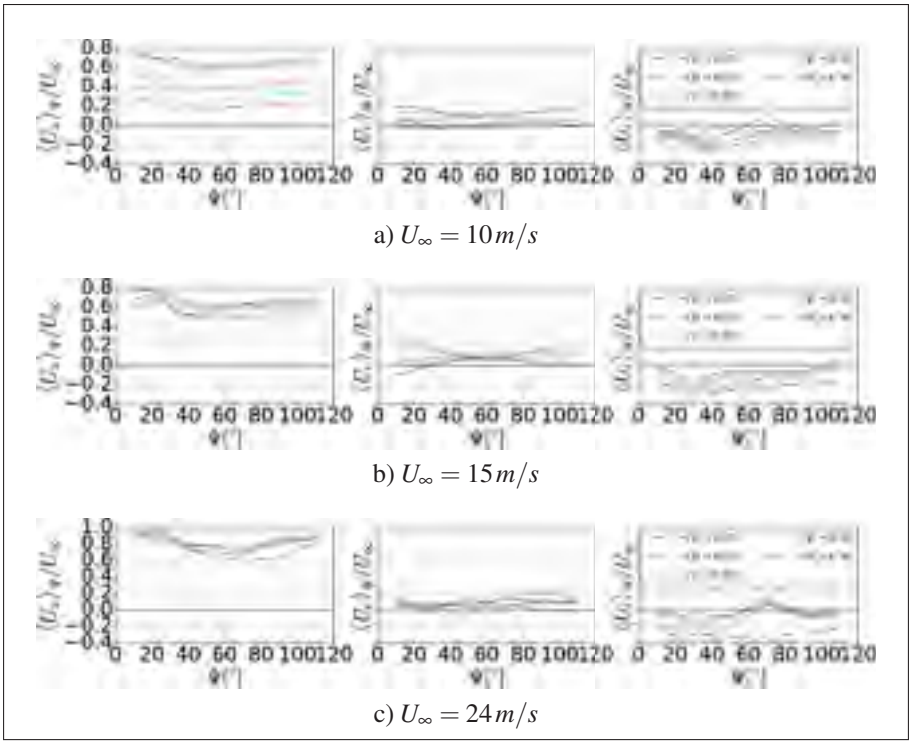

a) $U_\infty = 10m/s$

b) $U_\infty = 15m/s$

c) $U_\infty = 24m/s$

Figure 3.13 Azimuthal traverses of normalized phase averaged velocity components for the three cases at an downstream position $x/R = 0.13$ of the rotor for NEW MEXICO.

CHAPTER 4

CASE 1: NON-TURBULENT UNIFORM FLOW AT THE INLET

The immersion of the rotor model in a non-turbulent flow allows the validation and verification[1] of the implementation without the added layer of complexity of turbulent inflow. In Section 4.1 the adapted SOWFA framework is validated against EllipSys3D, another very popular framework for wind energy research. Then both frameworks are verified against experimental data by comparing them against the MEXICO experiment. In Section 4.2 the final numerical setup of the test case is derived and in Section 4.3 near wake results are presented followed by a concluding remark in Section 4.4.

4.1 Verification and validation

As the implementation details of this work are already laid out in Chapter 2, only EllipSys3D will be described briefly in order to highlight similarities and differences of these two frameworks.

EllipSys3D (Sørensen, 1995) is based on the control volume method with variables located at cell center and a Rhie-Chow (Rhie & Chow, 1983) like correction (Rethore & Sørensen, 2008).

The rotor is also modeled as a force, inserted as a momentum sink in the Navier-Stokes equations and distributed by a Gaussian distribution in order to avoid non-physical spikes in the velocity field around the affected cells. While SOWFA specifies a cut-off length for the 3D Gaussian curve in order to recover approximately 99.9% when integrated, the cut-off length of EllipSys3D is significantly larger to contain an even higher percentage. These two different cut-off lengths do not seem to have a significant impact on the simulation results (Nathan *et al.*, 2017).

[1] The results of this study were published as a conference article (Nathan *et al.*, 2017).

Another difference is the way how velocities are sampled in order to calculate the blade forces based on airfoil coefficient tables. EllipSys3D obtains the velocity value by a trilinear interpolation between the cell containing the actuator point and its adjacent cells (Sørensen, 1995).

While there are efforts to modify the original 2D airfoil coefficient data as e.g by Shen *et al.* (2012), the present work wants to examine how well the actuator line method can predict experimental results by relying on the original airfoil data obtained from wind tunnel experiments of an infinite wing.

A tip correction is applied on the calculated forces. Without the tip correction, the forces where much higher than predicted by experiment and there was a sudden drop in the force in the last actuator point before the tip. In order to have a smoother decline of the force it was concluded to apply the Glauert tip correction as shown in Figure (4.1). This resulted also in a better agreement with the experimental data.

While the Glauert tip correction was originally intended (Glauert, 1935) for including the presence of tip vortices for the actuator disk model, it still proves advantageous for the ALM at lower resolutions. Due to the relatively low resolution the shed tip vortices from an ALM are much larger than the ones observed experimentally. Hence the induction by the simulated vortices is weaker than in reality and the Glauert tip correction compensates in part for this lack (Nathan *et al.*, 2017).

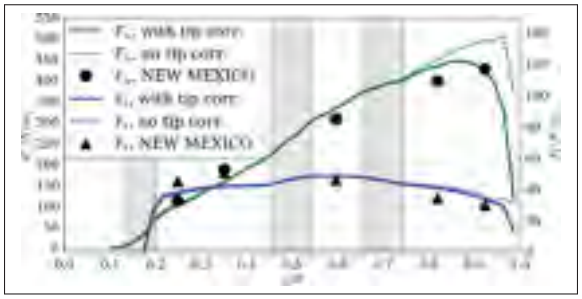

Figure 4.1 Difference of force evaluation with and without applied tip correction.

4.1.1 Base case setup

The computational domain is cubic as shown in Figure (4.2) with an edge length of

$$L_x = L_y = L_z = 20R$$

with R as the radius and the rotor positioned at the domain center. In both cases the cells in a refined zone around the rotor with edge lengths $x_{11} - x_{00} = w = 4R$ are cubic with the size $\Delta x = D/64$ and are stretched towards the domain boundaries in the case of EllipSys3D. Within SOWFA several refinement zones are applied each time halving the cell edge length as also done in Vanella *et al.* (2008). Therefore the mesh of EllipSys3D consists of $7.1 \cdot 10^6$ cells while the mesh of the SOWFA case consists of $1.9 \cdot 10^6$ cells. The technique used in SOWFA proves highly advantageous in terms of computational cost and its impact on the results will be examined in a sensitivity study in Section 4.2.

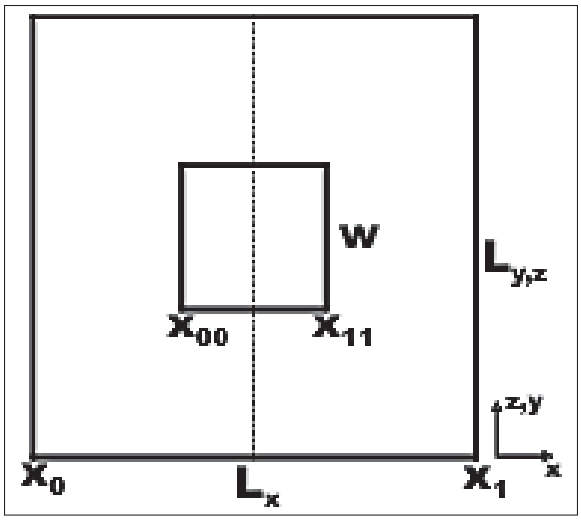

Figure 4.2 Mesh dimensions with rotor positioned at center indicated by grey dashed line at $x = 0$.

For the boundary conditions for the velocity both cases have an uniform inflow velocity of $\mathbf{U} = (U_\infty, 0, 0)$ resulting in an irrotational flow at the inlet and a zero gradient at the outlet. The lateral boundaries are set as symmetric boundary conditions.

Both simulations are large eddy simulations, the sub-grid scale models are the dynamic Lagrangian method based on Meneveau *et al.* (1996) for the SOWFA case and a DES model using a limiter to switch between $k-\omega*$ SST and LES Troldborg *et al.* (2015) for the EllipSys3D case. But as there is no inflow turbulence and the helicoidal vortex structure does not break up within the examined region, not a lot of turbulence modeling has to be done for the base case. When comparing to a very coarse DNS by deactivating the sub-grid scale model, no significant difference is found as mentioned in Nathan *et al.* (2017).

EllipSys3D applies QUICK (Leonard, 1979) in RANS regions and central differencing of fourth order in LES regions using the same limiter as for DES model.

For parametrization of the ALM the Gaussian distribution parameter is set at $\varepsilon = 2\Delta x$ and 40 actuator points are used to represent one blade in accordance with what was found in Chapter 2.

4.1.2 Results

The first interesting observation is the similarity in sampled velocities and AOAs as shown in Figure (4.3). Despite the more simplistic approach of SOWFA both frameworks seem to obtain almost the same values although steep velocity gradients exist in the sampling area due to the bound vorticity of the blades due to the inserted forces. This even holds for the relative small value of the tangential velocity component.

These results are encouraging as how to sample correctly the velocity for the ALM is still part of an on-going debate (Shen *et al.*, 2009a), but as shown here and subsequently even sampling at the actuator point itself delivers good results.

When looking at the AOAs in Figure (4.3a) it can be seen that for the radial position $r/R < 0.3$ at $U_\infty = 24\,m/s$ it exceeds the angle after which stalling occurs according to the 2D airfoil

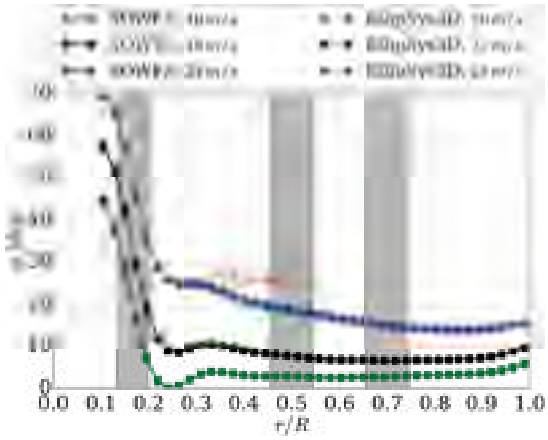

a) Angle of attack α for each actuator point along the blade. The grey zones represent transition between different airfoil types and the red line the AOA for which the inboard airfoil data indicates stalling. The rotor position is $Psi = 0°$.

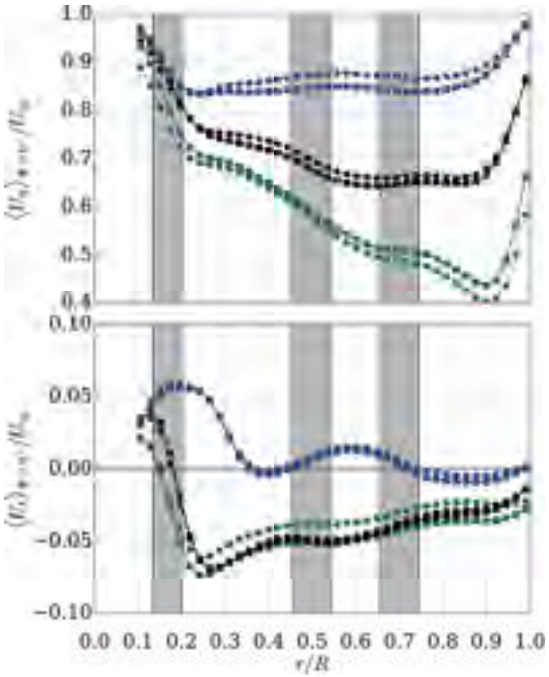

b) Normalized normal velocity and tangential velocity component $\langle U_n \rangle_{\Psi=0°}/U_\infty$ and $\langle U_t \rangle_{\Psi=0°}/U_\infty$ for each actuator point along the blade. The grey zones represent transition between different airfoil types. (see legend in Figure (4.3a)).

Figure 4.3 AOA and components of sampled velocity.

data. For the other cases and airfoil sections the AOA always remains below the critical angle. Hence the actuator line method with the unaltered airfoil data breaks for the aforementioned case and the calculated forces will not match the ones obtained experimentally in the inboard region with the DU airfoil (for reference see Figure (3.1a)). A possible circumvention could be the usage of the Beddoes-Leishman dynamic stall model (Leishman, 2002) as done in Pereira *et al.* (2013). Other approaches can also be found in Holierhoek *et al.* (2013).

In Figure (4.4) the body forces associated with rotating blades can be seen. For $U_\infty = 10\,m/s$ and $15\,m/s$ exists a very good agreement, while the forces are not correctly evaluated for the high velocity case. A sudden drop in both forces can be seen stemming from the fact that beyond the AOA no experimental data is available and in order to fill the region beyond that

the flat plate assumption (Viterna & Janetzke, 1982) is used leading to a sharp drop in the lift coefficient. Another interesting observation is that the forces for the MEXICO experiment are lower than for the NEW MEXICO experiment. This is probably due to the fact that the experiments were conducted with a slightly lower inlet velocity. Again the SOWFA and the EllipSys3D case are very similar even in the case where the models break down.

It should be noted that the agreement is very well and is similar to fully resolved rotor simulations which compared to NEW MEXICO such as conducted by Sørensen *et al.* (2016). When looking at fully resolved rotor simulations compared to MEXICO such as Bechmann *et al.* (2011), Sørensen *et al.* (2014) and Carrión *et al.* (2015) it is again confirmed that the MEXICO experiment was probably run with lower inlet velocities than indicated. Also earlier work on ALM and EllipSys3D found a similar agreement in Shen *et al.* (2012).

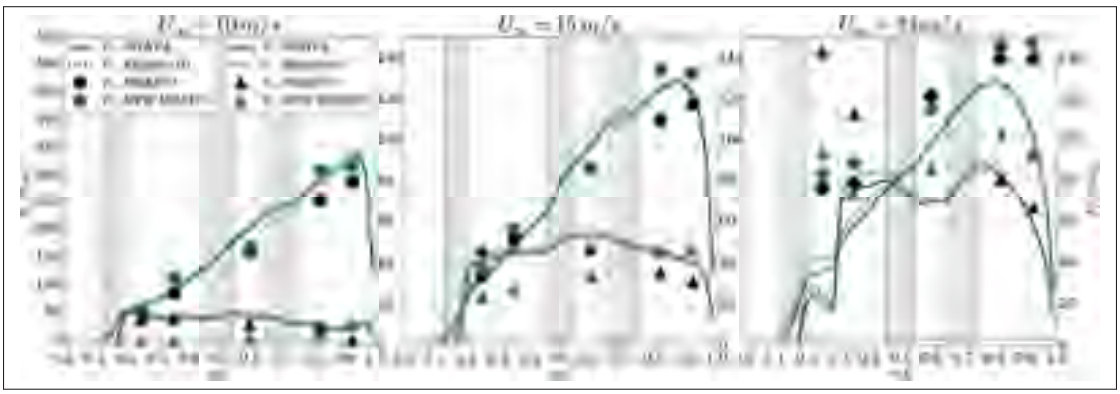

Figure 4.4 Comparison between the evaluated normal and tangential blade forces F_n and F_t by SOWFA and EllipSys3D (Nathan *et al.*, 2017) against the experimental results of MEXICO and NEW MEXICO over the radial position.

Due to the only slight discrepancies in force evaluation both frameworks produce a relatively similar flow field as shown in Figure (4.5). It can be seen that neither SOWFA nor EllipSys3D can simulate distinct vortices shedding in the case of turbulent wake state ($U_\infty = 10 m/s$), but instead a continuous vortex is shed from the rotor. This is due to the rather coarse resolution of $D/64$. In the cases with higher inlet velocities and a higher distance between the vortices a vortical structure can be noticed.

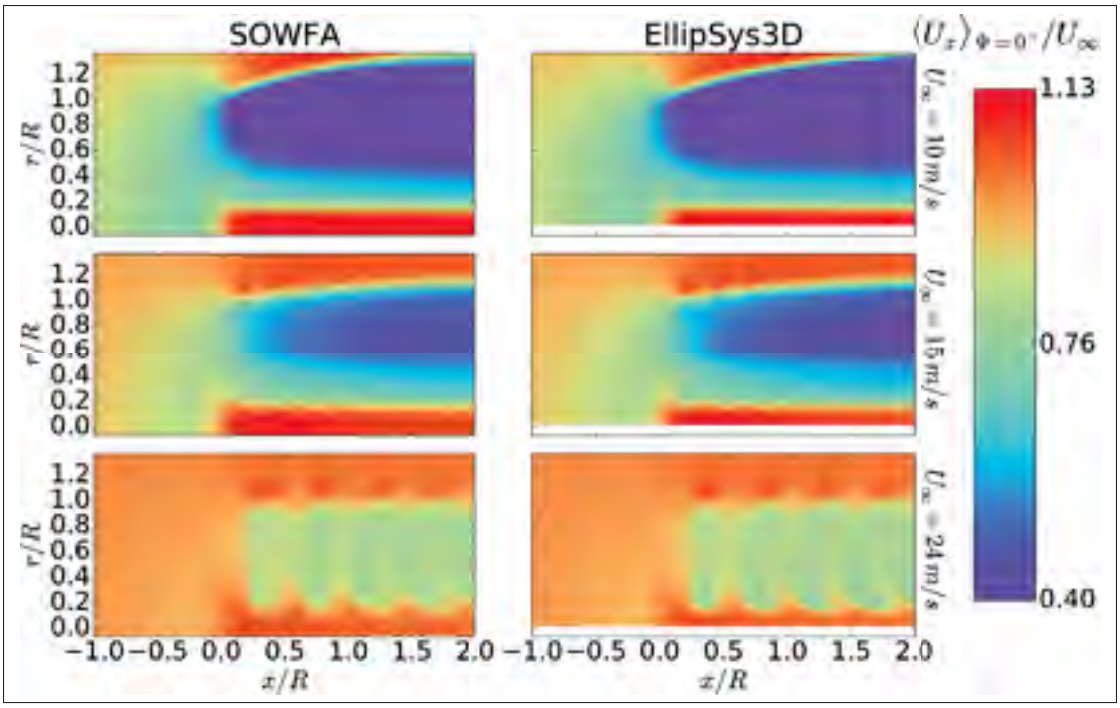

Figure 4.5 Planes of normalized axial velocity component U_x/U_∞ for all three cases for SOWFA and EllipSys3D. The rotor is situated at $x/R = 0$ and the velocity field is phase averaged for the rotor position $\Psi = 0^o$.

When looking at the radial profiles of the axial, normal and tangential velocity components U_x, U_r and U_t in Figure (4.6), it can be seen that in general both frameworks are underestimating the velocity deficit in the ultimate rotor vicinity ($x/R = \pm 0.13$) compared to the experimental results but the overall trend is very well maintained. An exception is the high velocity case ($U_\infty = 24\,m/s$) where the models deficit becomes appearant. It is remarkable that the solution for the ALM is even very close in the prediction of the radial flow $\langle U_r \rangle$ in the tip region $r/R \approx 1$ at the downstream position in Figure (4.6b) which bears close resemblance to the results found by fully resolved rotor simulations e.g. in Sørensen *et al.* (2014).

The high gradient of the radial velocity component in the tip region seems to be smeared out by the numerical simulation as can be seen in Figure (4.6b). This is stems from too far spread tip vortices due to coarse meshing. The same applies as well for the tangential velocity component in the root region.

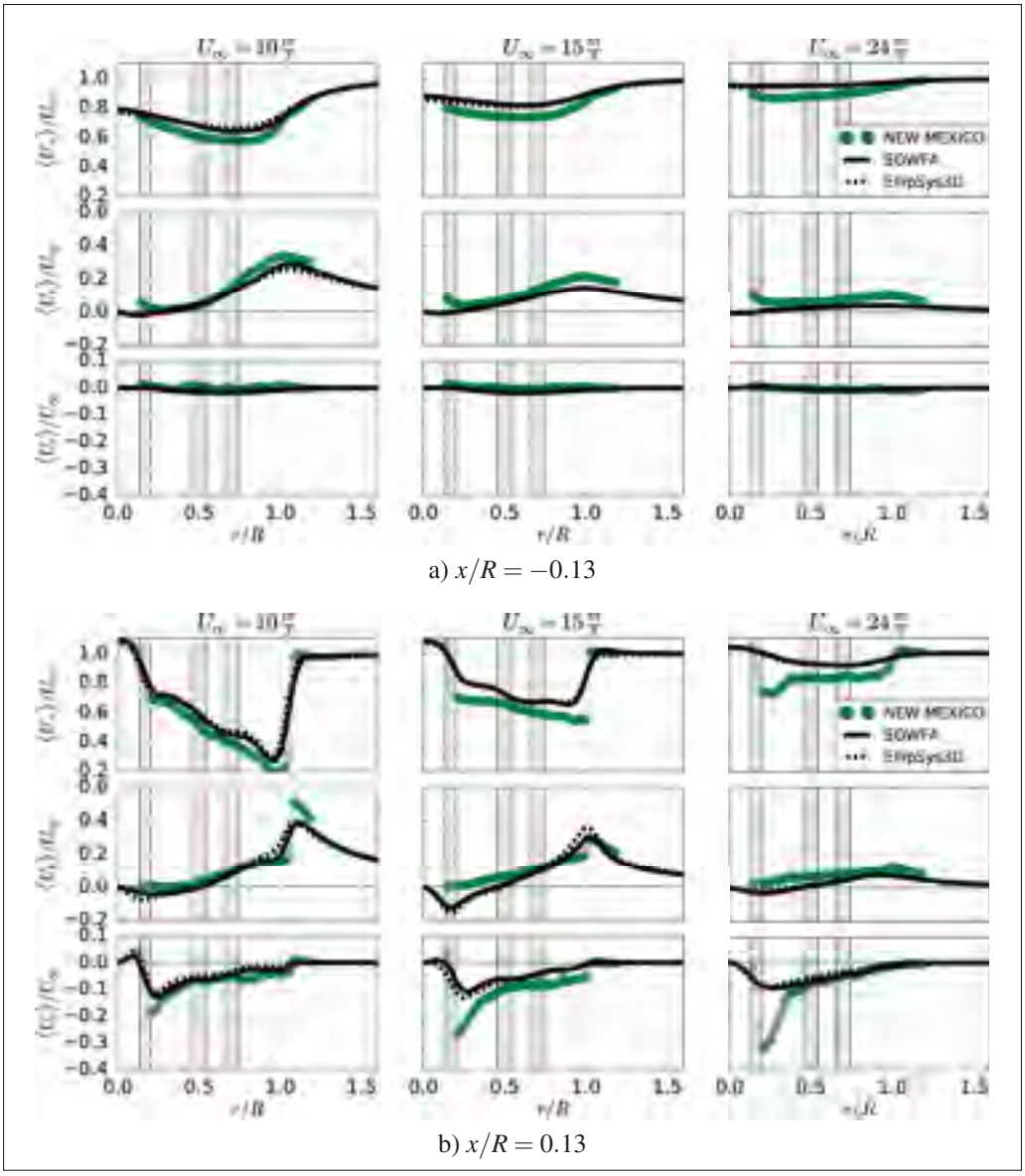

a) $x/R = -0.13$

b) $x/R = 0.13$

Figure 4.6 Radial profiles of time-averaged velocity components for different flow cases up- and downstream of rotor.

The axial profiles of the velocity components can be seen Figure (4.7) and again both codes reproduce very similar results in the near wake further away from the rotor. While for the inboard position only data from NEW MEXICO experiments for $U_\infty = 15\,m/s$ are available, we can look at a bigger picture for the outboard position shown in Figure (4.7b). Again simulation results are very close to experimental data from the NEW MEXICO experiment, while overestimating with respect to MEXICO results due to reasons already mentioned as also seen in

Shen *et al.* (2012). For the high velocity case ($U_\infty = 24\,m/s$) the vortex sheets shed from the blades become visible by the oscillations in the axial velocity component U_x.

When looking at the vortex properties as examined in Nilsson *et al.* (2015) in Figure (4.8) it can be seen that there is a good general agreement despite the coarse resolution of the grid around the rotor ($\Delta x = D/64$). In Figure (4.8a) the vortex locations were obtained based on a rotor position of $\Psi = 0^o$ while the experimental data was taken for $\Psi = 30^o$, which is the moment when the blade crosses the PIV sheet. This is was done for sake of convenience in order to easily compare the two numerical frameworks, and it is also justified as vortices follow same trajectory independent of rotor position Ψ. The center of a vortex was defined as the local maximum of the vorticity magnitude. Keeping in mind that the origins might not coincide as stated in Nilsson *et al.* (2015) and as mentioned above the wake deficit was lower in the experiments for $U_\infty = 15\,m/s$, the simulations appears to represent well the vortex propagation. This can also be seen by looking at Figure (4.8b) and comparing the axial locations of the vortices compared to the experimental results. Differences between the two simulations as seen in Figure (4.8a) and Figure (4.8b) stem from discrete representation of the vortices. In a more refined mesh both curves are expected to be closer.

When looking at the evolution of the vortices in terms of strength it can be seen in Figure (4.8c) that the circulation remains almost constant throughout the examined region, despite the fact that a constant integration radius R_S was used in order to evaluate the total circulation Γ. There is a sharp drop in circulation strength for the last two vortices in downstream direction. As already discussed in Section 3.2 these vortices are close to the edges of the PIV windows and therefore not fully captured. Hence these points are omitted in the shown graphic.

For obtaining the total circulation the vorticity ω was integrated over a square with the edge length R_S weighted by the area. In Figure (4.8d) the total circulation can be seen in dependence of the square edge size R_S. At around $R_S/R = 0.113$ the saddle point can be perceived up-to which almost only the vorticity due to the examined vortex is included. Beyond that R_S also the vorticity of the neighbouring vortices is taken into account hence the steeper increase.

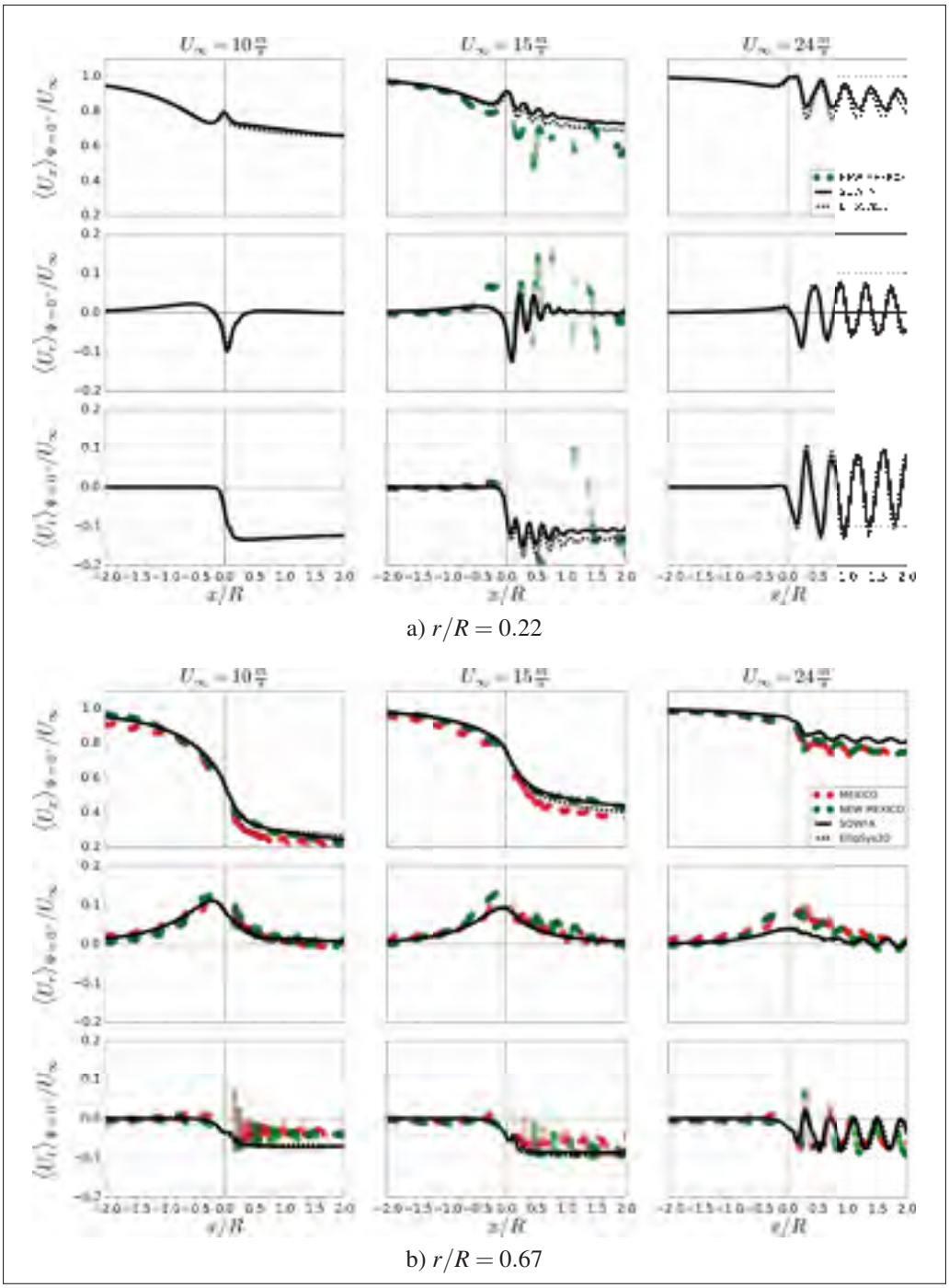

a) $r/R = 0.22$

b) $r/R = 0.67$

Figure 4.7 Axial profiles of phase averaged ($\Psi = 0^o$) velocity components for different flow cases an inboard and an outboard radial position.

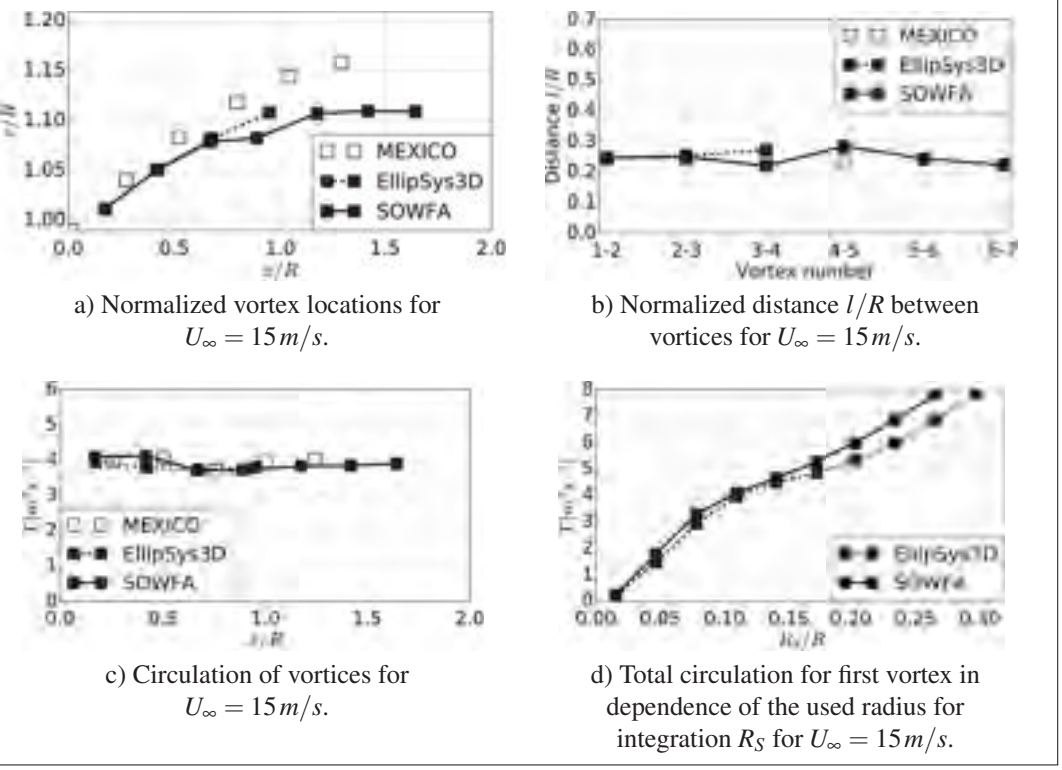

a) Normalized vortex locations for $U_\infty = 15\,m/s$.

b) Normalized distance l/R between vortices for $U_\infty = 15\,m/s$.

c) Circulation of vortices for $U_\infty = 15\,m/s$.

d) Total circulation for first vortex in dependence of the used radius for integration R_S for $U_\infty = 15\,m/s$.

Figure 4.8 Comparison of the vortex properties in the near wake.

The two examined frameworks, EllipSys3D and SOWFA, compare very well in the near wake of the rotor used in the MEXICO and NEW MEXICO experiment. When comparing them against experimental data it can be seen that they predict well the experimental results from the NEW MEXICO experiment while having a slight over-prediction to compared to the MEXICO experiment probably due to a lower inlet velocities in this experiment. Even vortex properties matched among the simulations and predicted the same trend as in the MEXICO experiment, although the resolution in the rotor vicinity might be too coarse for well resolving the helicoidal vortex structure.

Despite the different velocity sampling methods, both frameworks obtain very similar velocities and AOAs. Both AL implementations fail at the moment where the 2D airfoil data does not take into account the 3D effects of the rotating blades. As this occurs only for a very high

velocity at the most inboard location, it is very encouraging for using only non-altered airfoil data in the presented case.

It is therefore concluded that the here presented adaptions of the ALM implementation of SOWFA agrees very well with other implementations such as EllipSys3D and also with experimental results from the MEXICO project.

4.2 Numerical setup

After the method is validated, the focus will be now shifted towards the comparison of the ALM and the ASM against experimental values from the MEXICO project. The resolution around the rotor location has to be refined for allowing the ASM to be effective and also for a better resolution of the vortical structures shed from the tips and trailing edges.

In order evaluate the appropriate dimensions of mesh and refinement zones for the final case setup, first a sensitivity analysis is conducted on the domain extensions in axial and lateral direction. The nomenclature of the variables describing the mesh properties are the same as shown in Figure (4.2).

First the impact of the outer mesh dimensions x_0, x_1 and $L_{y,z}$ is examined on simulation results. In Figure (4.9) and Figure (4.10) the radial profiles of the axial component of the time-averaged velocity $\langle U_x \rangle$ and the mean axial turbulence intensity $\langle TI_x \rangle$ are shown. The variables used as indicators are first-order statistics such as the velocity components and second-order statistics such as the turbulence intensity derived by the resolved stress tensor, e.g. for the mean longitudinal turbulence intensity it is $\langle TI_x \rangle = \sqrt{\langle uu \rangle}/\langle U_x \rangle$ with $\langle \cdot \rangle$ as the time average.

For the closest inlet position and smallest domain width in Figure (4.9a) and Figure (4.9c) respectively, it can be seen that slight differences exist. For the inlet position this is due to the approaching of the boundary condition at the inlet which is a Dirichlet condition. Hence the fixed reference velocity value at the inlet is imposed at a position, where in the cases for $x_0/R < -5$ the rotor induction is already felt.

a) Variation of inlet position x_0/R

b) Variation of outlet position x_1/R

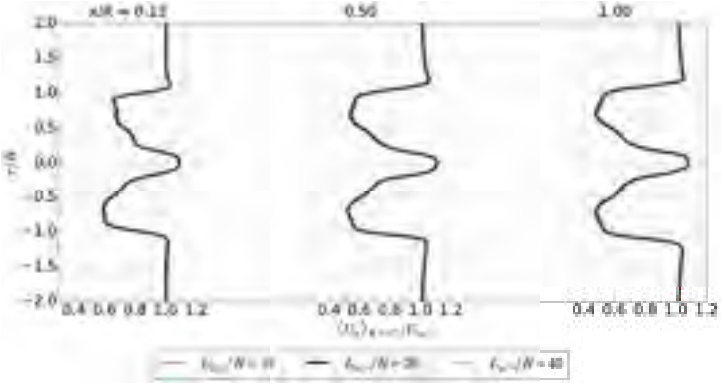

c) Variation of domain width $L_{y,z}/R$

Figure 4.9 Radial profiles of phase-averaged axial velocity component $\langle U_x \rangle_{\Psi=0^\circ}$ for sensitivity study for the normalized global mesh dimensions x_0/R, x_1/R and $L_{y,z}/R$.

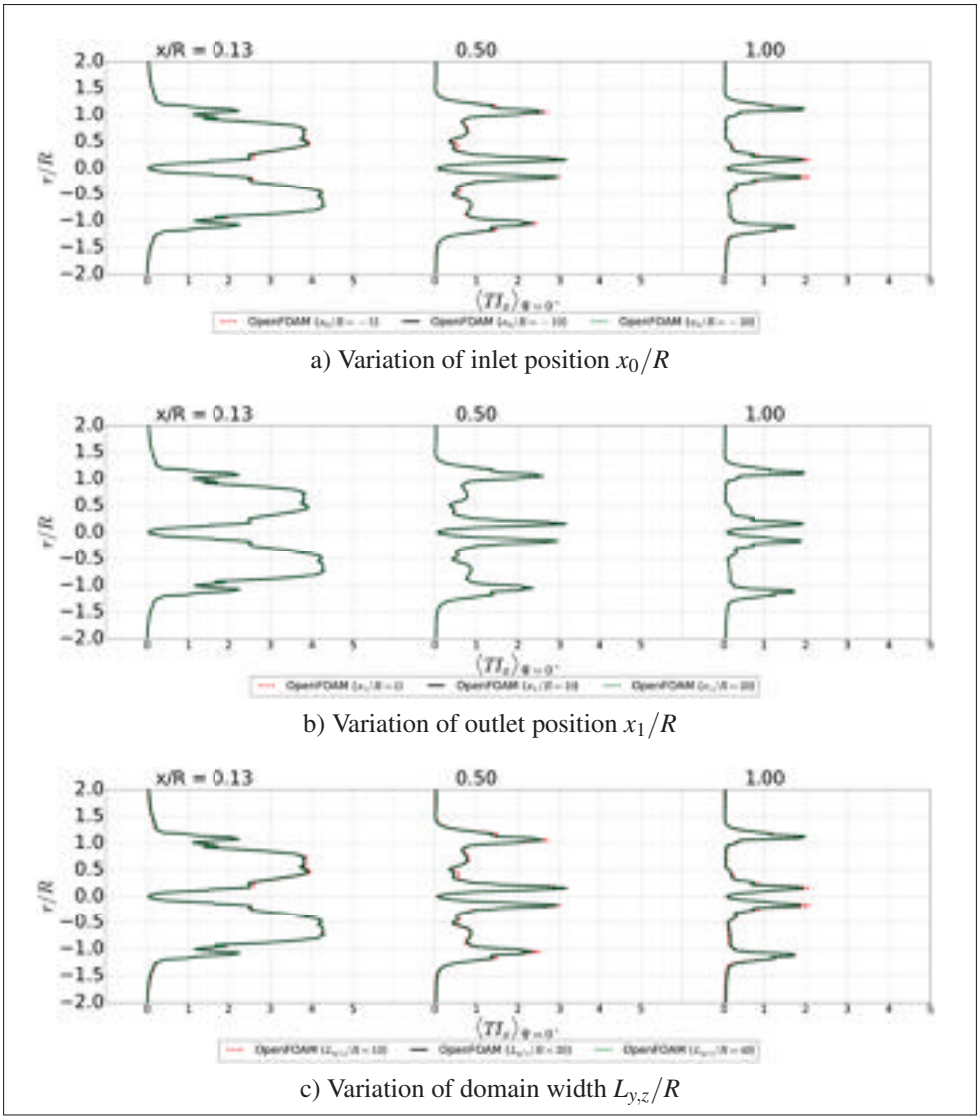

a) Variation of inlet position x_0/R

b) Variation of outlet position x_1/R

c) Variation of domain width $L_{y,z}/R$

Figure 4.10 Radial profiles of $\langle TI_x \rangle$ for sensitivity study for the normalized global mesh dimensions x_0/R, x_1/R and $L_{y,z}/R$.

When the domain width becomes too narrow the lateral boundary conditions hinders the free wake expansion and a blockage effect can be observed. Blocking the wakes expansion leads to an acceleration of the flow and hence to higher velocity values. The highest difference occurs for the lateral extent and its mean is around 0.2 % which is obtained by subtracting the radial profiles of the two cases and normalizing it by the reference velocity.

It is interesting to note that approaching the outlet position towards the rotor has almost no impact on the indicator variables as seen in Figure (4.9b). A similar verdict can be reached when looking at the second-order statistics in Figure (4.10b). The inlet boundary condition and blockage effect also result in a higher turbulence intensity. The highest mean difference between reference case and smaller case is $0.04\,\%$ for the lateral domains extensions $L_{y,z}$ when subtracting the turbulence intensity profiles of the two cases.

It can therefore be concluded by the variables observed, that results are most sensitive to the lateral extents, then the inlet position and a lesser significance for the outlet position. The new reduced domain dimensions are set as shown in Table (4.1).

domain dimensions	$\{L_x, L_{y,z}\}$	$\{10R, 10R\}$
inlet position	x_0	$-5R$
outlet position	x_1	$5R$

Table 4.1 Global mesh dimensions after sensitivity analysis.

Based on these dimensions a closer look on the sensitivity of the indicator variables on the refinement zone dimensions is taken. As sketched out in Figure (4.2), the start and the end of the refinement zone in axial direction and the lateral extents, x_{00}, x_{11} and w respectively are reduced and their impact on the results is observed. As vortex properties have a particular importance in the observation of near wakes of wind turbines, the resolution inner refinement zone is set at $\Delta x = D/128$ in contrast to $\Delta x = D/64$ as done for the base case in the Section 4.1. It can be seen from the results in Figure (4.11) and Figure (4.12) that there is not a noticeable impact on the results when reducing the refinement zone. The difference between the cases are even smaller than the ones presented for the global mesh dimensions. The lower limit for the final mesh is twofold. First as discussed in Chapter 2 there is a certain amount of uniform cells needed around the rotor for distributing the body force and secondly as the first shed tip vortex is used for comparisons it has to fall within the refined zone.

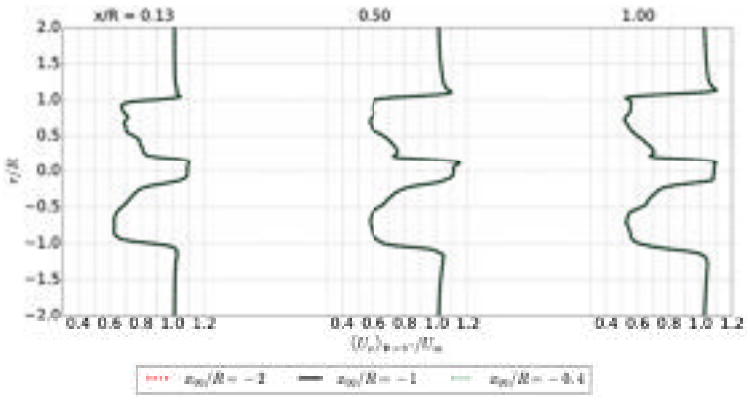

a) Variation of start of refinement zone x_{00}/R

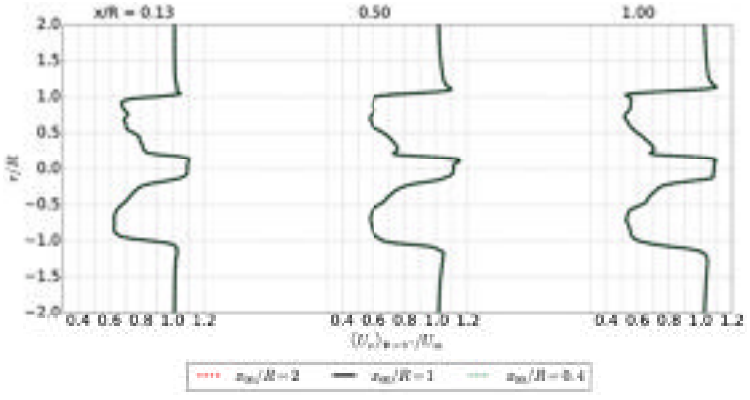

b) Variation of end of refinement zone x_{11}/R

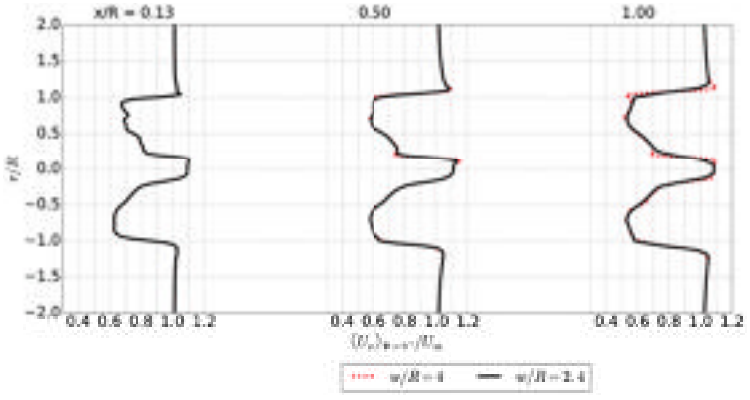

c) Variation of lateral extent of refinement zone w/R

Figure 4.11 Radial profiles of phase-averaged axial velocity component $\langle U_x \rangle_{\Psi=0^\circ}$ for sensitivity study for the normalized refinement zone dimensions x_{00}/R, x_{11}/R and w/R.

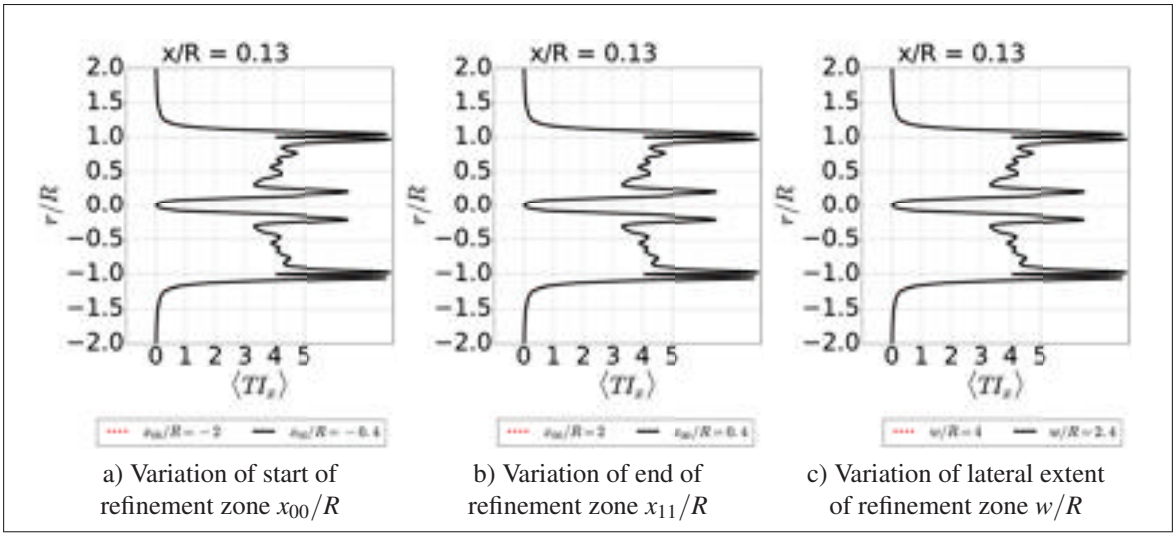

a) Variation of start of refinement zone x_{00}/R

b) Variation of end of refinement zone x_{11}/R

c) Variation of lateral extent of refinement zone w/R

Figure 4.12 Radial profiles of $\langle TI_x \rangle$ for sensitivity study for the normalized refinement zone dimensions x_{00}/R, x_{11}/R and w/R.

When looking at Figure (4.13) the first vortex still seems to be well represented in the final case while the vortices further downstream dissipate quicker due to the coarsening of the grid. When taking a closer it is revealed that the location of the first vortex still coincides and also its strength is still the same. Hence the final parameter for the refinement zone are shown in Table (4.2).

beginning (axial)	x_{00}/R	-0.4
end (axial)	x_{11}/R	0.4
lateral extent	w/R	2.4

Table 4.2 Refinement zone dimensions after sensitivity analysis.

4.3 Results

When refining the grid using the actuator line method the distribution parameter ε has to be adjusted in accordance in order to obtain a global torque close to the reference value. In the following only the case for $U_\infty = 15\,m/s$ will be examined as the other cases in Section 4.1 served as extreme cases for determining how the model behaves at its limits.

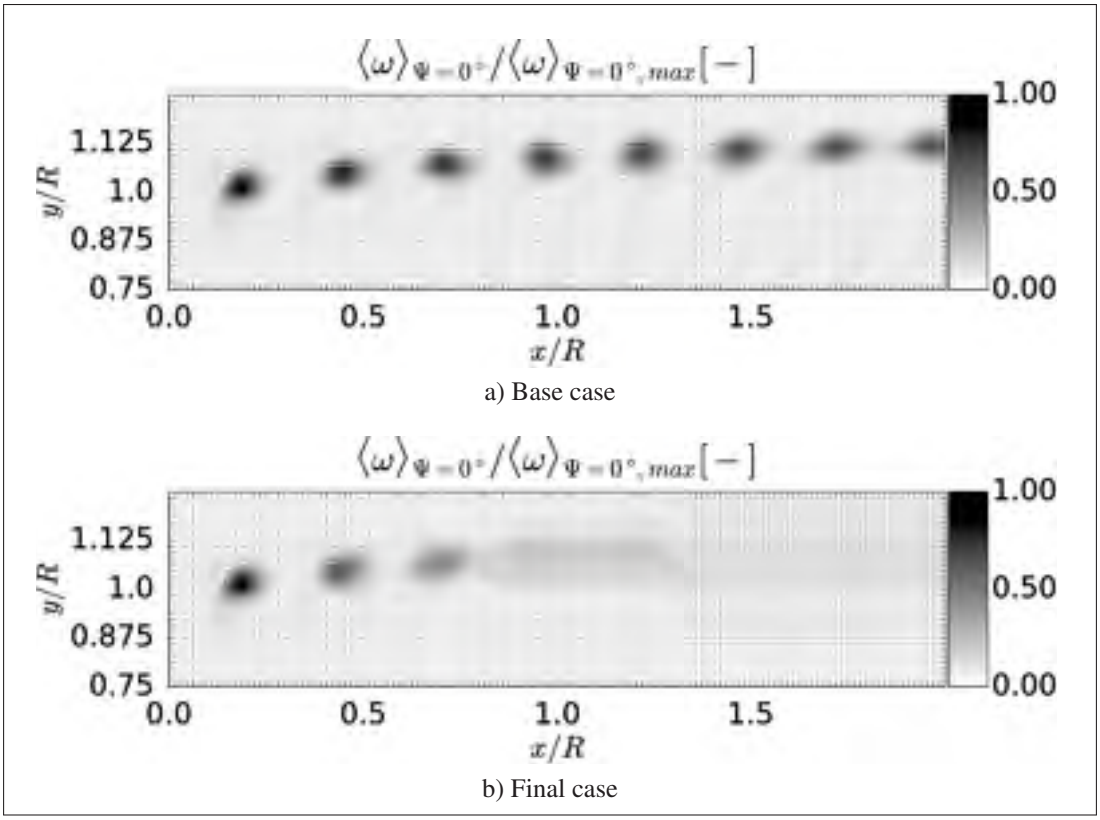

Figure 4.13 Normalized vorticity $\langle\omega\rangle_{\Psi=0^\circ}/\langle\omega\rangle_{\Psi=0^\circ,max}$ surface plots in of the wake edge for the base and final case.

While other work often relies on a constant $\varepsilon = 2\Delta x$ for different grid resolutions as done e.g. by Ivanell *et al.* (2010), this work adapts the ε in accordance with the grid resolution. This can be seen as a first step towards an actuator surface method, where the force is distributed in respect to the blades chord. The results are shown in Figure (4.14). A confidence interval of $\pm 1\,\%$ was established around the reference torque value T_{ref} and through iteration a distribution parameter is found for the simulation to fall in the range.

The lower bound for the distribution parameter here is $\varepsilon = 1.7\Delta x$ for the sake of numerical stability of the here chosen method. Other frameworks applying a different numerical discretization can go even lower e.g. in Nilsson *et al.* (2015). By doing so it can be seen that the best solution in terms of global torque for a resolution of $N = D/\Delta x = 32$ is off by around $4\,\%$ in Figure (4.14a).

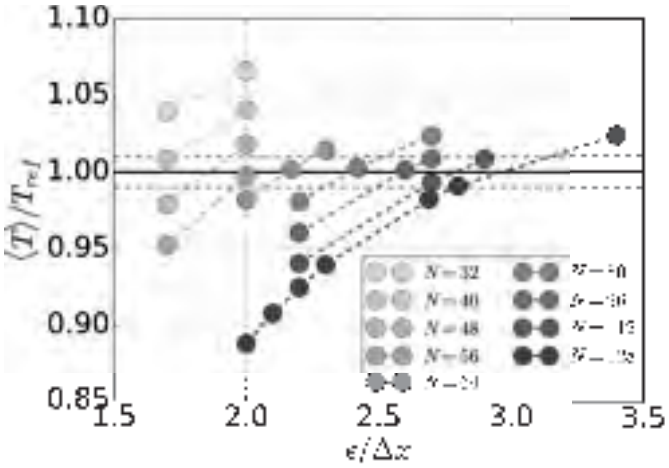

a) Relation between $\varepsilon/\Delta x$ and resulting global torque normalized by reference torque for $U_\infty = 15\,m/s$.

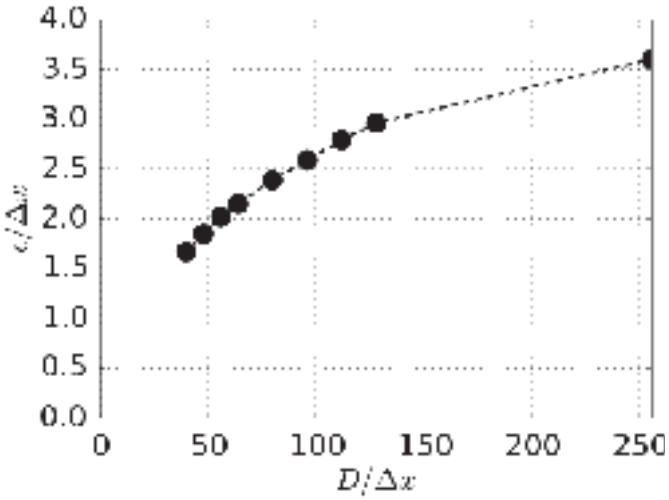

b) Optimal ε over number of cells for resolving one rotor diameter $D/\Delta x$.

Figure 4.14 Optimal ε for obtaining global torque in dependence of grid resolution.

As a general trend it can be seen that ε has to be increased with increasing resolution. This stems from the fact that by refining the mesh with a constant ε the punctual induction caused by the blade would be too high and eventually the torque would be below the reference value, e.g. for $\varepsilon = 2\Delta x$ for $N \geq 64$. In contrary when having a very low resolution a constant ε distributes the force too widely, causing a lower induction around the rotor resulting in an overestimation of the torque, e.g. for $\varepsilon = 2\Delta x$ for $N \leq 48$.

The optimal distribution parameter $\varepsilon/\Delta x$ found in Figure (4.14a) are now shown in dependence of the grid resolution N in Figure (4.14b). It seems as if this value would reach eventually an asymptotic limit. When looking at a more theoretical approach in Martínez-Tossas *et al.* (2015) it is suggested that the optimal distribution width ε lies between $0.14-0.25$ of the chord c. In this case for $D/\Delta x = 128$ the relation ε/c is between $0.5-8.9$ depending on the spanwise location. The observation made by Martínez-Tossas *et al.* (2015) is backed by Shives & Crawford (2013) where ε/c is situated in the same range. But it should be kept in mind that Shives & Crawford (2013) uses a much higher grid resolution allowing $\varepsilon/\Delta x \geq 4$ and Martínez-Tossas *et al.* (2015) $\varepsilon/\Delta x \geq 5$.

The curvature in Figure (4.14b) also confirms the findings of Jha *et al.* (2013) that keeping a constant $\varepsilon/\Delta x$ leads to an undesired behaviour. While Ivanell *et al.* (2010) suggests to choose the smallest possible distribution width ε ($\varepsilon/\Delta x = 1$ in that case), the observations of this work follow rather the work of Shives & Crawford (2013) suggesting the adaptation of ε in dependence of the grid resolution in order to distribute the force over a meaningful length scale.

For an excerpt of the resolutions presented in Figure (4.14) the radial profiles of the velocity components can be found in Figure (4.15). It can be seen that the method seems to converge towards a profile. The second doubling of the resolution results in a less significant change than the first one. As shown in Figure (4.14) the lowest resolution at $N = 32$ over-predicts the torque by distributing the force to widely which also reflects as well downstream at $x/R = 0.13$ in the axial velocity component U_x/U_∞. Despite following well the trend of the experimental values the method seems to converge towards radial profiles which are especially off in the tip and hub region where the strongest vortices are shed. This seems to be the limitations intrinsic of the ALM which is less apparent when using high fidelity approaches such as fully resolved rotor simulations (Carrión *et al.*, 2015).

When looking at the axial profiles of the velocity components in Figure (4.19) it is again seen that the solution seems to converge when increasing the resolution. The behaviour of the

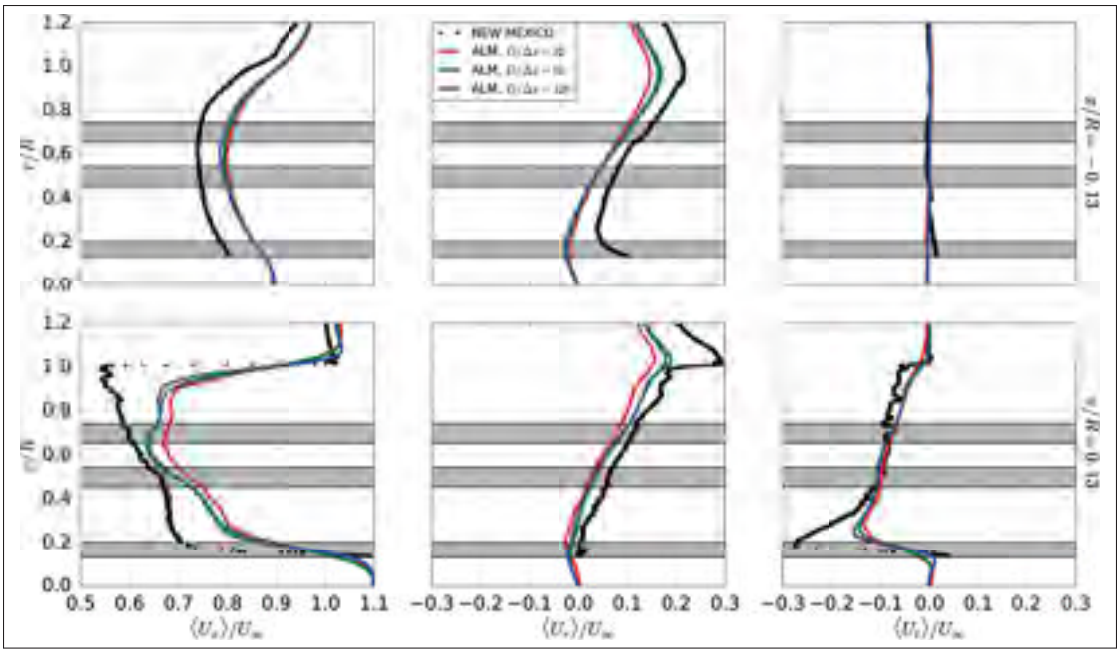

Figure 4.15 Radial profiles of time-averaged velocity components $\langle U_i \rangle$ for ALM in different grid resolutions.

solution within the refined zone with $-4 < x/R < 4$ is similar to the one of the radial profiles in Figure (4.15).

While the vortex sheets emitted from the blade are particularly visible in the hub region (r/R = 0.22) by the oscillating axial velocity downstream, it also starts to become visible for the higher resolution with $N = 128$ in the tip region $r/R = 0.67$. It is very interesting to notice that while the model is in very good agreement for $x/R > 0.5$ it seems to underestimate the induction in the region with $-1 < x/R < 0.5$ which is also visible in Figure (4.15).

Hence while ALM is often used for near wake analysis such as Nilsson *et al.* (2015), Ivanell *et al.* (2010), it slightly misrepresents the ultimate vicinity of the rotor up- and downstream. Much better results can be obtained by a fully resolved rotor simulation as done by Carrión *et al.* (2015).

As Vermeer *et al.* (2003) stated a good force distribution would enhance the representation of the induction caused by the blade passage. Hence the azimuthal profiles are visualized

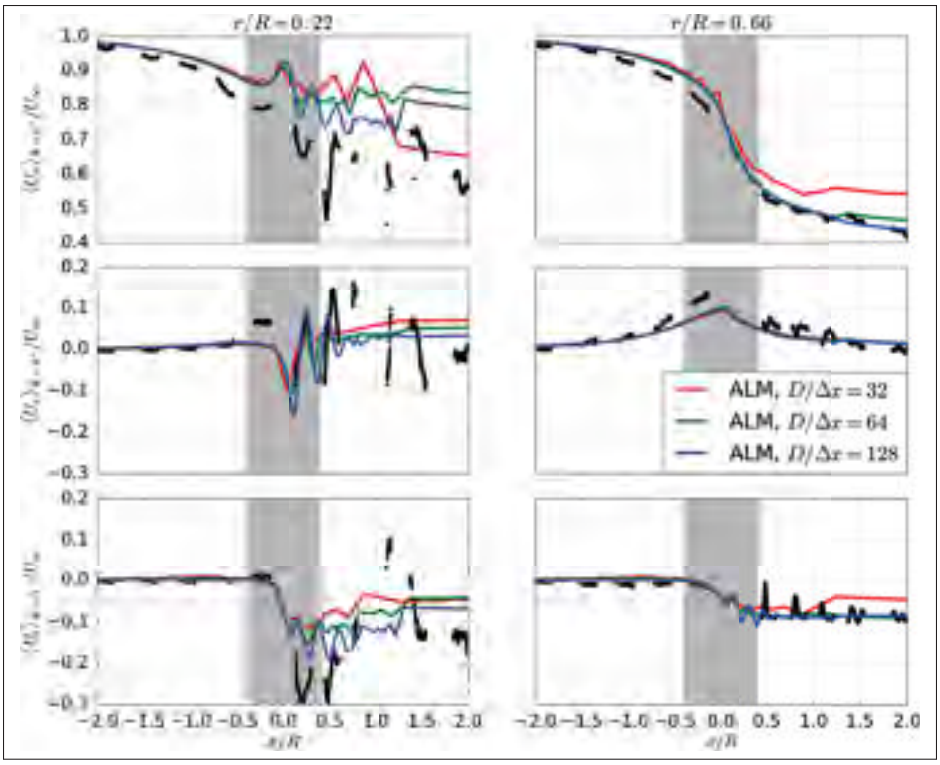

Figure 4.16 Axial traverses of normalized velocity components phase-averaged for azimuthal angles of $\Psi = 0°$ for ALM in different grid resolution. The grey area indicates the refined zone in the domain center.

in Figure (4.17). And indeed for a higher resolution the solution gets much closer to the experimental values from the NEW MEXICO experiment in particular for the upstream region but also for the mid-section for the downstream region. Again the mismatch in the downstream region results most probably from not capturing well the shed vortices at e.g. $r/R = 0.92$ and $x/R = 0.13$.

The next step in the transition from the ALM to the ASM would be to spread the forces in accordance to the chord width. This is done by applying the smallest possible distribution parameter $\varepsilon = 1.7\Delta x$ at the tip and proportionally vary the ε along the span. When looking at Figure (4.18) and especially in Figure (4.18b) it can be seen that this results in a very slight improvement of the tip representation and its induction on the axial velocity component. But when looking at Figure (4.18a) it can also be stated that this amelioration is bought at the ex-

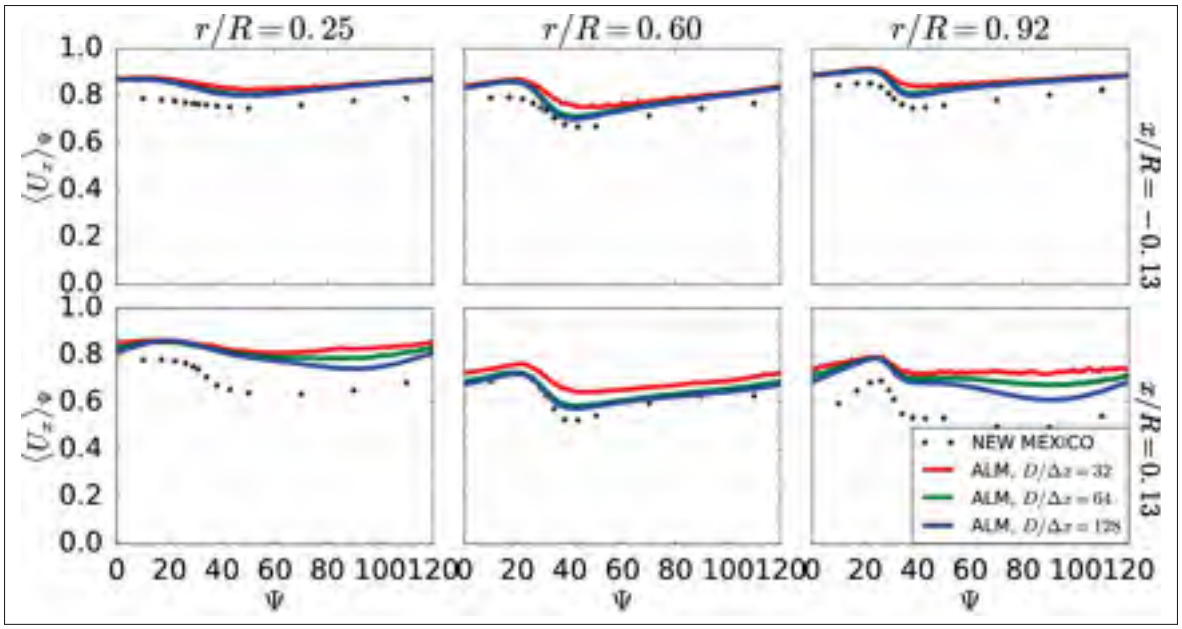

Figure 4.17 Azimuthal traverses of normalized velocity components phase-averaged for different azimuthal angles for ALM in different grid resolutions.

pense of too widely distributing the force towards the hub where the blade chord increases. Hence when increasing the resolution if further $N > 128$ this phenomenon is expected to become even more significant and hence doubts should be cast on proceeding in this way.

This effect can also be seen in the hub region when looking at the axial profiles in Figure (4.19). Hence when spreading the force in accordance with the chord the agreement lessens a lot in the region where the chord length grows.

Therefore this approach was not more refined by e.g. also adjust the distribution for the thickness or the blade twist. Instead the ASM used throughout this work is in fact an ALM with an adapted distribution parameter ε in dependence of the resolution.

When looking at the vorticity shed by the method for different resolutions in Figure (4.20) it can be clearly seen that with increasing resolution the vortical structures become more distinct. While tip and root vortex are clearly noticeable, it is interesting to observe that at transition

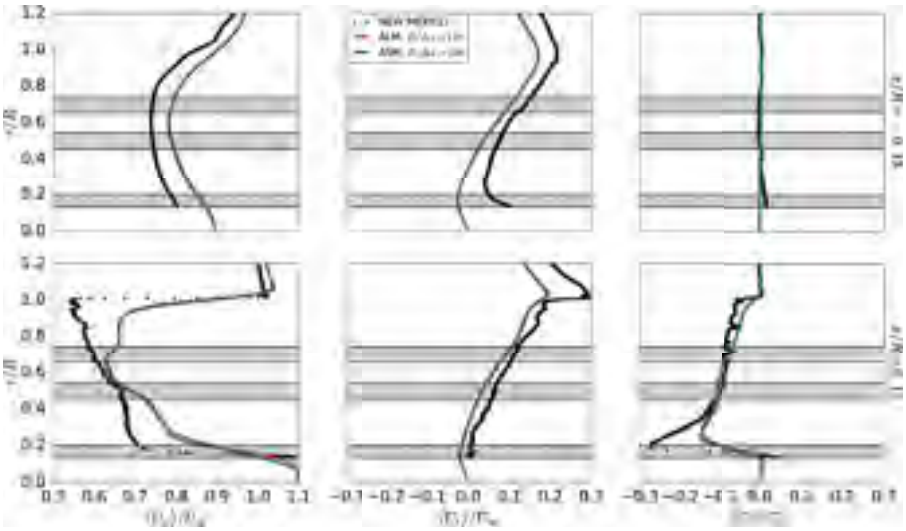

a) All three velocity components.

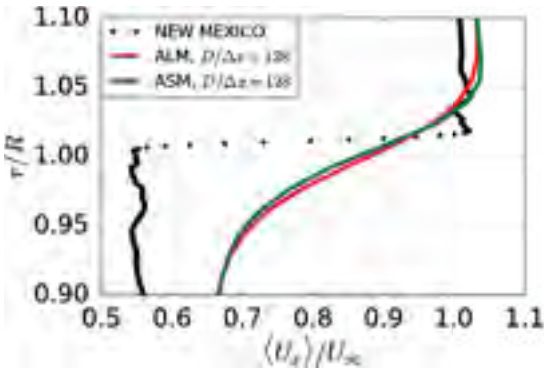

b) Zoom on tip region of axial component.

Figure 4.18 Radial profiles of time-averaged velocity components $\langle U_i \rangle$ for comparing ALM and ASM.

towards the mid-section airfoil $0.54 < r/R < 0.66$ also some strong vortical structures occur. This is due to the incompatibility of this airfoil with the other two.

When zooming in on the first tip vortex as done in Figure (4.20) and comparing it to the experimental vortex in Figure (4.21b) and at a smaller scale in Figure (4.22), it can be seen that though global torque values and near wake results for $x/R > 0.5$ are in a very good agreement, the representation of the tip vortex is rather crude.

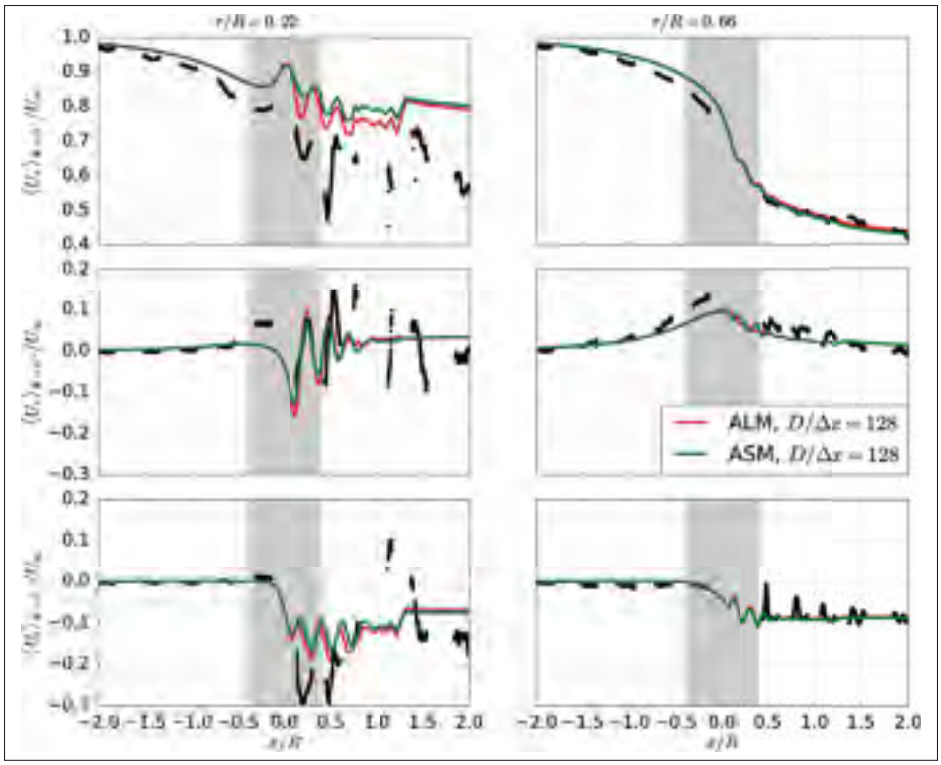

Figure 4.19 Axial profiles of normalized velocity components phase-averaged for azimuthal angles of $\Psi = 0^\circ$ for comparing ALM and ASM.

Also a slight idea of a secondary vortex can be perceived at the top-left corner of the primary vortex for $N = 128$, it is far away from what is seen in reality in Figure (4.22) or with a fully resolved rotor geometry in Carrión *et al.* (2015).

So in order to estimate what resolution would be necessary in order to obtain a more realistic vortex structure the radial variation of some of the vorticities in Figure (4.20) is shown in Figure (4.23a). It can be clearly seen how the vortex concentrates with an increased resolution.

When defining the vortex radius r_{core} as the limit containing 99 % of the vorticity the radii as depicted in Figure (4.23b) can be found. The Gaussian distribution is used as an approximation for the vorticity distribution within the vortex, which holds well as the force is also distributed in a Gaussian manner. It is also confirmed by the comparison of the Gaussian distribution

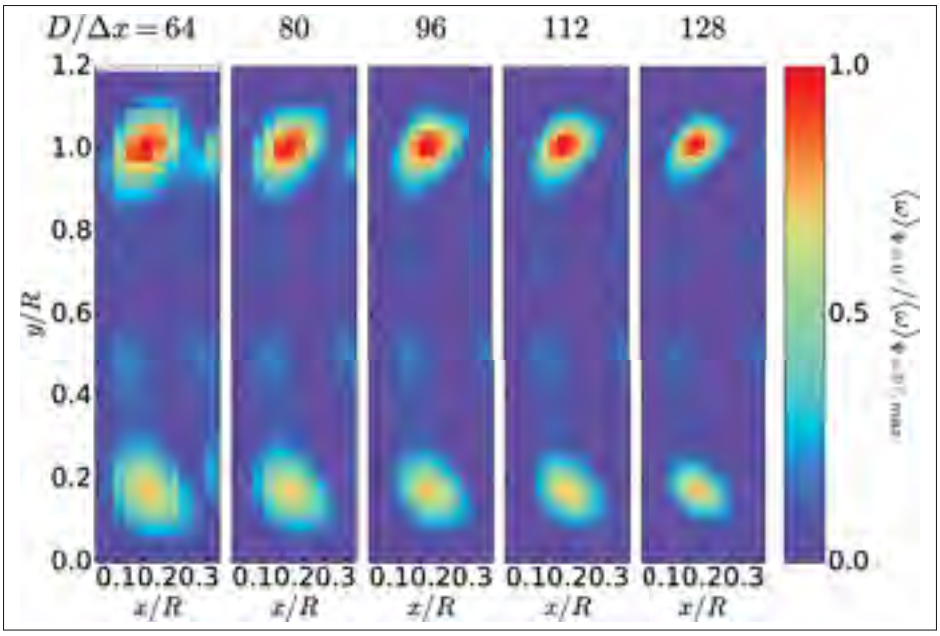

Figure 4.20 Normalized vorticity $\langle\omega\rangle_{\Psi=0^\circ}/\langle\omega\rangle_{\Psi=0^\circ,max}$ in the near wake for different grid resolutions.

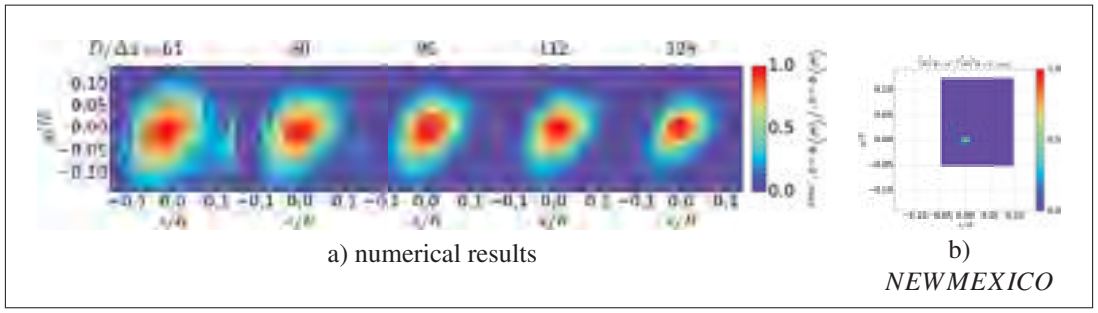

a) numerical results

b)
NEWMEXICO

Figure 4.21 Vortex form and size visualized by normalized vorticity $\langle\omega\rangle_{\Psi=0^\circ}/\langle\omega\rangle_{\Psi=0^\circ,max}$ of the first shed tip vortex for different grid resolutions.

and the vorticity for $N = 128$ in Figure (4.23a). Hence by using this approximation a possible distribution parameter ε can be deduced as shown in Figure (4.23b).

This would result in excessive demands for the mesh size with the here presented case which would result in a computational grid of more than $1 \cdot 10^9$ cells with the presented meshing approach and it would be beyond any justifiable computational scope. Fully resolved rotor calculations as conducted by Carrión *et al.* (2015) allowed to obtain tip vortices of $r_{core}/R \approx 0.2$

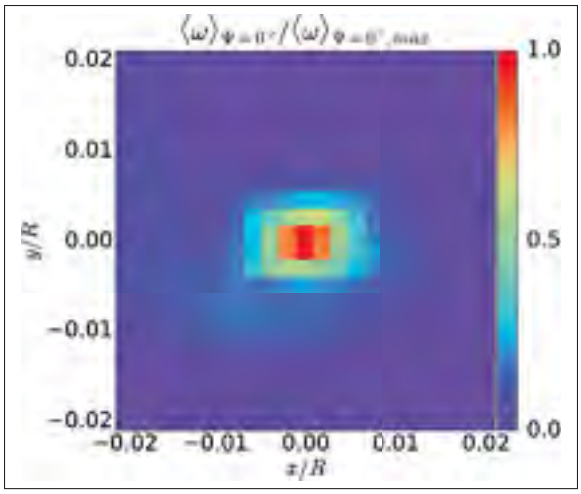

Figure 4.22 Normalized vorticity $\langle\omega\rangle_{\Psi=0^\circ}/\langle\omega\rangle_{\Psi=0^\circ,max}$ of experimental vortex of MEXICO experiment.

for $N \approx 900$ in the tip region which corresponds very well to results in Figure (4.23b). Another result for the vortex radius can be found in Nilsson *et al.* (2015) where for $\varepsilon/R = 0.012$ a vortex core radius of $r_{core}/R \approx 0.055$ was found.

4.4 Conclusion

The validation of the method used in this work against the EllipSys3D framework is very encouraging. It shows that although the methods for velocity sampling are slightly different, both framework yield very similar results. This results also in a very good agreement on all subsequent results such as the blade forces, velocity components and vortex properties. When verifying the results with the MEXICO and NEW MEXICO experiments it firstly was shown that both frameworks reproduce very well at least the cases for $U_\infty = 10\,m/s$ and $U_\infty = 15\,m/s$. While the model breaks down for the last case with $U_\infty = 24\,m/s$ towards the hub, the results demonstrate that, even with unmodified 2D airfoil data without taking the dynamic stall into account, this airfoil data can be used for a wide range of wind speeds.

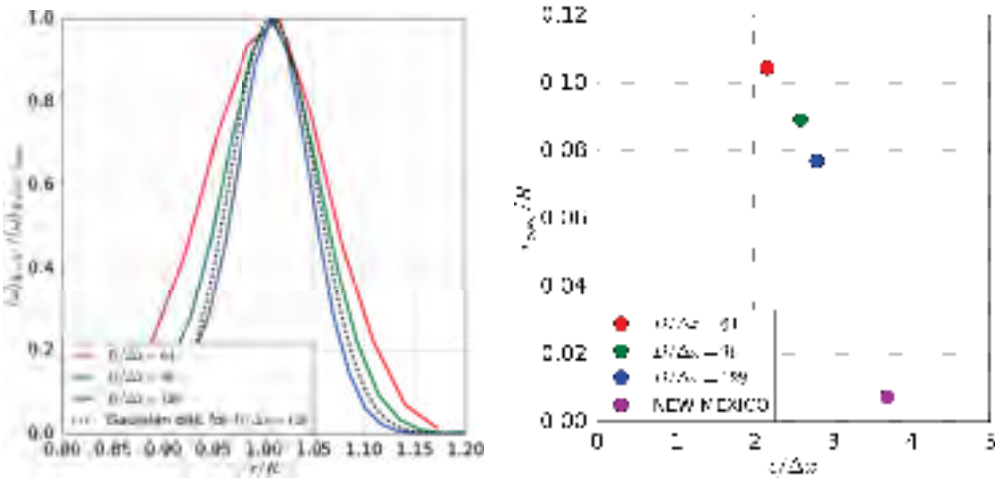

a) Radial profiles of normalized vorticity $\langle\omega\rangle_{\Psi=0^\circ}/\langle\omega\rangle_{\Psi=0^\circ,max}$.

b) Normalized vortex radius r_{core}/R over normalized distribution parameter ε/R

Figure 4.23 Radial vorticity distribution and vortex radii in dependence of distribution parameter.

Another very interesting aspect is the non-linear dependence of the distribution width on the grid resolution. It is also shown that with increasing grid resolution the spatial profiles seem to converge. This would be one aspect of a grid independent solution, but it is still very far away from resolving correctly the shed tip vortices. Although it seems to converge towards a value of $\varepsilon \approx 4-5\Delta$ for $N \geq 1024$ this would necessitate meshes of more than one billion cells. At this point the actuator force model should probably be abandoned and a fully resolved rotor simulation should be used with are non-uniform meshing strategy.

The ALM seems to have a limit in the downstream direction where the distinct blades are no longer discernible and the cheaper ADM could be used. It is also found that the velocity deficit started to match experimental values for $x/R > 5$ which would establish the lower barrier towards the rotor.

CHAPTER 5

CASE 2: HOMOGENEOUS ISOTROPIC TURBULENCE

In order to approach a more realistic flow model homogeneous isotropic turbulence is now introduced at the inlet. First there will be an examination of the turbulent field within the numerical simulation. Then results of the immersed rotor model are shown and discussed ending with some concluding remarks.

5.1 Evaluation of imposed turbulence

When looking at the global flow with the synthetic turbulence intensities $TI_{syn} = 0.1\,\%$, $5\,\%$, $10\,\%$ and $15\,\%$ in Figure (5.1) it is interesting to notice that very similar features arise. This stems from the fact that the same seed is used for the random number generator in the implementation of the Mann algorithm of Gilling (2009). Due to the difference in turbulence intensities they seem to evolve slightly different.

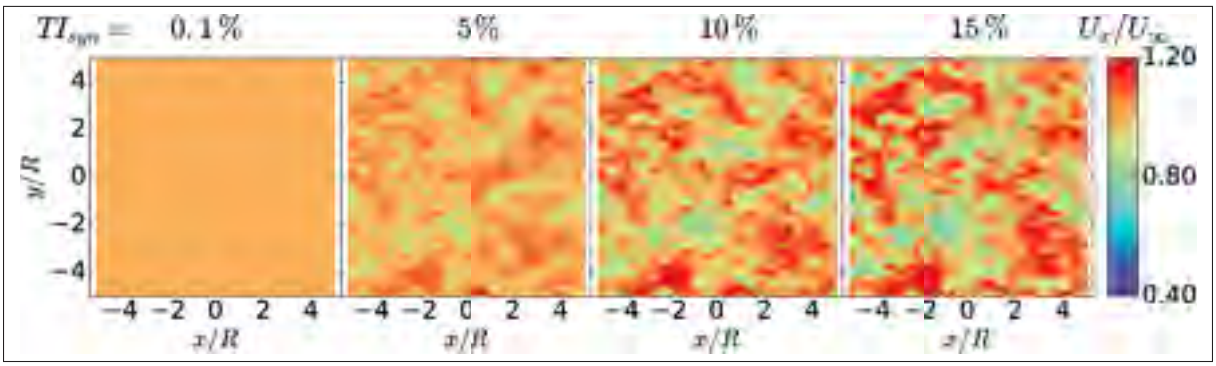

Figure 5.1 Midplane at $y/R = 0$ of instantaneous normalized axial velocity component U_x/U_∞ showing homogeneous isotropic turbulence for different turbulent intensities TI_{syn} in numerical domain.

In Figure (5.2) the longitudinal evolution of the turbulence intensities and fractions of resolved turbulent kinetic energy can be observed. As seen in Figure (5.2a) there is a stronger decay for higher turbulence intensities which was also found in Olivares Espinosa (2017). In the case of

Olivares Espinosa (2017) where EllipSys3D was compared to a solution based on OpenFOAM that over the same longitudinal distance of $10R$ a decay of 48 % and 44 % was found for each framework respectively. The major reason behind this extreme turbulence decay is due to the violation of the Nyquist-Shannon criterium, as in Olivares Espinosa (2017) the relation of the resolutions of the synthetic and computational grid is unity. This stands in a stark contrast to the 4 % in this case for the high turbulence intensity case. This huge decay which is even more significant for EllipSys3D necessitates to approach the introduction of the turbulence close to the turbine for high turbulence intensity cases (Olivares Espinosa, 2017). At the end of the domain there is a sharp rise due to the influence of the boundary conditions at the outlet. This seems to have only a local impact which augments for coarser resolutions.

When taking the case for $TI_{syn} = 5\,\%$ it is interesting to notice that while the resolved TI (green dashed line) is around 4.2 % at the rotor position $x/R = 0$ a huge part of the difference in relation to the imposed turbulence falls in the sub-grid and finally just a relatively small amount of the turbulent intensity or turbulent kinetic energy is "lost" during the transfer from the synthetic turbulence field to the computational domain.

It should be kept in mind though, that the TI, the rotor model is experiencing directly through velocity sampling, is TI_{res}. Therefore TI_{sgs} is only felt indirectly by an augmentation of the effective viscosity.

In Figure (5.2b) it can be seen how much of the turbulent motion is resolved and how much is modelled. The indicator used here is the fraction of the resolved turbulent kinetic energy over the total turbulent kinetic energy. It can be seen that the resolved scales exceed 96 % which lies well above the criterion of 80 % proposed by Pope (2004) and also confirmed by a study of Davidson (2009).

Interestingly in Figure (5.2b) it can be seen that in the refined zone in the vicinity of the rotor, slightly more turbulent scales end up in the resolved scales, but this almost not reflects in the turbulence intensity in Figure (5.2a). Hence the meshing strategy of successive refinement around the rotor has little effect on flow properties as also found by Vanella *et al.* (2008).

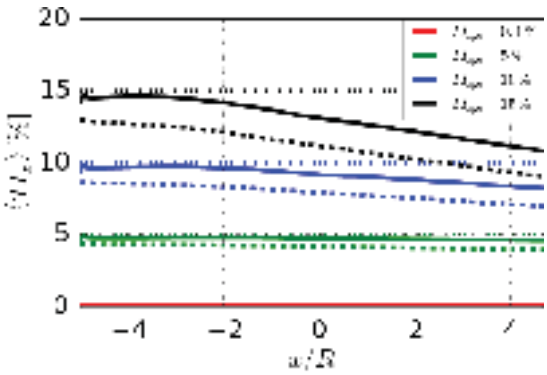

a) $\langle TI \rangle$ with $\langle TI_{res} \rangle$ (dashed line), $\langle TI_{res} \rangle + \langle TI_{sgs} \rangle$ (solid line) and TI_{syn} (dash-dotted line) as reference.

b) Fraction of resolved turbulent kinetic energy $\langle k_{res} \rangle / (\langle k_{res} \rangle + \langle k_{sgs} \rangle)$

Figure 5.2 Longitudinal evolution of resolved and modelled TI and k for different turbulence intensities.

An important aspect when imposing a synthetic turbulence as boundary conditions of a CFD simulation is respecting the Nyquist–Shannon sampling theorem (Shannon, 1949) as also mentioned by Muller (2015). Hence a study considering different ratios between the grid resolution of the synthetic turbulence and the simulation was undertaken. Its results are visualized in Figure (5.3) and it can be clearly seen that the higher the computational resolution is compared to the one of the synthetic turbulence, the less the turbulence intensity decays in longitudinal direction. While the criterion of Nyquist–Shannon states that the resolution of the computational domain should be at least twice as big, this work uses the ratio of $dx/\Delta x = 2.5$. The cell width of the synthetical field is declared as dx and of the computational mesh as Δx. In Figure (5.3b) it can also be seen how the resolved part increases with increasing resolution.

As already seen in Figure (5.1) the synthetic fields are very similar, also as they are based on the same spectrum only differing by a scaling factor $\alpha\varepsilon^{2/3}$ in order to achieve the desired variance σ. This reflects as well in Figure (5.4). There is only a slight difference between the theoretical spectra and the synthetic ones obtained by the Mann algorithm as also observed in Olivares Espinosa (2017) and Troldborg (2009). The numerical spectra are in very good agreement with the imposed turbulence and the difference on the higher wave numbers is due to

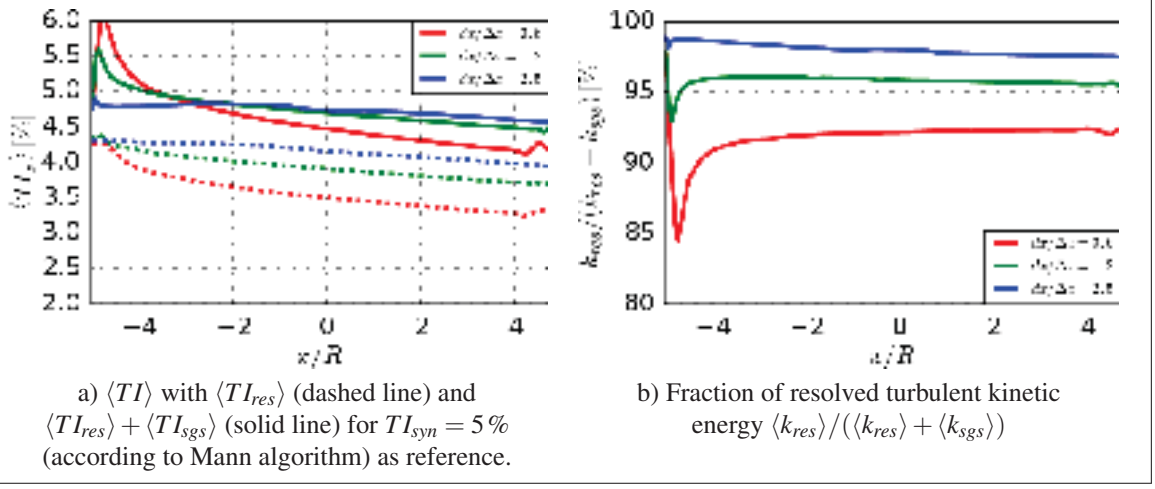

a) $\langle TI \rangle$ with $\langle TI_{res} \rangle$ (dashed line) and $\langle TI_{res} \rangle + \langle TI_{sgs} \rangle$ (solid line) for $TI_{syn} = 5\,\%$ (according to Mann algorithm) as reference.

b) Fraction of resolved turbulent kinetic energy $\langle k_{res} \rangle / (\langle k_{res} \rangle + \langle k_{sgs} \rangle)$

Figure 5.3 Longitudinal evolution of resolved and modelled $\langle TI \rangle$ and $\langle k \rangle$ for different grid resolutions.

turbulence modelling and numerical effects such as grid resolution and discretization schemes.

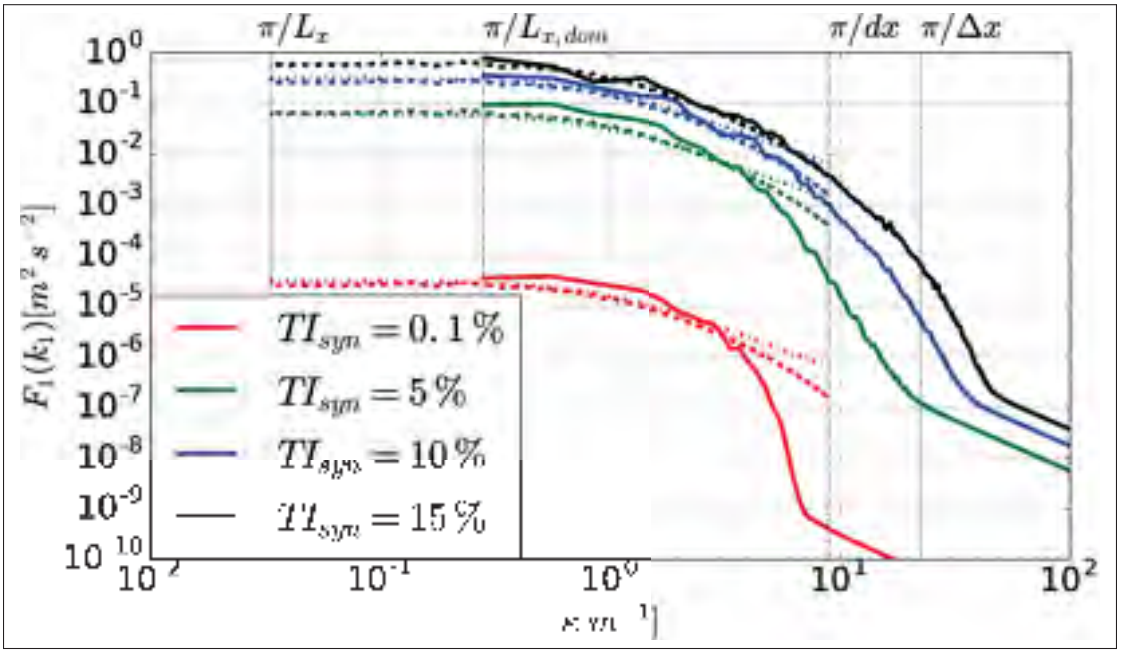

Figure 5.4 Theoretical (dot-dashed line), synthetic (dashed line) and numerical (solid line) spectra for HIT case for different turbulence intensities TI_{syn} at hub position.

The dependence of the numerical dissipation on the mesh resolution can be seen in Figure (5.3). In Figure (5.5) the influence of the other two parameters can be examined. The impact of the discretization scheme is visualized in Figure (5.5a). From the most dissipative scheme "upwind" towards the applied "LUST" scheme a clear improvement can be seen. In other work also TVD schemes in the context of LES are explored (Bidadi & Rani, 2015). But it was found that in this work the velocity gradients within the vortices are extremely steep and hence these structures get dampened when using schemes such as the TVD which adjusts itself based on the gradients.

There is a slight difference in the region upstream of the rotor position where the classic dynamic Smagorinsky approach is a bite more dissipative than the dynamic Lagrangian model.

But as soon as the more refined zone around $-4 < x/R < 4$ begins more turbulent scales are resolved and the difference between the two sub-grid model vanishes.

5.2 Results

The global torque of the turbine shows little dependence on the turbulence intensity in Figure (5.6). Therefore although there is a wide range of turbulence intensities, the resulting change is less than $1\,\%$ compared to the experimental value T_{ref}. Despite permitting a faster wake recovery and hence having a noticeable effect on a downstream turbine (Martinen *et al.*, 2014), the ambient turbulence has little impact on the extracted torque from wind. This is most probably due to the constant mean velocity in all cases and the reliance on airfoil data instead of dynamically modelling the turbulence effects on the blade as done in Vijayakumar *et al.* (2013).

In Figure (5.7), the effects of the ambient turbulence on the turbine wake are shown. While there are no noticeable impacts for the low turbulence case with $TI_{syn} = 0.1\,\%$ the beginning of a wake meandering phenomenon can be observed for $TI_{syn} > 0.1\,\%$. For $TI_{syn} = 15\,\%$ the turbulent structures seem to outgrow the structures created by the wind turbine.

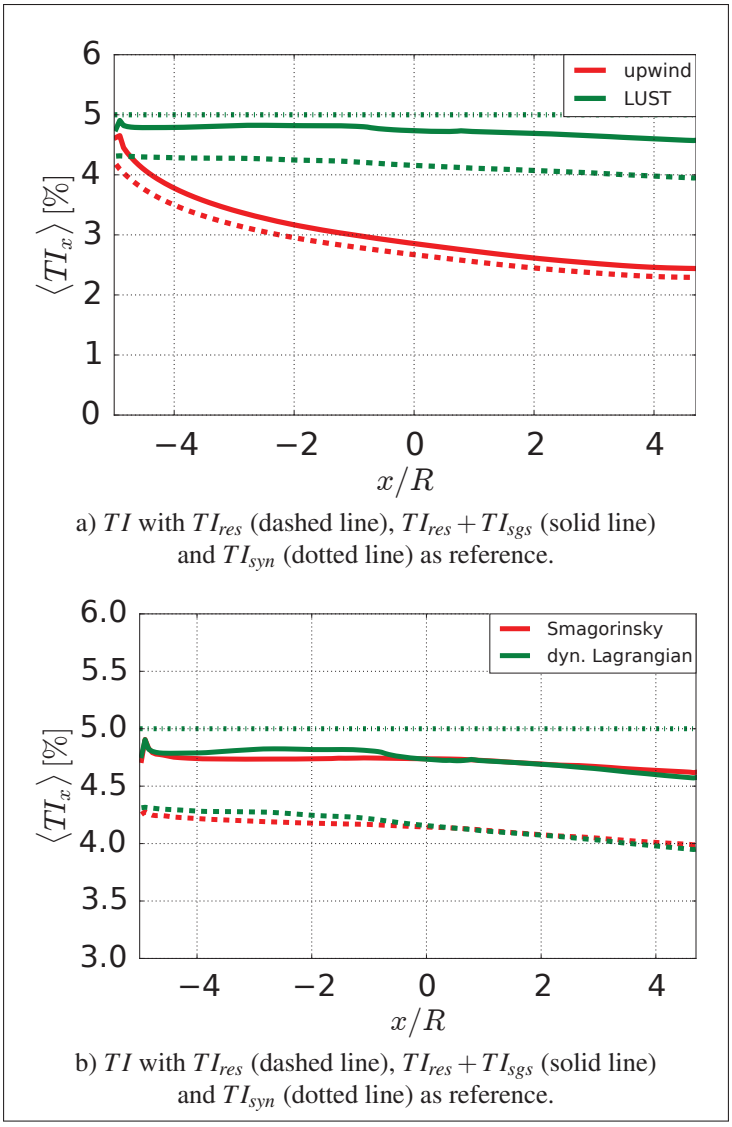

a) TI with TI_{res} (dashed line), $TI_{res} + TI_{sgs}$ (solid line) and TI_{syn} (dotted line) as reference.

b) TI with TI_{res} (dashed line), $TI_{res} + TI_{sgs}$ (solid line) and TI_{syn} (dotted line) as reference.

Figure 5.5 Longitudinal evolution of resolved and modelled $\langle TI \rangle$ for different discretization schemes and sub-grid model.

In Figure (5.7b) the wake recovery can be assessed qualitatively by looking at the mean field. Clearly the velocity deficit is well maintained for the low turbulence case with $TI_{syn} = 0.1\,\%$. For $TI_{syn} > 0.1\,\%$ wake recovery happens much faster.

It can also be noticed that due to the increasing amplitude of velocity fluctuations the time-averaging period of 40 rotor revolutions is not long enough to smooth out all velocity fluctu-

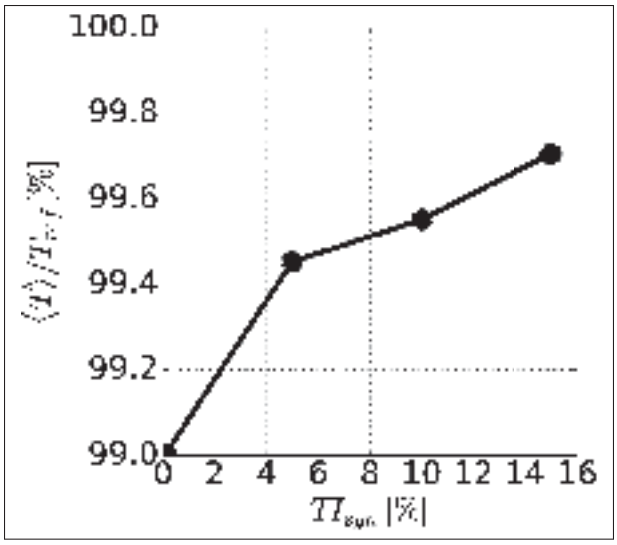

Figure 5.6 Normalized torque in dependence of turbulence intensity for homogeneous isotropic turbulence.

ations which can be seen when looking at the ambient field, especially in for $TI_{syn} > 15\,\%$. Nevertheless this fluctuations of the mean field are relatively small compared to the initial fluctuations. A better statistical convergence could be achieved by longer runtimes.

In Figure (5.8) it can first be noticed that the profiles for the cases of no turbulence presented in the previous chapter and the case for $TI = 0.1\,\%$ as specified by Schepers *et al.* (2012) are congruent. The higher the turbulence intensity the faster the wake recovery and therefore the lesser the wake deficit, which can be seen by looking at the profiles for $TI > 0.1\,\%$. Also the induction by root vortices as shown for $r/R = 0.22$ seem to be weaker when looking at the radial and tangential velocity component U_r and U_t.

When looking at the radial profiles of the velocity components in Figure (5.9) it can be seen again that the higher the TI the lesser the wake deficit and it seems to be more pronounced towards the tip. At the same time there seems to be no noticeable difference in the lateral velocity components.

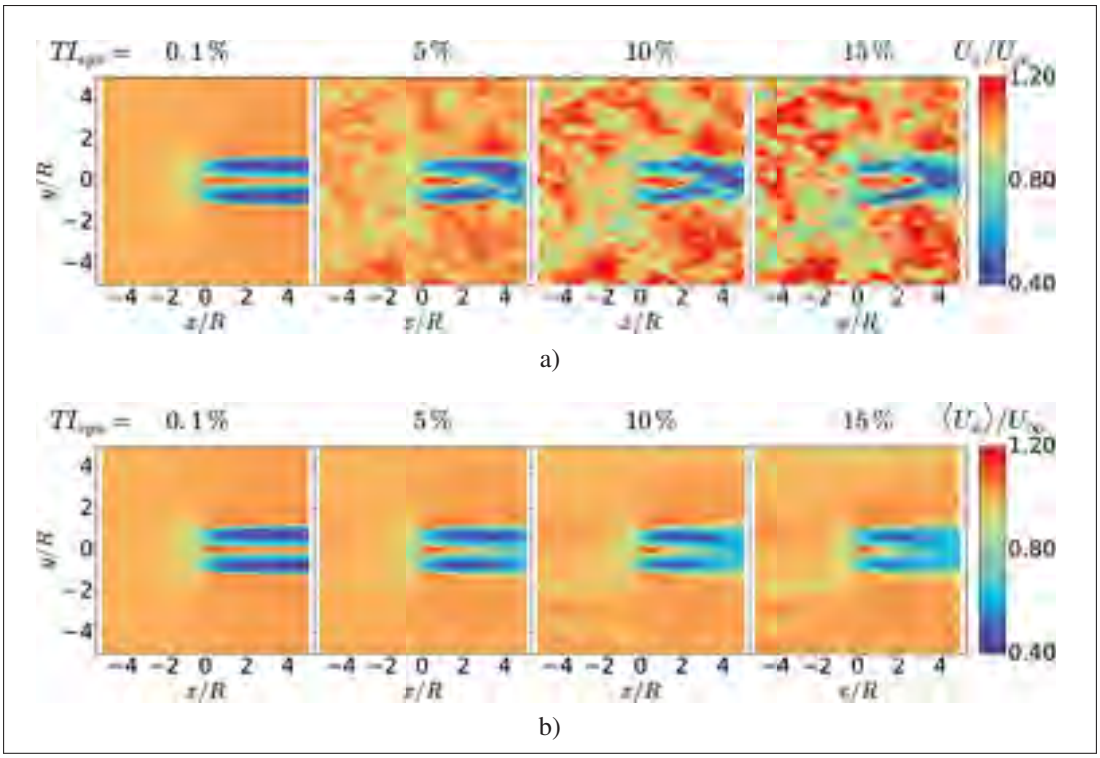

Figure 5.7 Instantaneous and mean axial velocity component U_x and $\langle U_x \rangle$ in sheared flow for different synthetic turbulence intensities TI_{syn} at hub height.

Interestingly when looking at the longitudinal evolution of the radial profiles in Figure (5.10) it can be seen that while at $x/R = 0.1$ the induction of the blade passing is clearly noticeable the asymmetry in respect to the center-line at $r/R = 0$ reduces already at $x/R = 0.3$. This is a very interesting observation that would permit to establish a clear limit up-to which the ALM or ASM would present uniqueness over the more widely used ADM. Of course complete symmetry is not obtained at $x/R = 0.3$, but future studies could go further beyond for determining the transition between ALM and ADM in the near wake.

As seen already in Figure (5.9) the difference in the induction close to the rotor is rather small also in the azimuthal profiles Figure (5.11) a part from a slight difference in the axial induction.

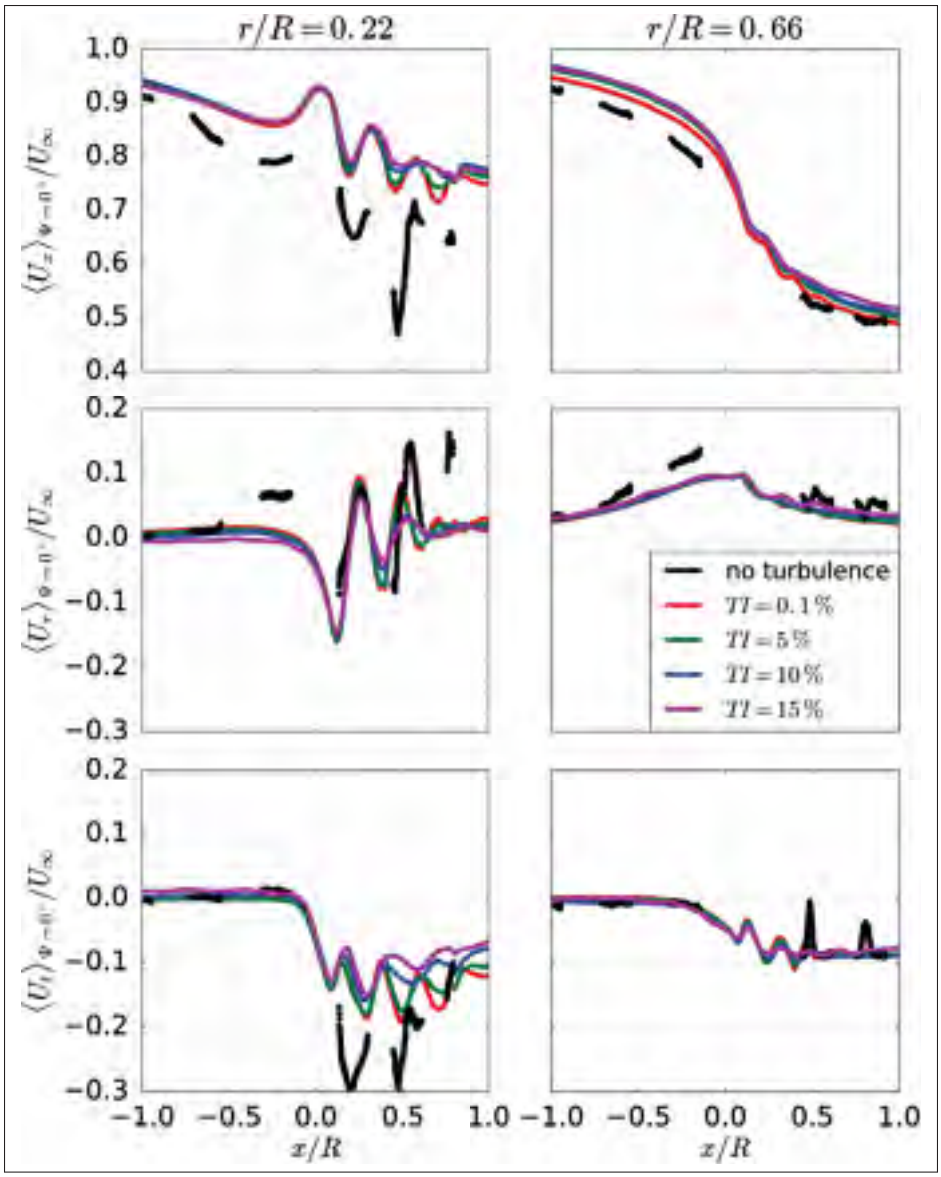

Figure 5.8 Axial profiles of phase-averaged velocity components $\langle U_i \rangle_{\Psi=0^\circ}$ at two different radial positions for different turbulence intensities.

In Figure (5.12) it can be seen how the strength of the vortical structures of the ambient fluid increases with higher turbulence intensity up-to the point for $T_{syn} = 15\,\%$ where its amplitude equals almost the one emitted by the rotor model.

When zooming in on the vortical structures emitted by one blade in Figure (5.13a), it can now be seen how the physical dissipation by the resolved and modelled ambient turbulence

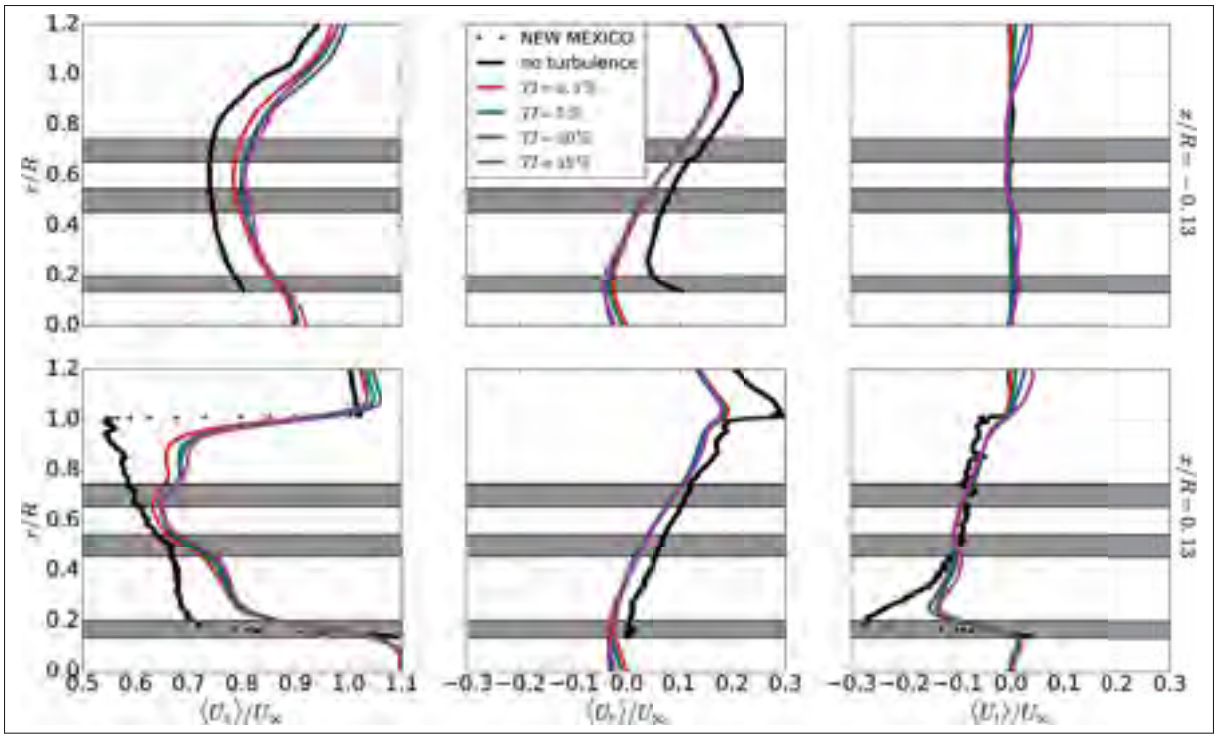

Figure 5.9 Radial profiles of mean velocity components $\langle U_i \rangle$ at two different axial positions for different turbulence intensities.

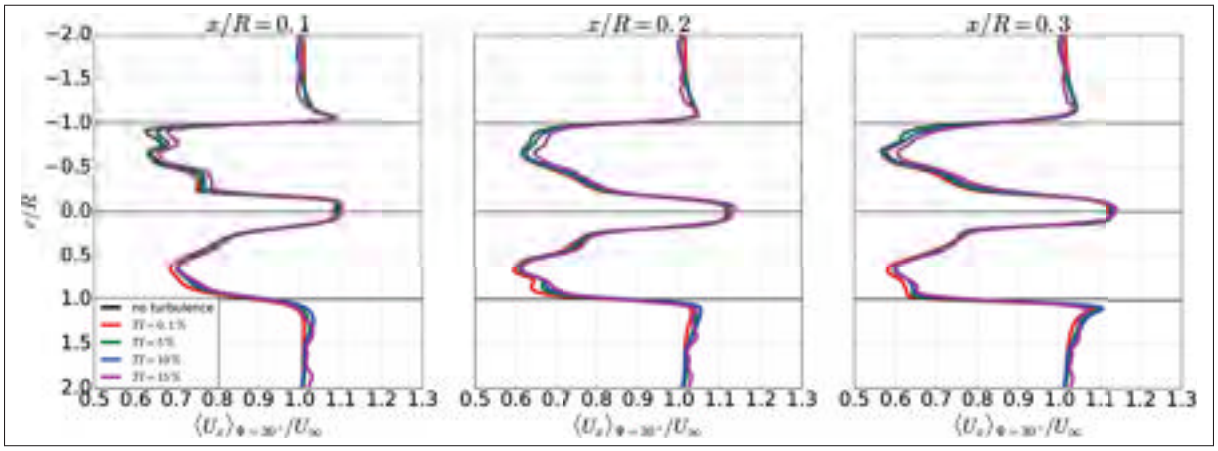

Figure 5.10 Longitudinal evolution of the radial profiles of phase-averaged axial velocity component $\langle U_x \rangle_{\Psi=30^\circ}$ downstream of the rotor for different turbulence intensities.

impacts the formation of the vortical structures. While for $TI_{syn} = 0.1\,\%$ even the beginning of a secondary vortex becomes visible around the tip vortex, the tip vortex smoothens out with

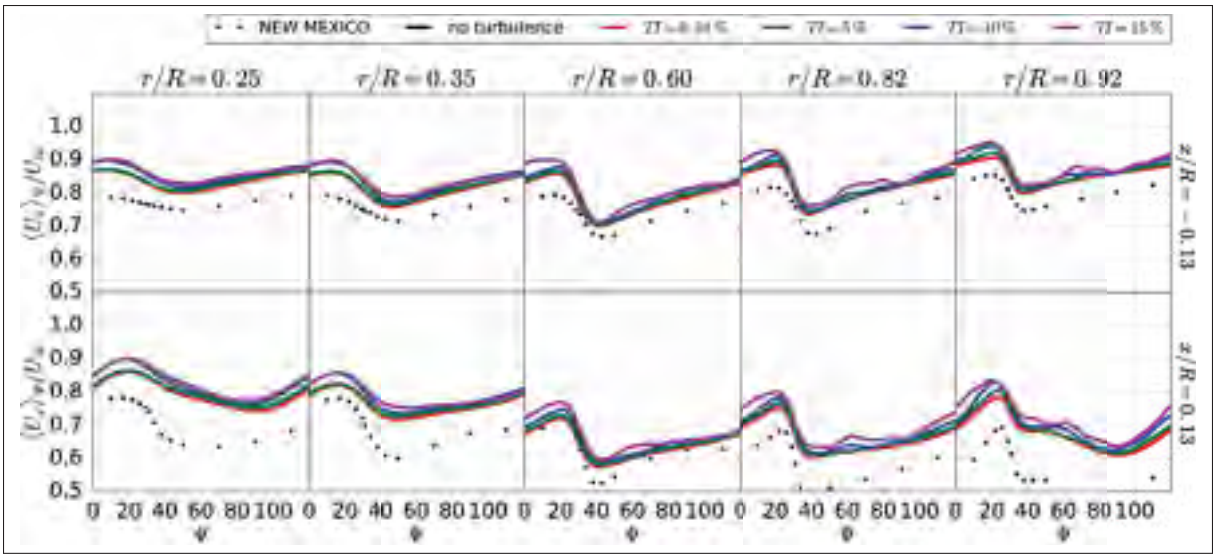

Figure 5.11 Azimuthal profiles of phase-averaged velocity components $\langle U_x \rangle_\Psi$ at $r/R = 0.92$ for different turbulence intensities.

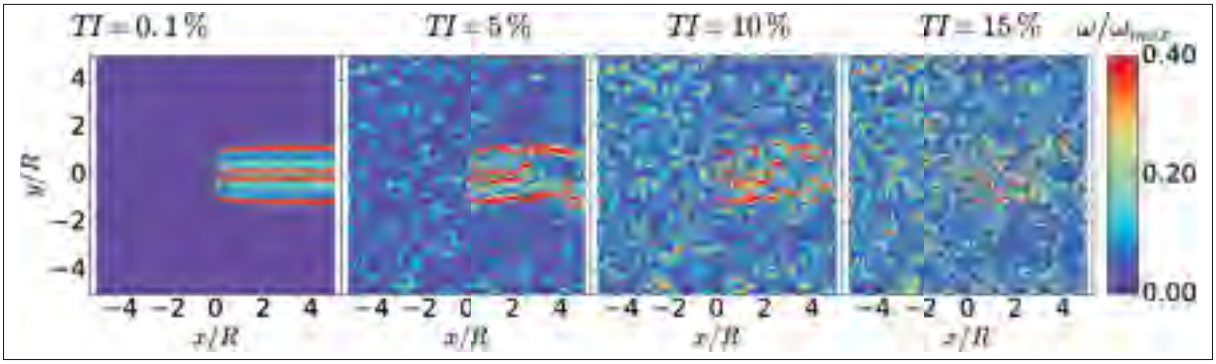

Figure 5.12 Vorticity fields for different turbulence intensities.

increasing turbulence intensity which becomes even clearer when looking solely on the tip vortex in Figure (5.13b).

In order to determine the properties of the first fully formed shed vortex, the vorticity distribution is shown in Figure (5.14).

In Figure (5.15) the impact of the rotor presence on the energy spectrum can be seen. The wavenumber κ_p relating to the frequency of a blade passage (three times rotor frequency) obtained by $\kappa_p = 2\pi 3 f / U_\infty$ shows a very distinct peak and its higher harmonics on the multiples

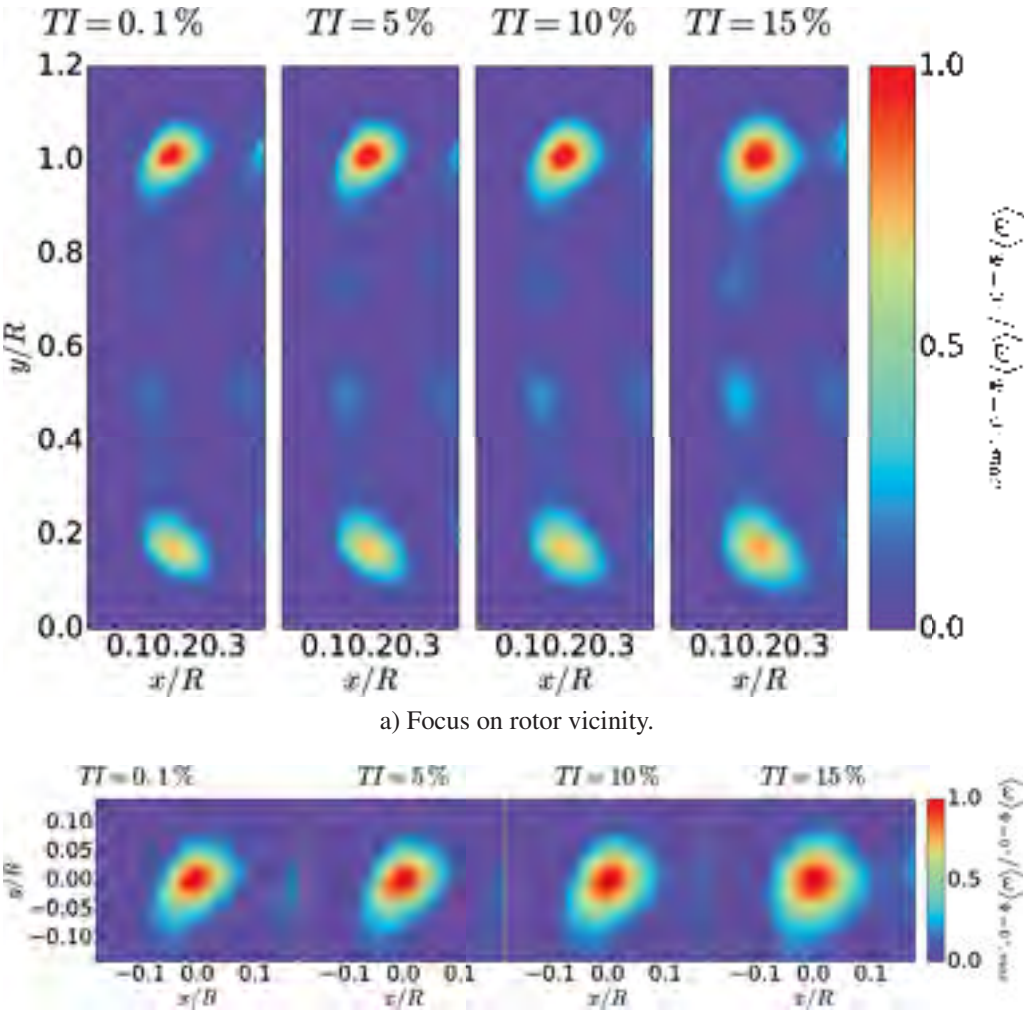

a) Focus on rotor vicinity.

b) Focus on first emitted tip vortex with reference frame centered on vortex center.

Figure 5.13 Phase-averaged normalized vorticity $\langle\omega\rangle_{\Psi=0^\circ}/\langle\omega\rangle_{\Psi=0^\circ,max}$ in sheared flow for different longitudinal turbulence intensities TI_x at hub position.

of κ_p. As the velocities of synthetic field are period with respect to their boundaries (Mann, 1998) the Bartlett method (Bartlett, 1948) can be used for generating the energy spectrum [1]. This contrasts with the usual assumption of $x/R = 2-4$ for the near wake limit as e.g. found in Sanderse *et al.* (2011), but it should be kept in mind that there is a strong dependence of the ambient turbulence intensity.

[1] See https://github.com/scipy/scipy/blob/v0.14.0/scipy/signal/spectral.py for implementation details of the method used in this work.

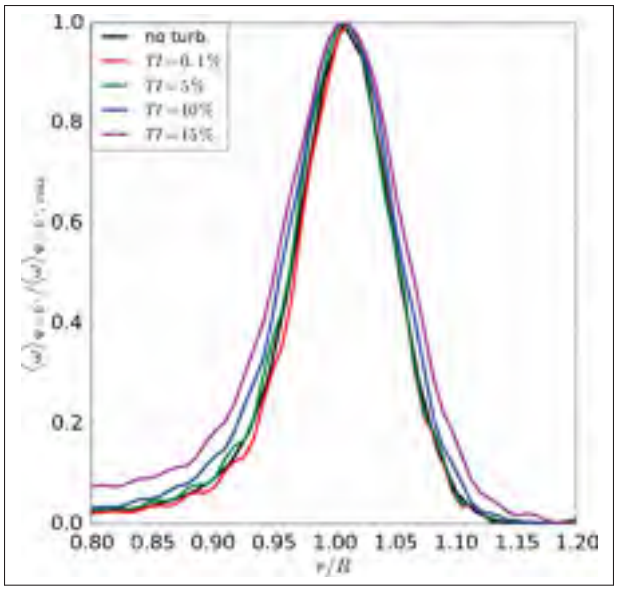

Figure 5.14 Radial profiles of normalized vorticity $\langle\omega\rangle_{\Psi=0^\circ}/\langle\omega\rangle_{\Psi=0^\circ,max}$.

It is interesting to notice the distinct peaks in the spectra occur at the wavenumber relating to the frequency of the blade passage and its harmonics. The harmonics are caused by the strong excitement by the blade passage and its interaction with the non-linear term in the NS equations. As the blade forces and hence the strength of the tip vortices are very comparable, the peaks are very similar among the different cases for $-0.4 \leq x/R \leq 0.2$. The higher the turbulent kinetic energy content stemming from the ambient flow the faster the peaks are dampened and blend into the ambient flow. For example there is almost no discernible effect by the blade at $x/R = 0.4$ for $TI_{syn} = 15\,\%$ while for $TI_{syn} = 0.1\,\%$ the velocity oscillations are still very noticeable. Although it is of lesser amplitude also the upstream region feels the distinct blades.

5.3 Conclusion

The boundary condition imposing the homogeneous isotropic turbulence obtained from the Mann algorithm works and parallelizes very well. Also the decay of the turbulence intensity in longitudinal direction is much less pronounced than in previous work. A significant part of the

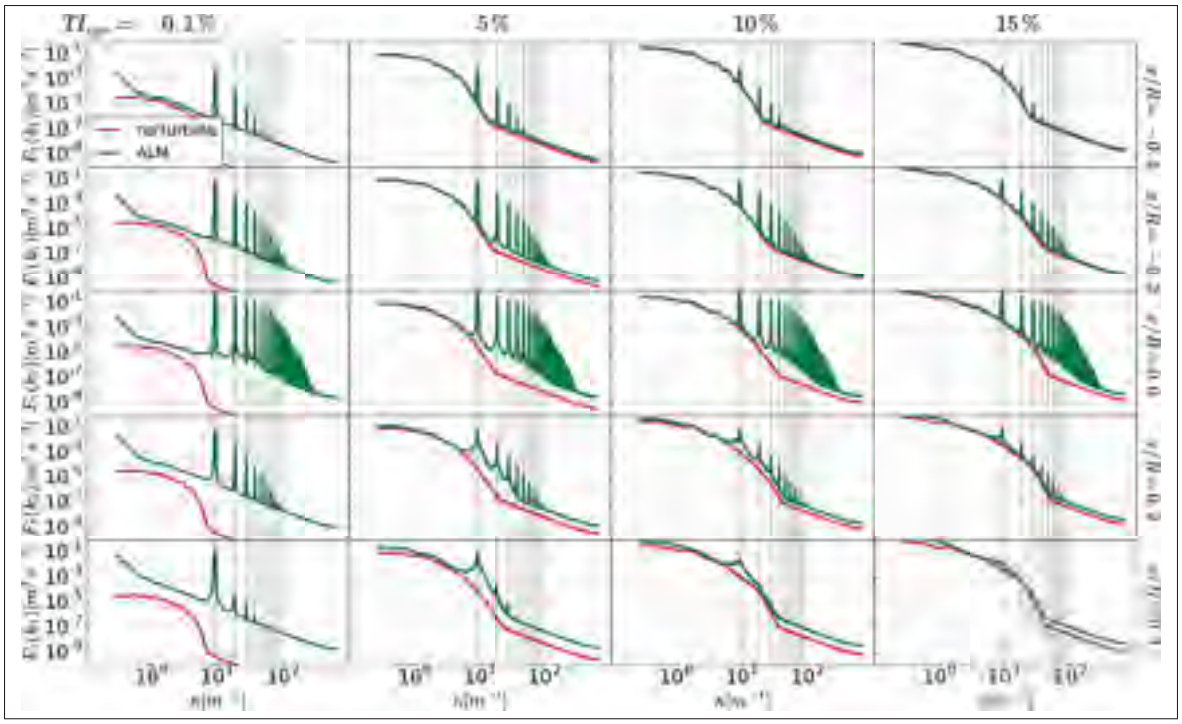

Figure 5.15 Impact of rotor presence on energy spectrum with wavenumber relating to 3 times rotor frequency and its higher harmonics indicated by dotted black lines.

difference between the resolved turbulence intensity and the imposed one from the synthetic field, resides within the sub-grid scales.

The wake does recover at a shorter distance for a higher turbulence intensity. It is very interesting to notice that the turbulent structures of the ambient flow eventually catch up with the amplitude of the structures emitted by the rotor. This is already noticeable in the instantaneous velocity fields but becomes even clearer when evaluating the spectra. When considering the velocity fluctuations in the downstream flow caused by the blade passages for determining the near wake, it can be observed that in this case for $TI_{syn} \geq 10\,\%$ the near wake already ends at $x/R = 0.4$. This is a remarkable observation which contrasts usual assumptions of the near wake reaching up-to $x/R = 2$–4 (Sanderse *et al.*, 2011).

CHAPTER 6

CASE 3: SHEAR LAYER TURBULENCE

While the imposed turbulent flow in Chapter 5 represents well the condition of a wind tunnel experiment, this chapter focuses on a sheared flow as experienced in practical wind turbine applications. First the numerical representation of the sheared flow without turbine is examined in Section 6.1 and then the results with an immersed rotor model are discussed in Section 6.2 followed by a conclusion in Section 6.3.

6.1 Evaluation of imposed turbulence

When looking at the global picture of how the numerical simulation represents the imposed shear flow in Figure (6.1), the flow ressembles to a shear layer turbulence. The horizontal planes in Figure (6.1a) bear close resemblance to the ones of the HIT in Figure (5.1) as this work tries to maintain a comparable mean velocity U_∞ and turbulence intensity $TI_{z/R=0}$ at the hub height. This again is done by adjusting the scaling parameter of the energy spectrum.

In Figure (6.2a) it can be seen that the axial velocity component U_x grows exponentially with height with a prescribed for neutral ABL $\alpha = 0.143$ by using the power law approximation for the vertical wind profile

$$U_x = U_{ref}\left(\frac{z}{z_{ref}}\right)^{\alpha} \tag{6.1}$$

with $U_{ref} = U_\infty = 15\,m/s$ at hub height $z/R = 0$. It can be seen that for $TI_{z/R=0} \geq 10\,\%$ the mean velocity profiles are less smooth which is due to high velocity fluctuations and the relatively short averaging time period of 40 rotor revolutions. As the oscillations remain reasonably close to the theoretical profile simulation time was not increased. When looking at the longitudinal evolution of the mean velocity $\langle U_x \rangle$ in Figure (6.2b) it can be seen that even for the higher turbulence intensity cases the variation at hub height is kept below $0.5\,\%$ and that there is a very slight offset of less than $0.1\,\%$ compared to the imposed value of $\langle U_{x,z/R=0} \rangle / U_\infty = 1$.

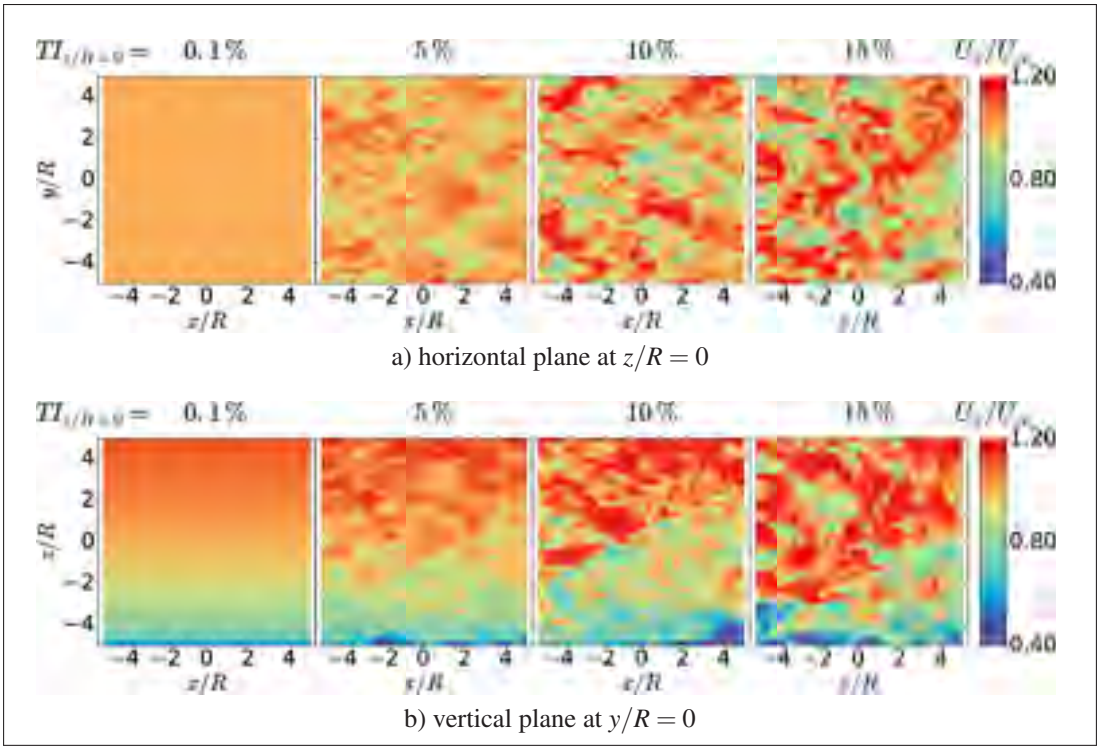

a) horizontal plane at $z/R = 0$

b) vertical plane at $y/R = 0$

Figure 6.1 Instantaneous axial velocity component U_x in sheared flow for different longitudinal turbulence intensities TI_x at hub position.

The vertical profiles of the longitudinal turbulence intensity in Figure (6.2c) at the rotor position show that the TI at hub height seems comparable to the ones of the HIT cases. Towards the ground the TI is steeply increasing as experienced in real sheared flow. When looking at the longitudinal decay of the turbulence intensity in Figure (6.2d) it can be seen that the rates are similar to the one in the HIT case. Also a very small fraction of the turbulence resides in the sub-grid scale.

In Figure (6.3) the same statistics can be seen for the case of $TI_{z/R=0} = 15\,\%$ at different heights. For the two planes close to the domain boundary at $y/R = -4$ and $y/R = 4$ the nature of the imposed turbulence can be seen more clearly. As the imposed turbulence is not fully divergence free (Muller, 2015) the numerical solver forces a divergence free solution and hence altering the imposed field.

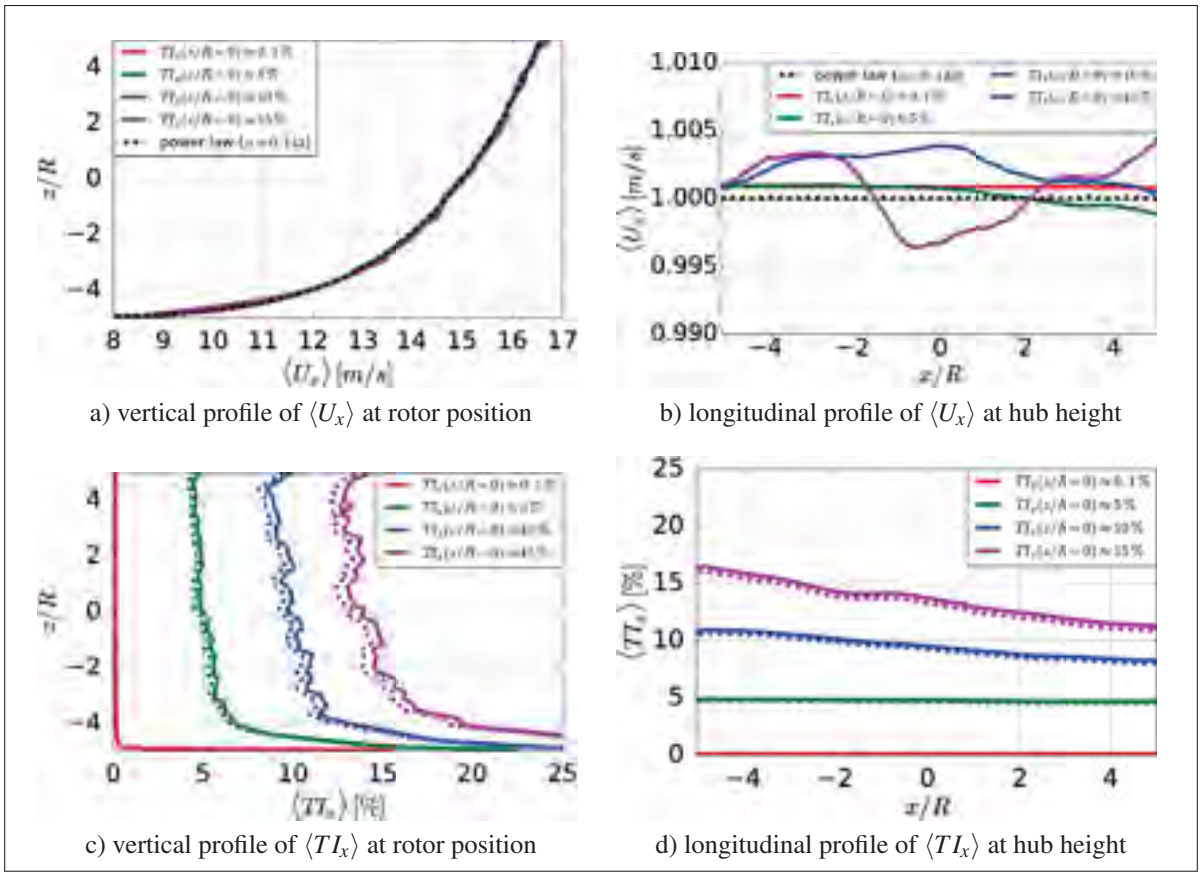

a) vertical profile of $\langle U_x \rangle$ at rotor position

b) longitudinal profile of $\langle U_x \rangle$ at hub height

c) vertical profile of $\langle TI_x \rangle$ at rotor position

d) longitudinal profile of $\langle TI_x \rangle$ at hub height

Figure 6.2 Longitudinal and vertical variation of time-average axial velocity component and longitudinal turbulence intensity for sheared flow with $\alpha = 0.143$ for different turbulence intensities at hub height ($z/R = 0$).

When taking a more quantitative look at the longitudinal evolution of the mean variables of the axial velocity component $\langle U_x \rangle$ and the axial turbulence intensity $\langle TI_x \rangle$ in Figure (6.3), it can be seen that the vertical mean velocity profile in Figure (6.3a) is very well maintained throughout the entire domain when comparing to the theoretical profile.

Another way of evaluating the longitudinal evolution of $\langle U_x \rangle$ as done in Muller (2015) is looking at how well the mean value is maintained at different heights z/R over the domain in Figure (6.3b). Again it shows a very good resemblance with the expected values.

When looking at the vertical profiles of $\langle TI_x \rangle$ in Figure (6.3c) at different axial positions, it can be seen that it experiences a steep increase towards the ground and decrease only slightly for

$z/R > 3$. Again when looking at the longitudinal evolution of $\langle TI_x \rangle$ in Figure (6.3d) it can be seen that the turbulence intensity at a certain height is well maintained throughout the domain with a slight increase towards the outlet of the computational domain. This is particularly pronounced for the $\langle TI_x \rangle$ close to the domain bottom at $z/R = -4$.

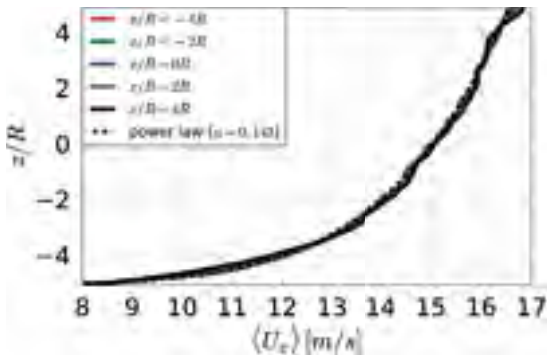

a) longitudinal profile of $\langle U_x \rangle$ at hub height

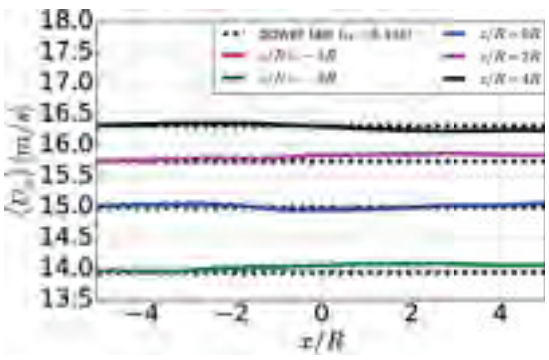

b) longitudinal profile of $\langle U_x \rangle$ at hub height

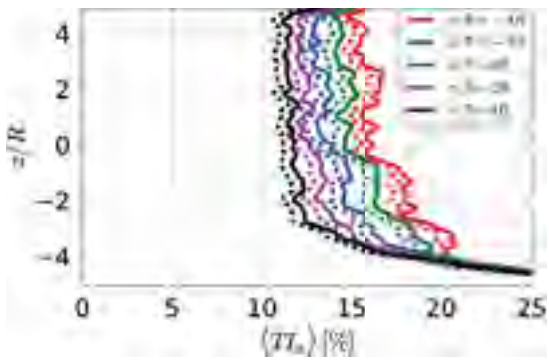

c) vertical profile of $\langle TI_x \rangle$ at rotor position

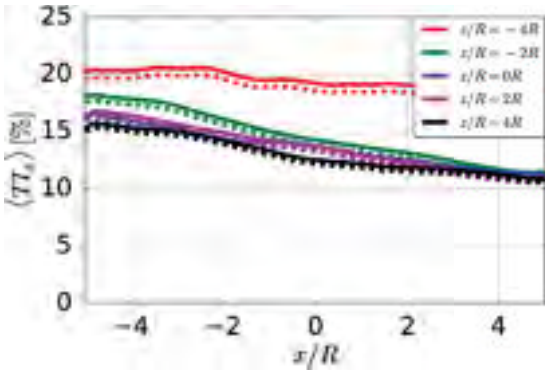

d) longitudinal profile of $\langle TI_x \rangle$ at different heights

Figure 6.3 Longitudinal and vertical variation of mean flow properties for sheared flow with $\alpha = 0.143$ at different positions for $TI_{z/R=0} = 15\,\%$.

The data presented in Figure (6.2) and Figure (6.3) were obtained by averaging sampled planes at different positions of the computational domain. When taking the vertical profile of the axial velocity component in Figure (6.3a) as an example, several planes were sampled at $x/R =$

$[-4,-2,0,2,4]$[1] and for each plane all vertical profiles over the whole lateral extent with $-5 \leq y/R \leq 5$ were averaged to obtain a single vertical profile representing an axial position.

6.2 Results

The instantaneous and mean velocity fields with an immersed rotor can be seen in Figure (6.4). The horizontal plane at hub height again seems to behave similar to the HIT cases in Figure (5.7a). When looking at the vertical planes in Figure (6.4b) the influence of the sheared flow can be seen by a higher velocity deficit in the wake on the lower half of the rotor.

When looking at the mean values in Figure (6.4c) wake recovery seems to happen faster than in the HIT cases. In Figure (6.4b) again it can be seen that the velocity deficit is more pronounced closer to the ground.

When comparing the axial profiles of the phase-averaged velocity in Figure (6.5) it can firstly be seen that there is little difference in the low turbulence cases between the sheared flow and the corresponding HIT case. With the higher turbulence intensity the velocity deficit lessens as wake recovery speeds up while the overall tendency is very well maintained throughout the refined zone of the mesh.

[1] Due to sampling problems with points coinciding with cell faces, on all sampling points an offset of $\Delta x/2$ was added.

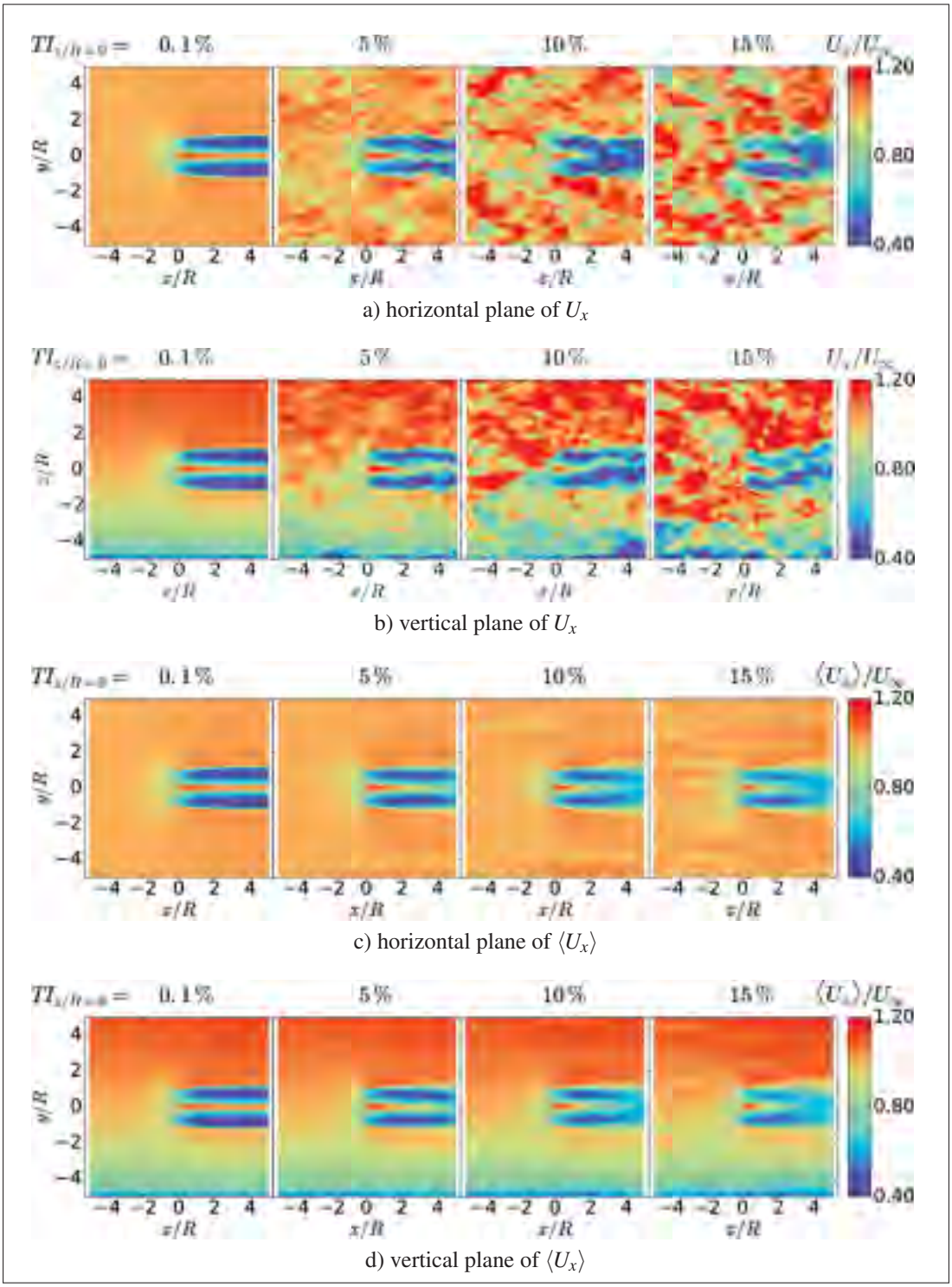

a) horizontal plane of U_x

b) vertical plane of U_x

c) horizontal plane of $\langle U_x \rangle$

d) vertical plane of $\langle U_x \rangle$

Figure 6.4 Instantaneous and mean axial velocity component U_x and $\langle U_x \rangle$ in sheared flow for different longitudinal turbulence intensities TI_x at hub position.

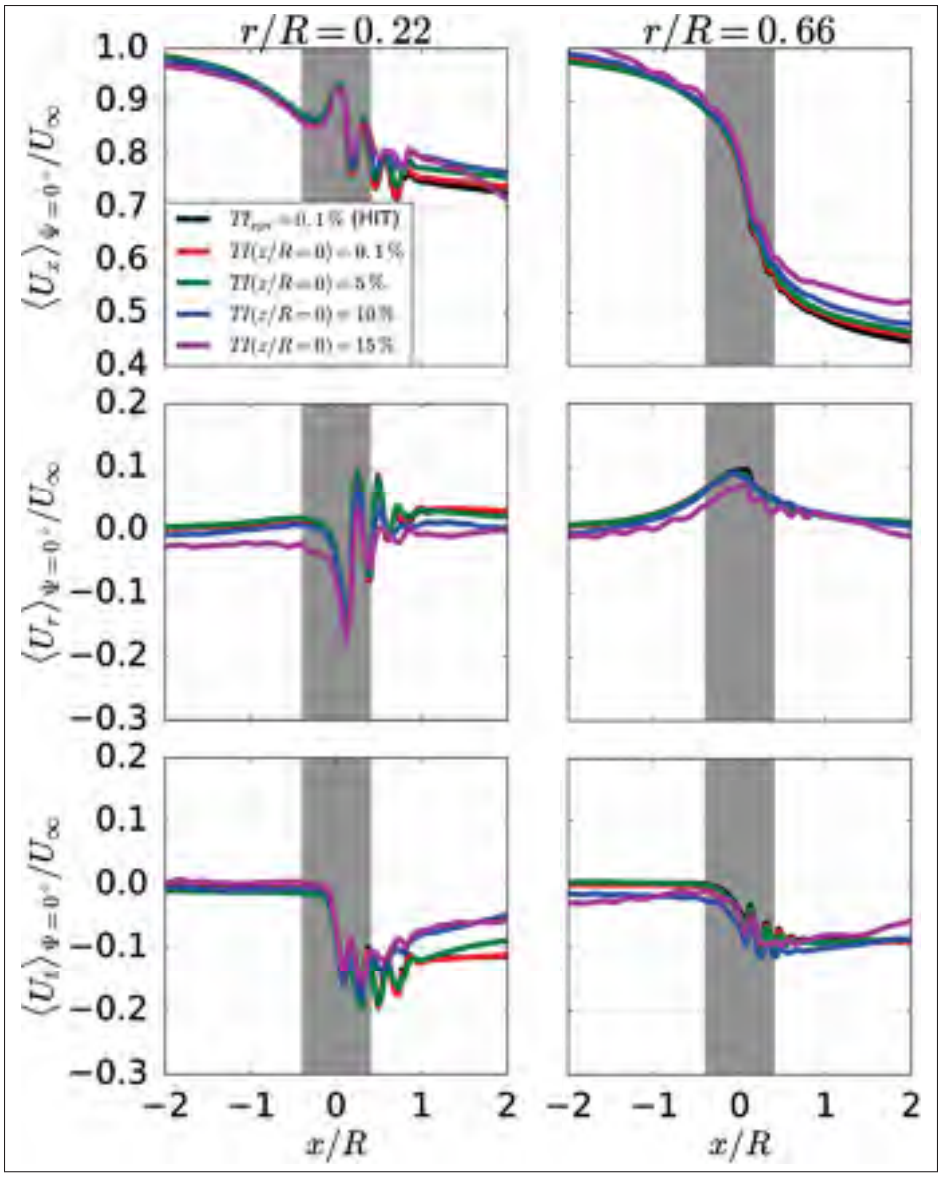

Figure 6.5 Axial profiles of $\langle U_i \rangle_{\Psi=0^\circ}$ at different radial positions. The refined rotor zone is indicated by the grey area.

The radial profiles in Figure (6.6) also exhibit the same trend for higher turbulence intensities.

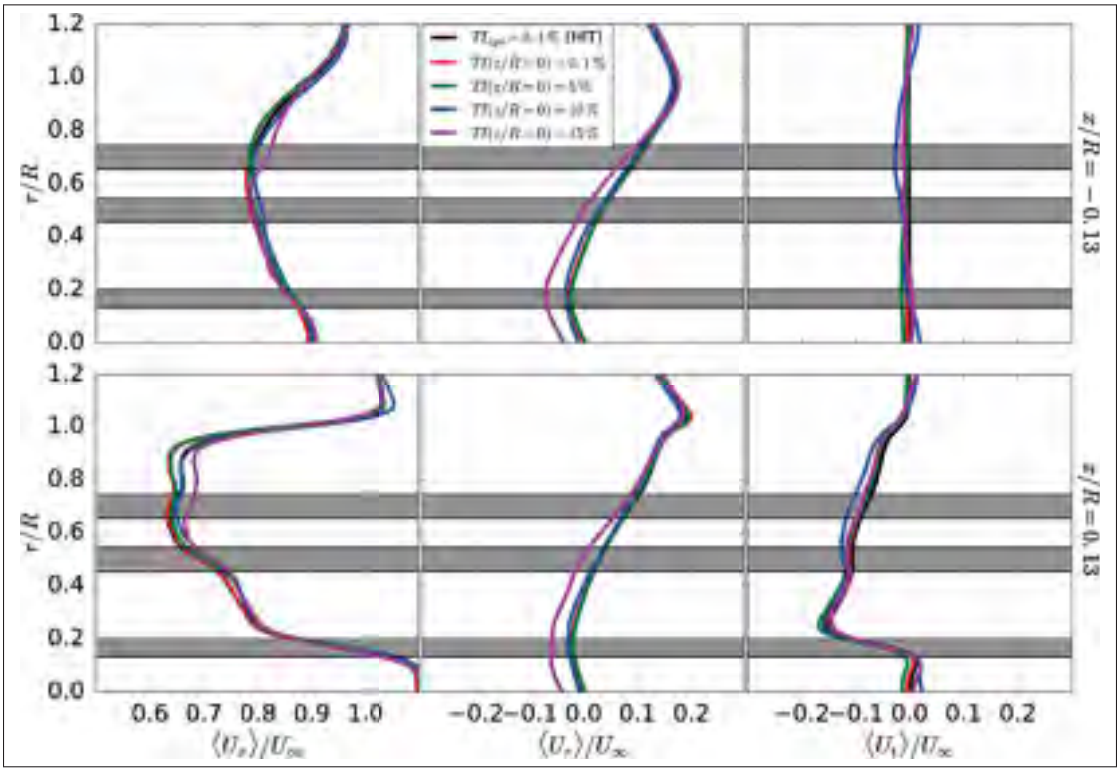

Figure 6.6 Radial profiles of $\langle U_i \rangle$ at different axial positions.

Apart from the high turbulence case, the axial induction shown in the azimuthal variation of the phase-averaged axial velocity component in Figure (6.7) there seems to be little difference between the cases.

When looking at the instantaneous normalized vorticity in Figure (6.8) it can be seen that while the vortical structures emitted by the rotor are prevalent for low turbulence intensity cases, they seem to get even for $TI_{x,z/R=0} \geq 10\%$. Hence, the turbulent structures of the ambient flow become as significant as the ones emitted from the wind turbine. This is of particular interest for estimating the range up-to which the effects of the distinct blades can be felt which serves

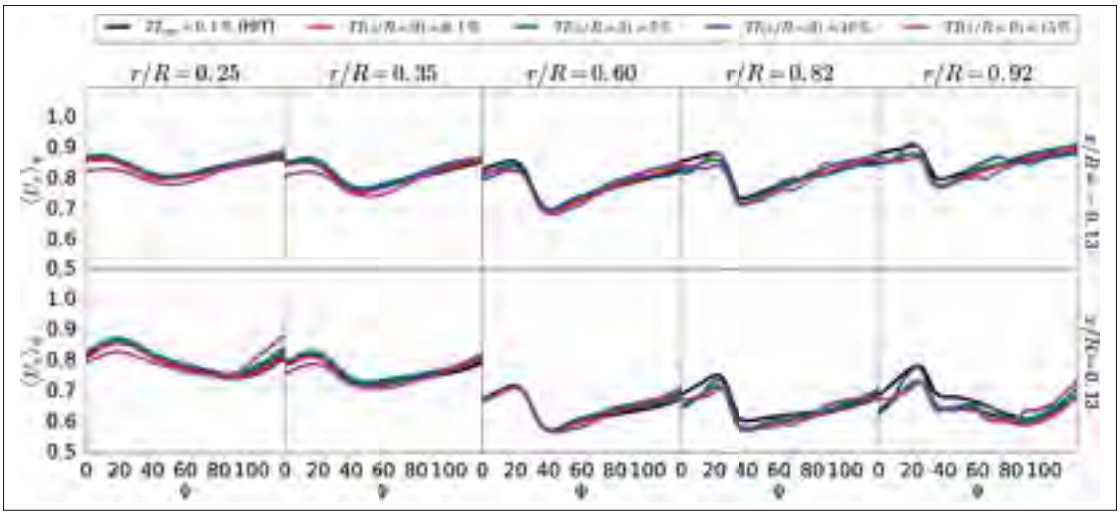

Figure 6.7 Azimuthal profiles of $\langle U_x \rangle_\Psi$ at different radial positions.

often as a measurement for determining the near wake. In the vertical plane in Figure (6.8b) it can be seen that there is an increase in the vorticity magnitude towards the ground.

When focusing on the vortical structures emitted by the blade in Figure (6.9a), again it can be seen that there are two very distinct vortices at the tip and the root, but also at the transition at the edges of the mid section airfoil. The dissipation due to the shear layer turbulence seems to be much more important than for the HIT cases, as the tip vortices increase much in extent for rising turbulence intensitieswhich can be seen when looking at Figure (6.9b). In this graphic a pertubation can be seen at the bottom of the computational domain, e.g. for $T_{z/R=0} = 0.1\,\%$ at $y/R = -4$. This is probably due to the nature of the way the synthetic turbulence is imposed.

When looking quantitatively on the vortex radii in Figure (6.10) this observation can be confirmed.

Another very interesting aspect is the question of how far downstream the ALM is noticable which can be investigated by looking at the spectra in Figure (6.11). Again the distinct peaks in the spectra occur at the wavenumber relating to the frequency of the blade passage and its harmonics. As the blade forces and hence the strength of the tip vortices are very comparable, the

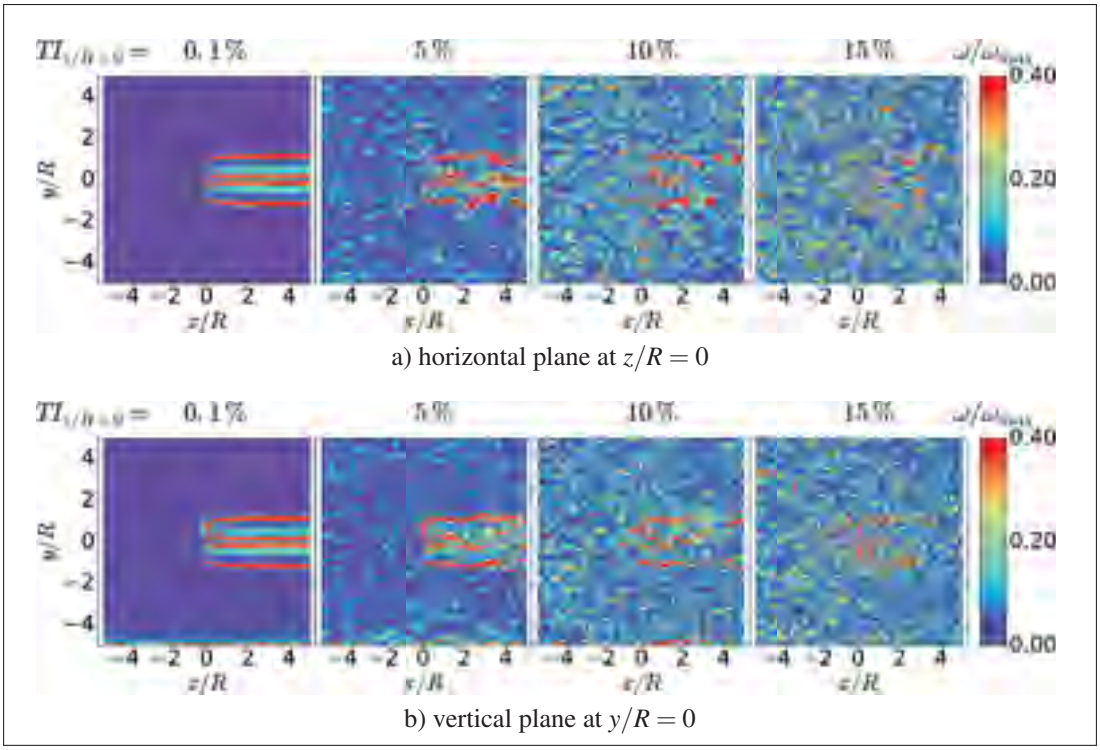

a) horizontal plane at $z/R = 0$

b) vertical plane at $y/R = 0$

Figure 6.8 Instantaneous normalized vorticity ω/ω_{max} in sheared flow for different longitudinal turbulence intensities TI_x at hub position.

peaks are very similar among the different cases for $-0.4 \leq x/R \leq 0.2$. Due to the dissipation caused by the ambient turbulence these peaks dampen at a different pace as seen at $x/R = 0.4$.

While before and at the rotor position for $-0.4 \leq x/R \leq 0$ the peaks remain very distinct, vortical structures by the ambient fluid and emitted by the blade cause the injected peaks to dampen and distributes energy to adjacent wavenumbers as seen for $x/R \geq 0.2$. Depending on the level of the ambient turbulence the peak gets attenuated up-to a point where it blends almost completely in with ambient turbulence as seen for $TI_{x,z/R=0} = 15\,\%$ at $x/R = 0.4$. This relates to the observation made earlier when looking at Figure (6.4) and Figure (6.8) where the ambient structures are almost as important as the structures emitted by the blade.

This is particularly interesting for examining the reach of the here used rotor model and the distinct presence of the separate blade forces. It seems that for a realistic case with a turbulent

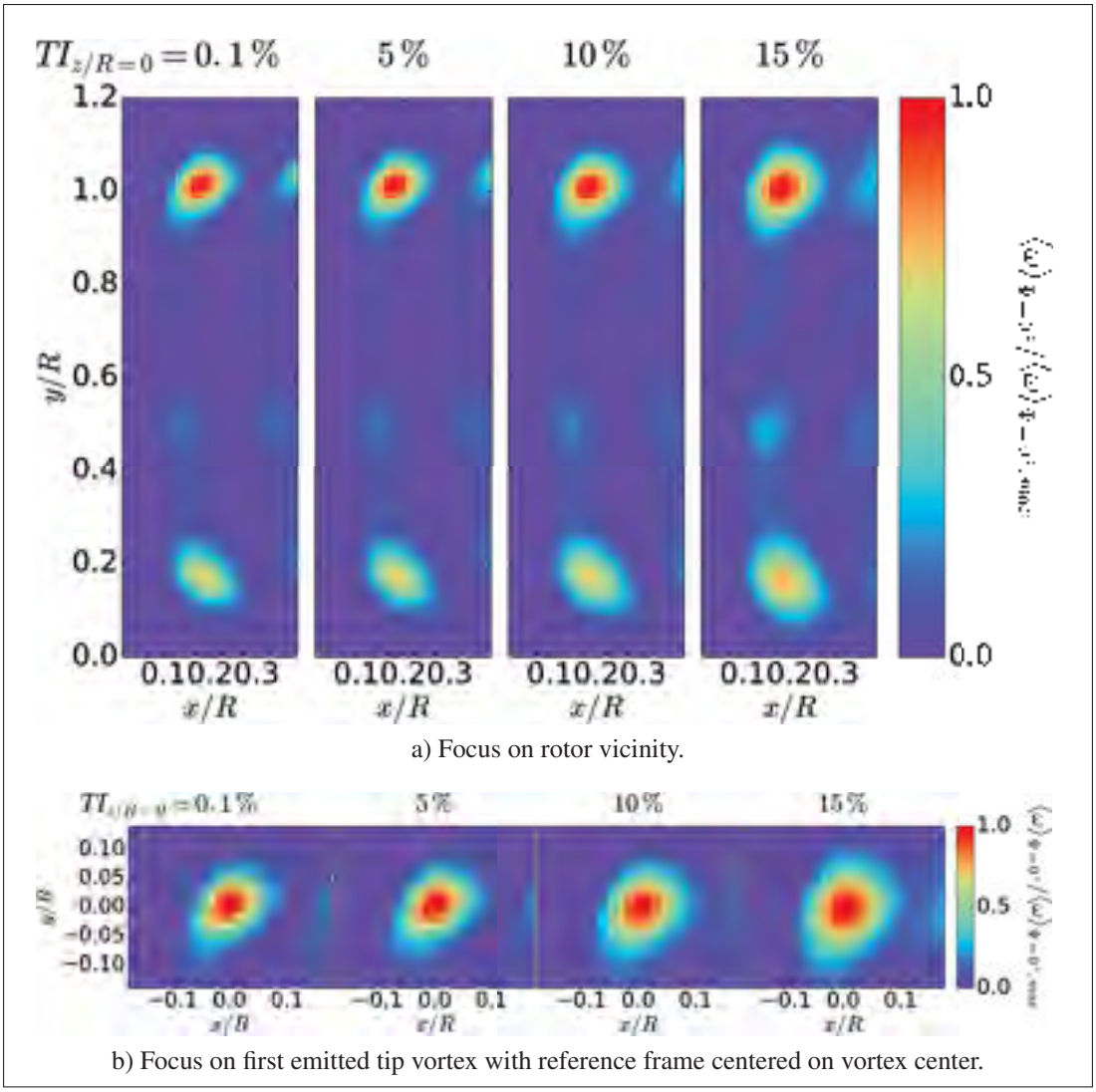

a) Focus on rotor vicinity.

b) Focus on first emitted tip vortex with reference frame centered on vortex center.

Figure 6.9 Phase-averaged normalized vorticity $\langle\omega\rangle_{\Psi=0^\circ}/\langle\omega\rangle_{\Psi=0^\circ,max}$ in sheared flow for different longitudinal turbulence intensities TI_x at hub position.

shear flow and a turbulence intensity of $TI_{x,z/R=0} \geq 10\,\%$ the velocity fluctuations at $x/R = 0.4$ already seem to have only a weak relation to the injected turbulence by the rotor but a much stronger one to the ambient turbulence.

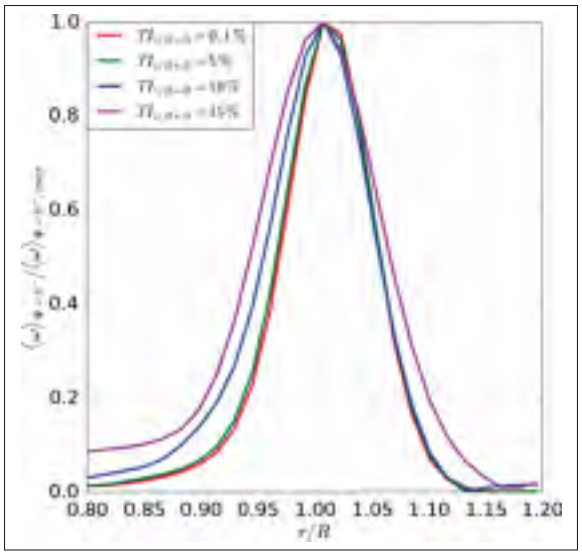

Figure 6.10 Radial distribution of phase-averaged normalized vorticity $\langle\omega\rangle_{\Psi=0^\circ}/\langle\omega\rangle_{\Psi=0^\circ,max}$.

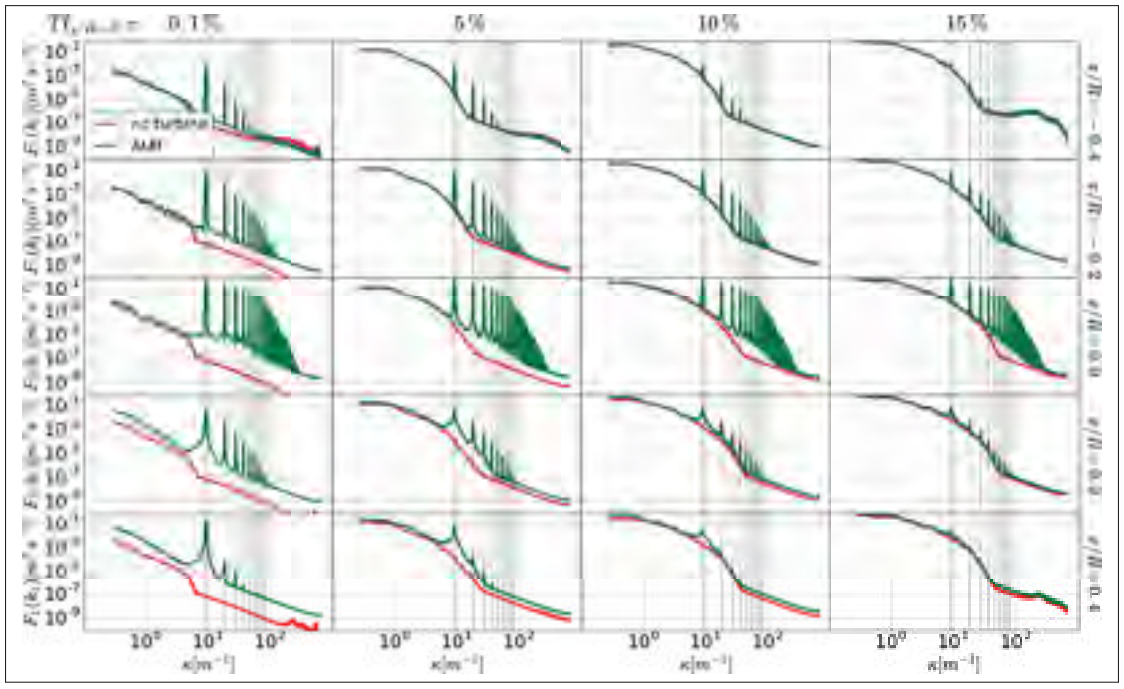

Figure 6.11 Spectra of different axial positions at hub height z/R.

6.3 Conclusion

The results obtained by using the library developed by Muller (2015) are encouraging for simulating a shear layer flow in a LES with a synthetic turbulence. As seen for the HIT cases there is a decay in the turbulence intensity in longitudinal direction, but remains well below the rate as experienced by e.g. Olivares Espinosa (2017). It was possible to maintain a similar mean velocity and longitudinal turbulence intensity at the hub height in the HIT cases and the cases of the sheared flow.

Although flow properties were maintained at a similar level, the sheared flow has a clear impact on the power extraction and also on vortex properties of the structures emitted by the blade. A very interesting observation is the fact that for higher turbulence intensities the effects of the distinct blades using the ALM seems to vanish at relatively short downstream distances when compared to literature (Sanderse *et al.*, 2011). This poses the question of the usability of the ALM when arguing for its capabilities of representing the transient behaviour and its impact on downstream turbines.

CONCLUSION AND RECOMMENDATIONS

The main objective of this work was to examine the near wake results of an enhanced actuator line method immersed in different ambient flows. This was achieved by firstly validating the implementation against another popular framework for CFD in wind energy research, EllipSys3D. The numerical results of both frameworks are very similar and agree the results from the MEXICO and NEW MEXICO experiments. This establishes more trust in both of these two frameworks. Interestingly while both methods for velocity sampling used the actuator point of the previous timestep, their interpolation method to obtain the velocity differed and yet almost no difference was found in the result. The reliance on the 2D airfoil coefficients delivered good results without prior modification or dynamic stall models, except for the high velocity case. Together with the fact that the velocity for the third case $U_\infty = 24\,m/s$ represents a typical cut-out speed for most wind turbines, this case would be very rarely attained. Hence, the available 2D airfoil data covers most of the real life cases.

By adjusting the distribution with ε based on the global torque the optimal parameter could be obtained for this case and several grid resolutions. It was found that the distribution width scales in a non-linear fashion with the grid resolution. In order to obtain an accurate representation of the tip vortices it would necessitate a grid resolution of $N = D/\Delta x \geq 1024$ which would lead to a mesh of more than one billion cells. Following the trend of the distribution it would be around $\varepsilon/\Delta x = 4-5$ at this resolution which is in agreement with recent theoretical findings by Martínez-Tossas *et al.* (2016) and also fully resolved rotor simulations done by Carrión *et al.* (2015). Of course at this point the mesh size and the associated computational costs would exceed by far the resources of Compute Canada and its usefulness could be questioned as well as fully resolved rotor simulations on a non-uniform mesh could be conducted at much lower resolutions and deliver more accurate results.

The boundary condition implemented to impose the homogeneous isotropic turbulence generated by the algorithm of Mann (1998) by the application of Gilling (2009) works as expected and deliveres moderate decay rates of turbulent kinetic energy. The computational overhead is negligible and it parallelizes very well. A very interesting phenomenon is the very low decay of turbulence intensity in longitudinal direction compared to previous work. Several aspects contribute to this behaviour, whereas the resolution of the computational domain versus the resolution of the synthetic domain plays the most important role. The Nyquist criterion was respected in this work whereas e.g. Olivares Espinosa (2017) had a ratio $\Delta x/\delta x \leq 1$ resulting in a very strong decay of turbulence intensity.

The library of Muller (2015) delivers good results for imposing a shear layer turbulence on a CFD simulation. As the Nyquist criterion was also respected in this case, the decay of the turbulence intensity remains relatively low. The different turbulence intensities have little influence on the extracted torque for both kinds of turbulent flow, as the mean velocity determines the amount of energy passing through the wind turbine. But they have an important effect on the rate of the wake recovery.

It is very interesting as well to see the results obtained from the energy spectra in the cases of the homogeneous isotropic turbulence and the shear layer turbulence. The extent of the near wake is often set between $2-6R$ downstream ((Vermeer *et al.*, 2003), (Sanderse *et al.*, 2011)) which might be true for a flow exhibiting a low turbulence intensity, but as found in this work for the turbulence cases with $TI_{x,r/R=0} \approx 15\,\%$ at hub height for $x/R = 0.4$ the distinct blade effects are not longer discernible. This is particular interesting as a turbulence intensity of $15\,\%$ at hub height is still considered to be low turbulence intensity according to IEC 61400 and many real sites exhibit much higher turbulence intensities. Hence the limit of the near wake would be even below $x/R = 0.4$. Together with the observation that the velocity deficit is underestimated in the ultimate rotor vicinity and good agreement with the experiment was

only found for $x/R > 5$, some doubts may be cast on the usability of the ALM for accurately describing the near wake. For the near wake properties the most accurate and less expensive solution would probably be a fully resolved rotor simulation with an appropriate model for representing the boundary layer on the blades instead of relying on airfoil coefficients. For far wakes it seems that an ADM would be much better suited as it is much less expensive and, as found in this work, the effects of the distinct blades are not noticable very far downstream.

Future work

Based on the presented methodology and its results, several possibilities for future work arise:

- Investigate the effect of the modification 2D airfoil data and/or application of dynamic stall modelling for the ALM on extreme cases such as the high velocity case from the (NEW) MEXICO experiment.
- Thorough comparison of the near wake results of a fully resolved rotor simulation with a well resolved ALM.
- Examine at which point downstream the radial profile of the axial velocity component, hence axial induction, becomes symmetric with respect to the center line. This could be done for different turbulent flows and different turbulence intensities. Together with the observations made with the energy spectra a more complete picture of the usability of the ALM could emerge. experiment.

APPENDIX I

PROPERTIES OF THE MEXICO ROTOR

1. Geometrical definition MEXICO blade

Table A-1 Geometrical definition of the blade used in MEXICO.

r $[m]$	c $[m]$	φ_T $[^\circ]$	Airfoil
0.210	0.195	0.000	Cylinder
0.230	0.195	0.000	Cylinder
0.235	0.090	0.000	Cylinder
0.300	0.090	0.000	Cylinder
0.375	0.165	8.200	transition
0.450	0.240	16.400	DU91-W2-250
0.675	0.207	12.100	DU91-W2-250
0.900	0.178	8.300	DU91-W2-250
1.025	0.166	7.100	DU91-W2-250
1.125	0.158	6.100	transition
1.225	0.150	5.500	RISØA1-21
1.350	0.142	4.800	RISØA1-21
1.475	0.134	4.000	RISØA1-21
1.575	0.129	3.700	transition
1.675	0.123	3.200	NACA64-418
1.800	0.116	2.600	NACA64-418
2.025	0.102	1.500	NACA64-418
2.165	0.092	0.700	NACA64-418
2.193	0.082	0.469	NACA64-418
2.222	0.056	0.231	NACA64-418
2.250	0.011	0.000	NACA64-418

2. Airfoil coefficients for the MEXICO blade

Table A-2 Coefficients for used airfoils of the MEXICO experiment.

DU91			RISØ			NACA		
α	c_L	c_D	α	c_L	c_D	α	c_L	c_D
-180	-0.3905	0.0263	-180	-0.3905	0.0263	-180	-0.3905	0.0263
-175	0.0062	0.0314	-175	0.0062	0.0314	-175	0.0062	0.0314
-170	0.4730	0.1072	-170	0.4730	0.1072	-170	0.4730	0.1072
-165	0.5280	0.2469	-165	0.5280	0.2469	-165	0.5280	0.2469
-160	0.3880	0.2854	-160	0.3880	0.2854	-160	0.3880	0.2854
-155	0.5191	0.4021	-155	0.5191	0.4021	-155	0.5191	0.4021
-150	0.6700	0.5768	-150	0.6700	0.5768	-150	0.6700	0.5768
-145	0.7551	0.7483	-145	0.7551	0.7483	-145	0.7551	0.7483
-140	0.8022	0.9219	-140	0.8022	0.9219	-140	0.8022	0.9219
-135	0.8082	1.0884	-135	0.8082	1.0884	-135	0.8082	1.0884
-130	0.7809	1.2432	-130	0.7809	1.2432	-130	0.7809	1.2432
-125	0.7231	1.3820	-125	0.7231	1.3820	-125	0.7231	1.3820
-120	0.6422	1.5039	-120	0.6422	1.5039	-120	0.6422	1.5039
-115	0.5413	1.6063	-115	0.5413	1.6063	-115	0.5413	1.6063
-110	0.4261	1.6903	-110	0.4261	1.6903	-110	0.4261	1.6903
-105	0.2995	1.7541	-105	0.2995	1.7541	-105	0.2995	1.7541
-100	0.1657	1.7994	-100	0.1657	1.7994	-100	0.1657	1.7994
-95	0.0270	1.8249	-95	0.0270	1.8249	-95	0.0270	1.8249
-90	-0.1135	1.8323	-90	-0.1135	1.8323	-90	-0.1135	1.8323
-85	-0.2532	1.8203	-85	-0.2532	1.8203	-85	-0.2532	1.8203
-80	-0.3897	1.7903	-80	-0.3897	1.7903	-80	-0.3897	1.7903
-75	-0.5199	1.7409	-75	-0.5199	1.7409	-75	-0.5199	1.7409
-70	-0.6412	1.6737	-70	-0.6412	1.6737	-70	-0.6412	1.6737
-65	-0.7496	1.5872	-65	-0.7496	1.5872	-65	-0.7496	1.5872
-60	-0.8421	1.4831	-60	-0.8421	1.4831	-60	-0.8421	1.4831
-55	-0.9129	1.3607	-55	-0.9129	1.3607	-55	-0.9129	1.3607
-50	-0.9588	1.2225	-50	-0.9588	1.2225	-50	-0.9588	1.2225

DU91 (cont.)			RISØ(cont.)			NACA (cont.)		
α	c_L	c_D	α	c_L	c_D	α	c_L	c_D
-45	-0.9718	1.0694	-45	-0.9718	1.0694	-45	-0.9718	1.0694
-40	-0.9492	0.9055	-40	-0.9492	0.9055	-40	-0.9492	0.9055
-35	-0.8823	0.7349	-35	-0.8823	0.7349	-35	-0.8823	0.7349
-30	-0.8851	0.4396	-30	-0.8300	0.5500	-30	-0.7534	0.5873
-25	-1.0238	0.2030	-25	-0.7650	0.4250	-25	-0.5972	0.4205
-20	-0.9552	0.1212	-20	-0.7000	0.3000	-20	-0.5089	0.2917
-15	-0.7264	0.0803	-15	-0.6500	0.1650	-15	-0.7997	0.0727
-10	-0.4823	0.0567	-10	-0.6000	0.0300	-10	-0.7048	0.0244
-9	-0.4337	0.0494	-9	-0.5235	0.0267	-9	-0.6501	0.0207
-8	-0.3748	0.0406	-8	-0.4470	0.0235	-8	-0.5769	0.0179
-7	-0.3166	0.0359	-7	-0.3705	0.0202	-7	-0.4982	0.0161
-6	-0.2546	0.0306	-6	-0.2940	0.0170	-6	-0.4039	0.0150
-5	-0.1924	0.0262	-5	-0.2060	0.0143	-5	-0.2998	0.0137
-4	-0.1319	0.0238	-4	-0.0911	0.0132	-4	-0.1878	0.0132
-3	-0.0612	0.0214	-3	0.0273	0.0122	-3	-0.0778	0.0132
-2	0.0249	0.0186	-2	0.1375	0.0192	-2	0.0330	0.0132
-1	0.1259	0.0167	-1	0.2473	0.0123	-1	0.1429	0.0132
0	0.2471	0.0155	0	0.3570	0.0101	0	0.2520	0.0134
1	0.3734	0.0196	1	0.4673	0.0101	1	0.3620	0.0135
2	0.4942	0.0194	2	0.5774	0.0103	2	0.4700	0.0140
3	0.6096	0.0197	3	0.6869	0.0107	3	0.5758	0.0144
4	0.7132	0.0202	4	0.7968	0.0109	4	0.6789	0.0150
5	0.8110	0.0213	5	0.9075	0.0113	5	0.7780	0.0157
6	0.8991	0.0227	6	1.0170	0.0119	6	0.8703	0.0168
7	0.9691	0.0256	7	1.1272	0.0130	7	0.9524	0.0185
8	1.0217	0.0316	8	1.2261	0.0149	8	1.0193	0.0212
9	1.0617	0.0389	9	1.3011	0.0177	9	1.0691	0.0256
10	1.0748	0.0412	10	1.3405	0.0255	10	1.1069	0.0310
11	1.1108	0.0533	11	1.3102	0.0524	11	1.1407	0.0416
12	1.1601	0.0687	12	1.2434	0.0886	12	1.1516	0.0523

DU91 (cont.)			RISØ(cont.)			NACA (cont.)		
α	c_L	c_D	α	c_L	c_D	α	c_L	c_D
13	1.1756	0.0772	13	1.1791	0.1094	13	1.1680	0.0650
14	1.1878	0.0839	14	1.1113	0.1172	14	1.1824	0.0764
15	1.1992	0.0902	15	1.0926	0.1313	15	1.1859	0.0903
16	1.1992	0.1003	16	1.0892	0.1452	16	1.1860	0.1054
17	1.1878	0.1136	17	1.0827	0.1563	17	1.1812	0.1198
18	1.1804	0.1330	18	1.0740	0.1662	18	1.1616	0.1353
19	1.1707	0.1508	19	1.0670	0.1758	19	1.1346	0.1533
20	1.1802	0.1677	20	1.0661	0.1858	20	1.1196	0.1747
21	1.1923	0.1854	21	1.0600	0.1964	21	1.0967	0.1982
22	1.2117	0.2061	22	1.0634	0.2110	22	0.8090	0.3730
23	1.2203	0.2277	23	1.0599	0.2244	23	0.7755	0.3612
24	1.2193	0.2517	24	1.0556	0.2404	24	0.7901	0.4023
25	1.0582	0.3615	25	1.0496	0.2579	25	0.8370	0.4423
26	0.8838	0.4823	26	1.0422	0.2768	26	0.8838	0.4823
27	0.9216	0.5215	27	1.0399	0.3040	27	0.9216	0.5215
28	0.9594	0.5608	28	1.0399	0.3395	28	0.9594	0.5608
29	0.9894	0.5993	29	1.0031	0.3814	29	0.9894	0.5993
30	1.0193	0.6377	30	0.9633	0.4117	30	1.0193	0.6377
35	1.1118	0.8214	35	0.7739	0.4995	35	1.1118	0.8214
40	1.1452	0.9936	40	0.7000	0.7000	40	1.1452	0.9936
45	1.1326	1.1536	45	0.8250	0.8500	45	1.1326	1.1536
50	1.0861	1.3014	50	1.0861	1.3014	50	1.0861	1.3014
55	1.0126	1.4361	55	1.0126	1.4361	55	1.0126	1.4361
60	0.9188	1.5573	60	0.9188	1.5573	60	0.9188	1.5573
65	0.8073	1.6624	65	0.8073	1.6624	65	0.8073	1.6624
70	0.6828	1.7513	70	0.6828	1.7513	70	0.6828	1.7513
75	0.5476	1.8211	75	0.5476	1.8211	75	0.5476	1.8211
80	0.4053	1.8723	80	0.4053	1.8723	80	0.4053	1.8723
85	0.2576	1.9028	85	0.2576	1.9028	85	0.2576	1.9028
90	0.1063	1.9138	90	0.1063	1.9138	90	0.1063	1.9138

DU91 (cont.)			RISØ(cont.)			NACA (cont.)		
α	c_L	c_D	α	c_L	c_D	α	c_L	c_D
95	-0.0499	1.9034	95	-0.0499	1.9034	95	-0.0499	1.9034
100	-0.2034	1.8736	100	-0.2034	1.8736	100	-0.2034	1.8736
105	-0.3518	1.8237	105	-0.3518	1.8237	105	-0.3518	1.8237
110	-0.4927	1.7566	110	-0.4927	1.7566	110	-0.4927	1.7566
115	-0.6229	1.6725	115	-0.6229	1.6725	115	-0.6229	1.6725
120	-0.7408	1.5741	120	-0.7408	1.5741	120	-0.7408	1.5741
125	-0.8430	1.4613	125	-0.8430	1.4613	125	-0.8430	1.4613
130	-0.9271	1.3354	130	-0.9271	1.3354	130	-0.9271	1.3354
135	-0.9865	1.1941	135	-0.9865	1.1941	135	-0.9865	1.1941
140	-1.0144	1.0365	140	-1.0144	1.0365	140	-1.0144	1.0365
145	-0.9929	0.8577	145	-0.9929	0.8577	145	-0.9929	0.8577
150	-0.9031	0.6560	150	-0.9031	0.6560	150	-0.9031	0.6560
155	-0.7101	0.4329	155	-0.7101	0.4329	155	-0.7101	0.4329
160	-0.6268	0.3090	160	-0.6268	0.3090	160	-0.6268	0.3090
165	-0.7269	0.2436	165	-0.7269	0.2436	165	-0.7269	0.2436
170	-0.9512	0.1091	170	-0.9512	0.1091	170	-0.9512	0.1091
175	-0.6873	0.0497	175	-0.6873	0.0497	175	-0.6873	0.0497
180	-0.3905	0.0263	180	-0.3905	0.0263	180	-0.3905	0.0263

BIBLIOGRAPHY

Akselvoll, K. & Moin, P. (1993). Application of the dynamic localization model to large-eddy simulation of turbulent flow over a backward facing step. *ASME-PUBLICATIONS-FED*, 162, 1–1.

Amdahl, G. M. (1967). Validity of the Single Processor Approach to Achieving Large Scale Computing Capabilities. *Proceedings of the April 18-20, 1967, Spring Joint Computer Conference*, (AFIPS '67 (Spring)), 483–485. doi: 10.1145/1465482.1465560.

Anderson, J. (2010). *Fundamentals of Aerodynamics*. McGraw-Hill Education.

Bartlett, M. S. (1948). Smoothing Periodograms from Time-Series with Continuous Spectra. *Nature*, 161, 686–687. doi: 10.1038/161686a0.

Bautista, M. (2015). *Turbulence modelling of the atmospheric boundary layer over complex topography*. (Ph.D. thesis).

Bazilevs, Y., Hsu, M.-C., Akkerman, I., Wright, S., Takizawa, K., Henicke, B., Spielman, T. & Tezduyar, T. E. (2011a). 3D simulation of wind turbine rotors at full scale. Part I: Geometry modeling and aerodynamics. *International Journal for Numerical Methods in Fluids*, 65, 207–235.

Bazilevs, Y., Hsu, M.-C., Kiendl, J., Wüchner, R. & Bletzinger, K.-U. (2011b). 3D simulation of wind turbine rotors at full scale. Part II: Fluid–structure interaction modeling with composite blades. *International Journal for Numerical Methods in Fluids*, 65, 236–253.

Bechmann, A., Mann, J., Johansen, J., Sørensen, N. & Sørensen, J. (2007). *Large-eddy simulation of atmospheric flow over complex terrain*. (Ph.D. thesis). Consulted at Risø-PhD-28(EN).

Bechmann, A., Sørensen, N. N. & Zahle, F. (2011). CFD simulations of the MEXICO rotor. *Wind Energy*, 14(5), 677–689.

Bidadi, S. & Rani, S. L. (2015). Investigation of numerical viscosities and dissipation rates of second-order TVD-MUSCL schemes for implicit large-eddy simulation. *Journal of Computational Physics*, 281, 1003–1031. doi: 10.1016/j.jcp.2014.10.057.

Boussinesq, J. (1877). *Essai sur la théorie des eaux courantes*. Imprimerie Nationale.

BP. (2017). *BP Statistical Review of World Energy*.

Branlard, E. & Gaunaa, M. (2014). Development of new tip-loss corrections based on vortex theory and vortex methods. *Journal of Physics: Conference Series*, 555(1), 012012.

Breton, S.-P., Sibuet-Watters, C., Masson, C., Iradi, S. G. & Munduate, X. (2012). On the prediction of tip vortices in the near wake of the MEXICO rotor using the actuator surface method. *International Journal of Engineering Systems Modelling and Simulation*, 4(1/2), 11. doi: 10.1504/IJESMS.2012.044840.

Calaf, M., Meneveau, C. & Meyers, J. (2010). Large eddy simulation study of fully developed wind-turbine array boundary layers. *Physics of Fluids*, 22(1), 015110. doi: 10.1063/1.3291077.

Carrión, M., Steijl, R., Woodgate, M., Barakos, G., Munduate, X. & Gomez-Iradi, S. (2015). Computational fluid dynamics analysis of the wake behind the MEXICO rotor in axial flow conditions. *Wind Energy*, 18(6), 1023–1045.

Chattot, J.-J. (2011). Wind turbine aerodynamics: analysis and design. *International Journal of Aerodynamics*, 1(3/4), 404. doi: 10.1504/IJAD.2011.038853.

Churchfield, M., Laursen, J., Loeven, A., Lee, S. & Moriarty, P. J. (2013). A Comparison Between Wind Turbine Aerodynamics Model Output When Using a Generic Versus the Actual Turbine Characterization as Input. (51st AIAA Aerospace Sciences Meeting including the New Horizons Forum and Aerospace Exposition), 1–18.

Churchfield, M. J., Lee, S., Michalakes, J. & Moriarty, P. J. (2012). A numerical study of the effects of atmospheric and wake turbulence on wind turbine dynamics. *Journal of turbulence*, (13), N14.

Comte-Bellot, G. (1969). *Turbulent flow between two parallel walls*. Aeronautical Research Council.

Crespo, A., Hernández, J. & Frandsen, S. T. (1999). Survey of modelling methods for wind turbine wakes and wind farms. *Wind Energy*, 2(1), 1–24. doi: 10.1002/(SICI)1099-1824(199901/03)2:1<1::AID-WE16>3.0.CO;2-7.

Davidson, L. (2009). Large Eddy Simulations: How to evaluate resolution. *International Journal of Heat and Fluid Flow*, 30(5), 1016–1025. doi: 10.1016/j.ijheatfluidflow.2009.06.006.

Davidson, P. (2015). *Turbulence: An Introduction for Scientists and Engineers*.

Dobrev, I., Massouh, F. & Rapin, M. (2007). Actuator surface hybrid model. 75(1), 1–7.

Doran, P. (2017). *Étude des instabilités des tourbillons de sillage d'avion en effet de sol*. (Ph.D. thesis).

Drela, M. (1989). XFOIL: An Analysis and Design System for Low Reynolds Number Airfoils. In Mueller, T. J. (Ed.), *Low Reynolds Number Aerodynamics: Proceedings of the Conference Notre Dame, Indiana, USA, 5–7 June 1989* (pp. 1–12). Berlin, Heidelberg: Springer Berlin Heidelberg. doi: 10.1007/978-3-642-84010-4_1.

Du, Z. & Selig, M. (1998). A 3-D stall-delay model for horizontal axis wind turbine performance prediction. (ASME Wind Energy Symposium), 9.

España, G., Aubrun, S., Loyer, S. & Devinant, P. (2011). Spatial study of the wake meandering using modelled wind turbines in a wind tunnel. *Wind Energy*, 14(7), 923–937.

Ferziger, J. & Peric, M. (2012). *Computational Methods for Fluid Dynamics*. Berlin Heidelberg: Springer.

Fureby, C., Tabor, G., Weller, H. G. & Gosman, A. D. (1997). A comparative study of subgrid scale models in homogeneous isotropic turbulence. *Physics of Fluids*, 9(5), 1416–1429. doi: 10.1063/1.869254.

Germano, M., Piomelli, U., Moin, P. & Cabot, W. (1991). A dynamic subgrid-scale eddy viscosity model. *Physics of Fluids A: Fluid Dynamics*, 3(7), 1760-1765. doi: 10.1063/1.857955.

Germano, M. (1986). A proposal for a redefinition of the turbulent stresses in the filtered Navier–Stokes equations. *Physics of Fluids*, 29(7), 2323. doi: 10.1063/1.865568.

Germano, M. (1992). Turbulence: the filtering approach. *Journal of Fluid Mechanics*, 238, 325–336.

Gilling, L. (2009). *TuGen*.

Glauert, H. (1935). Airplane Propellers. In Durand, W. F. (Ed.), *Aerodynamic Theory, Vol. IV, Division L* (pp. 169-360). New York: Springer.

Hand, M., Simms, D., Fingersh, L., Jager, D., Cotrell, J., Schreck, S. & Larwood, S. (2001). *Unsteady Aerodynamics Experiment Phase VI: Wind Tunnel Test Configurations and Available Data Campaigns*.

Hansen, M. O. L., Sørensen, J. N., Voutsinas, S., Sørensen, N. N. & Madsen, H. A. (2006). State of the art in wind turbine aerodynamics and aeroelasticity. *Progress in Aerospace Sciences*, 42(4), 285–330. doi: 10.1016/j.paerosci.2006.10.002.

Hau, E. (2008). *Windkraftanlagen: Grundlagen, Technik, Einsatz, Wirtschaftlichkeit*. Berlin Heidelberg: Springer.

Holierhoek, J. G., de Vaal, J. B., van Zuijlen, A. H. & Bijl, H. (2013). Comparing different dynamic stall models. *Wind Energy*, 16(1), 139–158.

Hough, G. R. & Ordway, D. E. (1964). *The generalized actuator disk*. Developments in Theoretical and Applied Mechanics.

(2015). Wind turbines [Norm]. ISO, Geneva, Switzerland.

Issa, R. I. (1986). Solution of the implicitly discretised fluid flow equations by operator-splitting. *Journal of Computational Physics*, 62(1), 40–65. doi: 10.1016/0021-9991(86)90099-9.

Ivanell, S., Sørensen, J. N., Mikkelsen, R. F. & Henningson, D. (2009). Analysis of numerically generated wake structures. *Wind Energy*, 12(1), 63–80. doi: 10.1002/we.285.

Ivanell, S., Mikkelsen, R. F., Sørensen, J. N. & Henningson, D. (2010). Stability analysis of the tip vortices of a wind turbine. *Wind Energy*, 13(8), 705–715.

Jasak, H. (1996). *Error analysis and estimation for finite volume method with applications to fluid flow*. (Ph.D. thesis, Imperial College).

Jha, P. K., Churchfield, M. J., Moriarty, P. J. & Schmitz, S. (2013). Guidelines for Actuator Line Modeling of Wind Turbines on Large-Eddy Simulation-type Grids. *Journal of Solar Energy Engineering*, 136(August), 1–11. doi: 10.1115/1.4026252.

Johansson, P. B. V. & George, W. K. (2006). The far downstream evolution of the high-Reynolds-number axisymmetric wake behind a disk. Part 1. Single-point statistics. *Journal of Fluid Mechanics*, 555, 363–385.

Jones, W. P. & Launder, B. E. (1972). The prediction of laminarization with a two-equation model of turbulence. *International Journal of Heat and Mass Transfer*, 15(2), 301–314. doi: 10.1016/0017-9310(72)90076-2.

Kalvig, S., Manger, E. & Hjertager, B. (2014). Comparing different CFD wind turbine modelling approaches with wind tunnel measurements. 555(1), 1–13.

Kelley, N. D. (1992). *Full vector (3-D) inflow simulation in natural and wind farm environments using an expanded version of the SNLWIND (Veers) turbulence code*.

Krogstad, P.-Å. & Lund, J. A. (2012). An experimental and numerical study of the performance of a model turbine. *Wind Energy*, 15(3), 443–457.

Larsen, G. C., Madsen, H. A., Thomsen, K. & Larsen, T. J. (2008). Wake meandering: A pragmatic approach. *Wind Energy*, 11(4), 377–395. doi: 10.1002/we.267.

Leishman, J. G. & Beddoes, T. S. (1989). A SemiEmpirical Model for Dynamic Stall. *Journal of the American Helicopter Society*, 34(3), 3-17. doi: doi:10.4050/JAHS.34.3.

Leishman, J. G. (2002). Challenges in Modeling the Unsteady Aerodynamics of Wind Turbines. *Wind Energy*, 5(2-3), 85–132. doi: 10.1115/wind2002-37.

Leonard, B. P. (1979). A stable and accurate convective modeling procedure based on quadratic upstream interpolation. *Computer Methods in Applied Mechanics and Engineering*, 19, 59–98.

Lesieur, M., Métais, O. & Comte, P. (2005). *Large-Eddy Simulations of Turbulence*. Cambridge University Press.

Mann, J. (1998). Wind field simulation. *Probabilistic Engineering Mechanics*, 13(4), 269–282. doi: 10.1016/S0266-8920(97)00036-2.

Manwell, J., McGowan, J. & Rogers, A. (2010). *Wind Energy Explained: Theory, Design and Application*. Wiley.

Martinen, S., Carlén, I., Nilsson, K., Breton, S. & Ivanell, S. (2014). Analysis of the effect of curtailment on power and fatigue loads of two aligned wind turbines using an actuator disc approach. 524, 012182.

Martínez-Tossas, L. A., Churchfield, M. J. & Meneveau, C. (2015). Optimal smoothing length scale for actuator line models of wind turbine blades. *Wind Energy*, 00, 1–14.

Martínez-Tossas, L. A., Churchfield, M. J. & Meneveau, C. (2016). A Highly Resolved Large-Eddy Simulation of a Wind Turbine using an Actuator Line Model with Optimal Body Force Projection. *Journal of Physics: Conference Series*, 753(8), 082014.

Mason, P. J. (1994). Large-eddy simulation: A critical review of the technique. *Quarterly Journal of the Royal Meteorological Society*, 120(515), 1–26. doi: 10.1002/qj.49712051503.

Meneveau, C., Lund, T. S. & Cabot, W. H. (1996). A Lagrangian dynamic subgrid-scale model of turbulence. *Journal of Fluid Mechanics*, 319(-1), 353. doi: 10.1017/S0022112096007379.

Menter, F. R. (1994). Two-Equation Eddy-Viscosity Turbulence Modls for Engineering Applications. *AIAA Journal*, 32(8), 1598–1605.

Meyers, J. & Meneveau, C. (2012). Optimal turbine spacing in fully developed wind farm boundary layers. *Wind Energy*, 15(2), 305–317.

Mikkelsen, R. (2004). *Actuator Disc Methods Applied to Wind Turbines*. (Ph.D. thesis, DTU, Copenhagen, DK).

Muller, Y.-A. (2015). *Étude du méandrement du sillage éolien lointain dans différentes conditions de rugosité*. (Ph.D. thesis).

Nathan, J., Bautista, M., Masson, C. & Dufresne, L. (2014). Study of the near wake of a wind turbine in ABL flow using the actuator line method. (TORQUE2014: 5. science of making torque from wind conference), 1–10.

Nathan, J., Forsting, A. R. M., Troldborg, N. & Masson, C. (2017). Comparison of OpenFOAM and EllipSys3D actuator line methods with (NEW) MEXICO results. *Journal of Physics: Conference Series*, 854(1), 012033.

Nilsson, K., Shen, W. Z., Sørensen, J. N., Breton, S.-P. & Ivanell, S. (2015). Validation of the actuator line method using near wake measurements of the MEXICO rotor. *Wind Energy*, 18(9), 499–514.

Olivares Espinosa, H. (2017). *Turbulence Modelling in Wind Turbine Wakes*. (Ph.D. thesis).

Pereira, R., Schepers, G. & Pavel, M. D. (2013). Validation of the Beddoes–Leishman dynamic stall model for horizontal axis wind turbines using MEXICO data. *Wind Energy*, 16(2), 207–219.

Piomelli, U. (1993). High Reynolds number calculations using the dynamic subgrid-scale stress model. *Physics of Fluids A: Fluid Dynamics*, 5(6), 1484-1490. doi: 10.1063/1.858586.

Pope, S. (2000). *Turbulent Flows*. Cambridge University Press.

Pope, S. B. (2004). Ten questions concerning the large-eddy simulation of turbulent flows. *New Journal of Physics*, 6, 1–24. doi: 10.1088/1367-2630/6/1/035.

Porté-Agel, F., Meneveau, C. & Parlange, M. B. (2000). A scale-dependent dynamic model for large-eddy simulation: application to a neutral atmospheric boundary layer. *Journal of Fluid Mechanics*, 415(-1), 261–284. doi: 10.1017/S0022112000008776.

Rethore, P.-E. M. & Sørensen, N. N. (2008). Actuator disc model using a modified Rhie-Chow/SIMPLE pressure correction algorithm. Comparison with analytical solutions. (Energy Association (EWEA)), 1–11.

Rhie, C. & Chow, W. (1983). Numerical study of the turbulent flow past and airfoil with trailing edge separation. *AIAA Journal*, 21(11), 1525–1532. doi: 10.2514/3.8284.

Sagaut, P. (2006). *Large Eddy Simulation for Incompressible Flows: An Introduction*. Springer.

Sanderse, B., van der Pijl, S. & Koren, B. (2011). Review of computational fluid dynamics for wind turbine wake aerodynamics. *Wind Energy*, 14(7), 799–819.

Schepers, J. & Boorsma, K. (2014). *New MEXICO experiment: Preliminary overview with initial validation*.

Schepers, J., Boorsma, K., Cho, T., Gomez-Iradi, S., Schaffarczyk, P., Jeromin, A., Shen, W., Lutz, T., Meister, K., Stoevesandt, B., Schreck, S., Micallef, D., Pereira, R., Sant, T., Madsen, H. & Sørensen, N. (2012). *Final report of IEA Task 29, Mexnext (Phase 1): Analysis of Mexico wind tunnel measurements*.

Schmitz, S. & Chattot, J.-J. (2006). A coupled Navier-Stokes/Vortex-Panel solver for the numerical analysis of wind turbines. *Computers & Fluids*, 35, 742–745. doi: 10.1016/j.compfluid.2006.01.006.

Shamsoddin, S. & Porté-Agel, F. (2016). A Large-Eddy Simulation Study of Vertical Axis Wind Turbine Wakes in the Atmospheric Boundary Layer. *Energies*, 9, 366.

Shannon, C. E. (1949). Communication in the presence of noise. *Proceedings of the IRE*, 37(1), 10–21.

Shen, W. Z., Mikkelsen, R., Sørensen, J. N. & Bak, C. (2005). Tip loss corrections for wind turbine computations. *Wind Energy*, 8(4), 457–475. doi: 10.1002/we.153.

Shen, W. Z., Hansen, M. O. L. & Sørensen, J. N. (2009a). Determination of the angle of attack on rotor blades. *Wind Energy*, 12(1), 91–98. doi: 10.1002/we.277.

Shen, W. Z., Zhang, J. H. & Sørensen, J. N. (2009b). The Actuator Surface Model: A New Navier–Stokes Based Model for Rotor Computations. *Journal of Solar Energy Engineering*, 131(1), 011002. doi: 10.1115/1.3027502.

Shen, W. Z., Zhu, W. J. & Sørensen, J. N. (2012). Actuator line/Navier–Stokes computations for the MEXICO rotor: comparison with detailed measurements. *Wind Energy*, 15(5), 811–825.

Shives, M. & Crawford, C. (2013). Mesh and load distribution requirements for actuator line CFD simulations. *Wind Energy*, 16(8), 1183–1196.

Sibuet Watters, C. & Masson, C. (2010). Modeling of lifting-device aerodynamics using the actuator surface concept. *International Journal for Numerical Methods in Fluids*, 62(11), 1264–1298.

Smagorinsky, J. (1963). General circulation experiments with the primitive equations: 1. The basic experiment. *Monthly Weather Review*, 91(3), 99–164. doi: 10.1175/1520-0493(1963)091<0099:GCEWTP>2.3.CO;2.

Snel, H. (1998). Review of the present status of rotor aerodynamics. *Wind Energy*, 1(S1), 46–69. doi: 10.1002/(SICI)1099-1824(199804)1:1+<46::AID-WE3>3.3.CO;2-0.

Sørensen, J. N. & Shen, W. Z. (2002). Numerical Modeling of Wind Turbine Wakes. *Journal of Fluids Engineering*, 124(2), 393. doi: 10.1115/1.1471361.

Sørensen, N. N. & Schreck, S. J. (2012). Computation of the National Renewable Energy Laboratory Phase-VI rotor in pitch motion during standstill. *Wind Energy*, 15(3), 425–442.

Sørensen, N. N., Bechmann, A., Réthoré, P.-E. & Zahle, F. (2014). Near wake Reynolds-averaged Navier–Stokes predictions of the wake behind the MEXICO rotor in axial and yawed flow conditions. *Wind Energy*, 17(1), 75–86.

Sørensen, N. N., Zahle, F., Boorsma, K. & Schepers, G. (2016). CFD computations of the second round of MEXICO rotor measurements. *Journal of Physics: Conference Series*, 753, 022054. doi: 10.1088/1742-6596/753/2/022054.

Spalart, P. & Allmaras, S. (1994). A One-Equation Turbulence Model for Aerodynamic Flows. (La Recherche Aérospatiale), 5–21.

Spalart, P. R. & Garbaruk,A. Howerton, B. M. (2017). CFD Analysis of an Installation Used to Measure the Skin-Friction Penalty of Acoustic Treatments. (AIAA Aviation 2017 Conference; 5-9 Jun. 2017), 1.

Speziale, C. G. (1985). Galilean invariance of subgrid-scale stress models in the large-eddy simulation of turbulence. *Journal of Fluid Mechanics*, 156, 55–62.

Stroustrup, B. (2013). *The C++ Programming Language* (ed. 4th). Addison-Wesley Professional.

Stull, R. (2012). *An Introduction to Boundary Layer Meteorology*. Springer Netherlands.

Sørensen, N. (1995). *General purpose flow solver applied to flow over hills*. (Ph.D. thesis, DTU). Consulted at Published 2003.

Tennekes, H. & Lumley, J. (1972). *A First Course in Turbulence*. Pe Men Book Company.

Troldborg, N., Zahle, F., Réthoré, P.-E. & Sørensen, N. N. (2015). Comparison of wind turbine wake properties in non-sheared inflow predicted by different CFD rotor models. *Wind Energy*, (18(7)), pp. 1239–1250.

Troldborg, N. (2009). *Actuator Line Modeling of Wind Turbine Wakes*. (Ph.D. thesis, DTU, Copenhagen, DK).

Vanella, M., Piomelli, U. & Balaras, E. (2008). Effect of grid discontinuities on large-eddy simulation statistics and flow fields. *Journal of Turbulence*, 9(January), 37–41. doi: 10.1080/14685240802446737.

Veers, P. S. (1988). *Three-dimensional wind simulation*.

Vermeer, L. J., Sørensen, J. N. & Crespo, A. (2003). Wind turbine wake aerodynamics. *Progress in Aerospace Sciences*, 39(6-7), 467–510. doi: 10.1016/S0376-0421(03)00078-2.

Versteeg, H. & Malalasekera, W. (2007). *An Introduction to Computational Fluid Dynamics: The Finite Volume Method*. Pearson Education Limited.

Vijayakumar, G., Lavely, A., Jayaraman, B., Craven, B. & Brasseur, J. (2013, 11). Forcing of Wind Turbine Blade Boundary Layer Dynamics by Atmospheric Turbulence with Hybrid URANS-LES. *APS Division of Fluid Dynamics Meeting Abstracts*.

Viterna, L. A. & Janetzke, D. C. (1982). *Theoretical and experimental power from large horizontal-axis wind turbines*.

Warming, R. & Beam, R. M. (1976). Upwind second-order difference schemes and applications in aerodynamic flows. *AIAA J*, 14(9), 1241–1249.

Weller, H. G., Tabor, G., Jasak, H. & Fureby, C. (1998). A tensorial approach to computational continuum mechanics using object-oriented techniques. *Computers in Physics*, 12(6), 620–631. doi: 10.1063/1.168744.

Wilcox, D. (2006). *Turbulence Modeling for CFD*. DCW Industries.